Proximity Effects in Ferromagnet/Superconductor Layered Heterostructures with Inhomogeneous Magnetization

A THESIS
SUBMITTED TO THE FACULTY OF THE GRADUATE SCHOOL
OF THE UNIVERSITY OF MINNESOTA
BY

Chien-Te Wu

IN PARTIAL FULFILLMENT OF THE REQUIREMENTS
FOR THE DEGREE OF
Doctor of Philosophy

Oriol T. Valls

July, 2014

Acknowledgements

First of all, I would like to express my deepest gratitude to my advisor, Professor Oriol Valls, for his guidance, support, and encouragement during these past five years. I have been fortunate to have him as my advisor. He has taught me numerous lessons on physics research and offered me his invaluable insights to guide me through all the challenges that I have faced. His kind and patient instruction has made this thesis possible. He has not only guided me through my PhD education, but also provided his wisdom to help me advance to the next step in my career. I would also like to thank Dr. Klaus Halterman for his long-term collaboration and all his enthusiastic and useful help during these years. I would like to thank my committee members, Professor Allen Goldman, Charles Campbell, and Jiangping Wang for their time and valuable advice on my thesis. I would also like to thank Professor Cheng-Cher Huang, Charles Campbell, and Aaron Wynveen who had constantly offered me their advice and helped me throughout my academic career. I would like to thank my friends Yu-Chen Liu, Chia-Luen Lee, Cheng-Chia Lee, Chih-Jung Hung, Chun-I Chuang, Abdul Naseer Malmi Kakkada, Gaurav Shukla, Xiaowei Zhang, Cheng-Hsien Li, Lu-Chen Weng, Chia Wei, Yu-Min Chuo, Kaily Liu, Kevin Kao, and Ke-Jung Chen. I thank my girlfriend Haithien Phu. Without her, this thesis whould not have been possible. Finally, I thank my parent for their love, support, and constant encouragement over the years.

This thesis is supported by IARPA grant No. N66001-12-1-2023 and by the Dissertation Fellowship of the University of Minnesota.

Dedication

I would like to dedicate my thesis to my beloved parents.

Abstract

In this thesis, we present a theoretical investigation of the proximity effects in ferromagnet/superconductor heterostructures with inhomogeneous magnetization, including ferromagnet/ferromagnet/superconductor (F_1F_2S) trilayers and conical-ferromagnet/ superconductor bilayers. We numerically obtain the self-consistent solutions of the Bogoliubov-de Gennes (BdG) equations and use these solutions to compute the relevant physical quantities. In F_1F_2S trilayers, we find that the critical temperature, T_c, can be a non-monotonic function of the angle α between magnetizations in F layers. The minimum $T_c(\alpha)$ often occurs when magnetizations are mutually perpendicular ($\alpha = \frac{\pi}{2}$). In addition, we demonstrate that the T_c minimum corresponds to the maximum of the penetration of the long-range triplet amplitudes. We compare our theoretical results with experiment and find that they are in excellent agreement. We also study other aspects of proximity effects such as the local density of states, local magnetizations, and thermodynamic functions. In conical-ferromagnet/superconductor bilayers, we obtain the relation between T_c and the thickness d_F of the magnetic layer, and find that the $T_c(d_F)$ curves include multiple oscillations. Moreover, for a range of d_F, the superconductivity is reentrant with temperature T: as one lowers T the system turns superconducting, and when T is further lowered it returns to normal. We demonstrate that the behavior of both $m = 0$ and $m = \pm 1$ triplet amplitudes are related to the intrinsic periodicity of conical ferromagnet. Our theoretical fits of $T_c(d_F)$ are in good agreement with experimental data. The transport properties, including the tunneling conductance and the spin polarized transport, in F_1F_2S trilayers are investigated. To fully take into account proximity effects, we adopt a transfer matrix method incorporated with the Blonder-Tinkham-Klapwijk formalism and self-consistent solutions to the BdG equations. We show that our method ensures that conservation laws are properly satisfied. Our results indicate that the behavior of tunneling conductance depends on the misorientation angle between magnetizations, and also exhibits resonance effects. We also investigate the bias dependence of non-equilibrium spin transfer torque and its connection to both spin currents and local magnetizations.

Contents

List of Figures

Chapter 1

Introduction

1.1 Basics of superconductivity

Superconductivity was first discovered by the group of Heike Kamerlingh Onnes in 1911 [1, 2]. When studying the electrical resistance of mercury at low temperatures, they found that the resistance abruptly disappeared at about 4.2 K. As a consequence, a current can circulate in a closed superconducting ring for years without measurable decay. In understanding superconductivity, another important property of materials in the superconducting state was discovered by Meissner and Ochsenfeld in 1933 [3]. This property, known as the Meissner effect, describes the complete expulsion of the magnetic flux from a superconductor during its transition to the superconducting state [1, 2]. It is important to recognize that the Meissner effect cannot be explained by perfect conductance, since, as opposed to the Meissner effect for a superconductor, a normal conductor would keep the magnetic field in which it is embedded.

However, if a sufficiently large magnetic field is applied, superconductivity is destroyed. The field at which a superconductor recovers its normal resistance is known as the critical magnetic field strength. An applied magnetic field B increases the free energy of the superconducting phase F_S by $B^2/2\mu_0$. On the other hand, there is no comparable free energy increase for the normal phase. Thus, $F_N(T) - F_S(T) = {B_c}^2(T)/2\mu_0$ and the entropy difference is $S_S - S_N = \frac{B_c}{\mu_0}\frac{dB_c}{dT}$. Because B_c decreases with increasing temperature, the entropy difference is negative: the superconducting phase is therefore more ordered than the normal phase. Since $S_S = S_N$ at $T = T_c$, the transition at

$T = T_c$ is of the second-order phase transition. However, the transition in the presence of a field is of the first order.

The widely-accepted microscopic theory led by the Cooper pair idea to explain superconductivity was first advanced by Bardeen, Cooper, and Schrieffer (BCS) in 1957, almost half a century after the discovery of superconductivity [4]. Just one year before the formulation of the BCS theory, Cooper demonstrated that the normal Fermi sea becomes unstable in the presence of any small attractive interaction among electrons [5]. This attraction can bind interacting pairs of electrons, generally known as Cooper pairs, near the Fermi sea into bound states. The BCS ground-state wavefunction for superconductors can be described by $|\Psi_S\rangle = \prod_{\mathbf{k}}(u_{\mathbf{k}} + v_{\mathbf{k}} c^{\dagger}_{\mathbf{k}\uparrow} c^{\dagger}_{-\mathbf{k}\downarrow})|0\rangle$ under the constraint $|u_{\mathbf{k}}|^2 + |v_{\mathbf{k}}|^2 = 1$, where $|0\rangle$ is the vacuum state. $|v_{\mathbf{k}}|^2$ represents the probability amplitude that the pair $(\mathbf{k}\uparrow, -\mathbf{k}\downarrow)$, which consists of a spin-up electron with momentum $\mathbf{k}$ and spin-down electron with momentum $-\mathbf{k}$, is occupied and $|u_{\mathbf{k}}|^2$ represents the probability amplitude that it is unoccupied. We can see that electrons are involved only as pairs in the BCS ground state. In fact, this BCS ground-state wavefunction is a superposition of terms containing different numbers of Cooper pairs. One can find $u_{\mathbf{k}}$ and $v_{\mathbf{k}}$ by minimizing the ground-state energy under the constraint $\langle \Psi_S | N_{op} | \Psi_S \rangle = N$, where N_{op} is the particle number operator and N is the number of electrons in the actual metal. By taking advantage of the method of Lagrange multipliers, the effective BCS Hamiltonian, $H_{BCS} \equiv H - \mu N_{op}$, is given by

$$H_{BCS} = \sum_{\mathbf{k}} \epsilon_{\mathbf{k}} \left(c^{\dagger}_{\mathbf{k}\uparrow} c_{\mathbf{k}\uparrow} + c^{\dagger}_{-\mathbf{k}\downarrow} c_{-\mathbf{k}\downarrow} \right) + \sum_{\mathbf{k}\mathbf{k}'} U_{\mathbf{k}\mathbf{k}'} c^{\dagger}_{\mathbf{k}\uparrow} c^{\dagger}_{-\mathbf{k}\downarrow} c_{-\mathbf{k}'\downarrow} c_{\mathbf{k}'\uparrow}, \tag{1.1}$$

where μ (or E_F) is the Fermi energy, $\epsilon_{\mathbf{k}} \equiv \hbar^2 \mathbf{k}^2 / 2m - \mu$, and $U_{\mathbf{k}\mathbf{k}'}$ is the strength of an attractive interaction. Using the anti-commutation relations of the fermion operators, one can obtain the following expression for the superconducting ground-state energy, $F_S(T = 0)$,

$$W_S = 2 \sum_{\mathbf{k}} \epsilon_{\mathbf{k}} v^2_{\mathbf{k}} + \sum_{\mathbf{k}\mathbf{k}'} U_{\mathbf{k}\mathbf{k}'} u_{\mathbf{k}} v_{\mathbf{k}} u_{\mathbf{k}'} v_{\mathbf{k}'}. \tag{1.2}$$

The minimization conditions together with the normalization condition, $u^2_{\mathbf{k}} + v^2_{\mathbf{k}} = 1$, lead to $u^2_{\mathbf{k}} = \frac{1}{2}\left[1 + \frac{\epsilon_{\mathbf{k}}}{\sqrt{\epsilon^2_{\mathbf{k}} + \Delta^2_{\mathbf{k}}}}\right]$ and $v^2_{\mathbf{k}} = \frac{1}{2}\left[1 - \frac{\epsilon_{\mathbf{k}}}{\sqrt{\epsilon^2_{\mathbf{k}} + \Delta^2_{\mathbf{k}}}}\right]$, where the so-called gap parameter is defined as $\Delta_{\mathbf{k}} = -\sum_{\mathbf{k}'} U_{\mathbf{k}\mathbf{k}'} u_{\mathbf{k}'} v_{\mathbf{k}'}$, and must be determined self-consistently.

For simplicity, Cooper introduced the average potential approximation that all $U_{\mathbf{k}\mathbf{k}'} = -V$ for states in the energy shell of width $\hbar\omega_D$, the Debye cutoff energy, around E_F, and $U_{\mathbf{k}\mathbf{k}'} = 0$ for states beyond $\hbar\omega_D$. By making this approximation, it follows that the gap parameter is independent of $\mathbf{k}$ and

$$\Delta_{\mathbf{k}} \equiv \Delta_0 = \sinh\left[1/VN(0)\right], \tag{1.3}$$

where $N(0)$ denotes the density of states at E_F for one spin direction.

Until now, we have considered the ground state of a superconductor at zero temperature. We can now obtain the excitation spectrum based on the canonical transformations proposed by Bogoliubov and Valatin independently [6, 7],

$$c_{\mathbf{k}\uparrow} = u_{\mathbf{k}}\gamma_{\mathbf{k}\uparrow} + v_{\mathbf{k}}\gamma^{\dagger}_{-\mathbf{k}\downarrow}, \tag{1.4a}$$

$$c_{-\mathbf{k}\downarrow} = u_{\mathbf{k}}\gamma_{-\mathbf{k}\downarrow} - v_{\mathbf{k}}\gamma^{\dagger}_{\mathbf{k}\uparrow}. \tag{1.4b}$$

With a routine procedure of the mean field theory and the help of the Bogoliubov transformations, the model Hamiltonian can now be recast into a diagonalized form,

$$H_{BCS} = \sum_{\mathbf{k}} \sqrt{\epsilon^2_{\mathbf{k}} + \Delta^2_{\mathbf{k}}} \left[\gamma^{\dagger}_{\mathbf{k}\uparrow}\gamma_{\mathbf{k}\uparrow} + \gamma^{\dagger}_{-\mathbf{k}\downarrow}\gamma_{-\mathbf{k}\downarrow}\right] + W_S. \tag{1.5}$$

The gap equation can also be generalized to non-zero temperatures,

$$\Delta_{\mathbf{k}} = -\sum_{\mathbf{k}'} U_{\mathbf{k}\mathbf{k}'} \frac{\Delta_{\mathbf{k}'}}{2E_{\mathbf{k}'}} \tanh\frac{\beta E_{\mathbf{k}'}}{2}, \tag{1.6}$$

where $E_{\mathbf{k}} = \sqrt{\epsilon^2_{\mathbf{k}} + \Delta^2_{\mathbf{k}}}$ and $\beta = \frac{1}{k_B T}$. Under the average potential approximation, $E_{\mathbf{k}} = \sqrt{\epsilon^2_{\mathbf{k}} + \Delta^2_0}$. It follows that the quasiparticle spectrum of the superconductor exhibits an energy gap given by Δ_0. In the superconductor, there are no electron-like states with energy in the interval $[E_F, E_F + \Delta_0]$, and no hole-like states in the interval $[E_F, E_F - \Delta_0]$. The self-consistency condition becomes

$$\frac{1}{V} = \frac{1}{2}\sum_{\mathbf{k}} \frac{\tanh\left(\beta E_{\mathbf{k}}/2\right)}{E_{\mathbf{k}}} \tag{1.7}$$

The critical temperature T_c is the temperature at which the gap parameter vanishes. By changing the sum to an integral, one can obtain $k_B T_c = 1.13\hbar\omega_D \exp^{-1/VN(0)}$ and $\Delta_0 = 1.764\ k_B T_c$. This is consistent with experimental values of $2\Delta_0$, which fall in the

range 3.0 to 4.5 $k_B T_c$. The BCS theory also predicts that a condensation energy at $T = 0$ is $W_S - W_N = -\frac{1}{2}N(0)\Delta_0^2$, where $W_N \equiv F_N(T = 0)$ is the total energy of the system in its normal state. Bardeen, Cooper, and Schrieffer received the 1972 Nobel prize for their extremely successful theory of superconductivity.

1.2 Superconducting proximity effects in ferromagnet/superconductor systems

What happens when non-superconducting materials are put in contact with superconductors? In 1932, Holm and Meissner conducted a tunneling experiment [8] on two superconductors connected by a small contact and found that a resistanceless current can pass through such junctions. Without knowing about Holm and Meissner's experiment, this phenomenon was also theoretically predicted in 1962 by Josephson, and is now known as the Josephson effect [9]. It is well understood that the existence of supercurrent tunneling from one superconductor to another is a result of superconducting proximity effects.

The superconducting proximity effects depict how the Cooper pairs diffuse into a non-superconducting normal metal, or equivalently, how the superconductivity is induced in the non-superconducting materials when placed in contact with superconductors [10]. To understand the superconducting proximity effects in these layered heterostructures, it is best to study the Cooper pair amplitudes, $F(\mathbf{r}) \equiv \langle \psi_\uparrow(\mathbf{r})\psi_\downarrow(\mathbf{r})\rangle$, that are proportional to the probability of finding a Cooper pair in space. Note that in the above expression for the pair amplitudes, the position dependent field operators are adopted to take into account the inhomogeneous systems we consider here. In nonmagnetic normal metal/superconductor (N/S) bilayers with a sufficiently good contact at the interface, it is found that at finite temperatures the Cooper pair amplitudes in the N layers has the asymptotic form, $F \sim \exp(-|x|/\xi_N)$, where x denotes the distance from the N/S interface [10]. In the clean limit, the characteristic decay length, ξ_N, in the above asymptotic form is $\xi_N = \hbar v_F/2\pi k_B T$, where v_F is the Fermi velocity. However, when T approaches zero, the asymptotic form of F in the N regions becomes $1/|x|$ indicating that the proximity effects in N/S systems are very long ranged. Indeed, the "proximity length" of the leakage in the N layer is experimentally found to be very

long ($10^4 \mathring{A}$ or even larger) [11]. Due to the proximity effects, the superconductivity not only decays into the N layer, but is also depleted in the S layer near the interface as a result of the leakage. As a consequence of this leakage, the superconducting transition temperatures, T_c, of the N/S bilayers is lower than that of pure bulk S materials. The physical origin behind the leakage of superconductivity in the N layer is related to the process of the Andreev reflection [12]. Consider an electron (hole) incident from the N side with energy within the superconducting gap: a hole (electron) with opposite spin of the incident electron (hole) can be retroreflected at the N/S interfaces. As a result, the incident electron together with another electron, corresponding to the reflected hole, form a Cooper pair in the superconductor. By means of the Andreev reflection, the normal metal in the N/S layered structures can acquire superconductivity.

Recently, superconducting proximity effects in ferromagnet/superconductor (F/S) systems [13] have also attracted the interest of researchers due to their potential technological applications in spintronics [14]. The exchange interaction tends to align spins of electrons in the same direction in ferromagnets, whereas for s-wave superconductors, Cooper pairs are composed of electrons with opposite spins. Therefore, ferromagnetism and s-wave superconductivity seem two mutually exclusive phenomena and is therefore difficult to find them coexisting in **bulk** materials [13]. However, due to the great advances of fabrication technologies, such coexistence can now be attained near the interfaces of F/S heterostructures by the superconducting proximity effects, as we discussed above in N/S heterostructures, and by the reverse proximity effect, the penetration of the spin polarization into the S layer. Thus, F/S junctions provide researchers opportunities to study the interplay between magnetism and superconductivity.

The most prominent feature of F/S systems is that the Cooper pair amplitudes not only decay, as in N/S structures, but also oscillate inside the ferromagnets [15, 16]. As a simplified illustration, the qualitative behavior of the pair amplitudes is plotted as a function of position near the F/S interface in Fig. 1.1. One can clearly see that the superconductivity is weakened on the superconducting side near the interface. The pair amplitudes deep inside the superconductor gradually saturate to their bulk value (far right outside the range plotted in Fig. 1.1). In the ferromagnet region, the pair amplitudes decay and oscillate.

A qualitative explanation of this oscillatory behavior is given in Ref. [15]. When

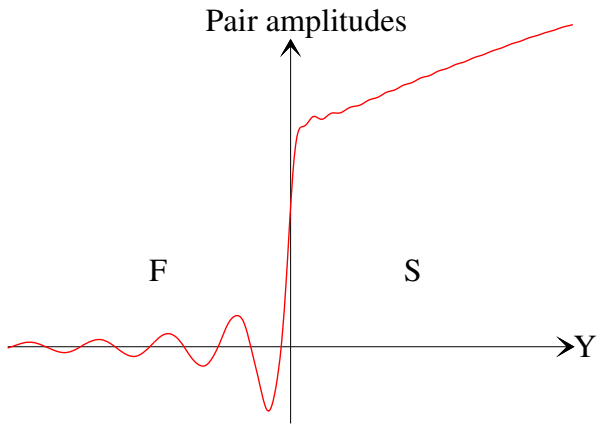

Figure 1.1: Schematic behavior of the Cooper pair amplitudes, near the F/S interface, are plotted as a function of position, Y. The vertical axis represents the F/S interface.

the Cooper pair enters into the F side, the electron with a spin parallel to the exchange field **h**, the effective internal field associated with the exchange interaction, lowers its energy by h, while the other electron with an opposite spin increases its energy by the same amount (see below). To separately conserve their total energy, the Cooper pair acquires a nonzero center-of-mass momentum in the ferromagnetic layer. Considering all possible angles incident to the interface and the antisymmetric requirement on the spin part, the overall pair amplitudes are found to be sinusoidally modulated in space. Therefore, the physical picture of the proximity effect in F/S heterostructures is similar to the physics of the superconducting order parameter modulation in the Fulde-Ferrell-Larkin-Ovchinnikov state [17, 18].

Both the decay length and the oscillation period are determined by the strength of the exchange field. As a matter of fact, both of them are shorter when the exchange field of ferromagnets in F/S systems is stronger. The characteristic length ξ_F that describes the oscillating period of the Cooper pair amplitudes is investigated in Ref. [16] and is found in the form, $\xi_F \approx (k_{F\uparrow} - k_{F\downarrow})^{-1}$, where $k_{F\uparrow}$ and $k_{F\downarrow}$ are Fermi wavevectors for the spin-up band and spin-down band in ferromagnets respectively [15]. If there is no Fermi wavevector mismatch between the ferromagnets and the superconductors, we then have $\frac{k_{F\uparrow}^2}{2m} = \frac{k_{FS}^2}{2m} + h$ and $\frac{k_{F\downarrow}^2}{2m} = \frac{k_{FS}^2}{2m} - h$, where k_{FS} is the Fermi wavevector for

superconductors. The characteristic length becomes

$$\xi_F \approx k_F^{-1} \left[\sqrt{1+I} - \sqrt{1-I} \right]^{-1}, \tag{1.8}$$

where I, normalized to the Fermi energy E_{FS}, is the dimensionless strength of the exchange field. In this notation, $I \equiv \frac{h}{E_{FS}} = 1$ represents a fully spin-polarized ferromagnet, i.e., a half metal. In addition to the oscillating period, ξ_F also characterizes the decay length of the pair amplitudes as indicated in Ref. [16]. Therefore, compared to the N/S layered structures, the proximity length in a strong ferromagnet of F/S systems can be much shorter, typically in the order of $10\mathring{A}$ or, for a half metal, less.

As a consequence of the damped oscillatory nature of the Cooper pair amplitudes, the transition temperatures of F/S bilayers have unusual non-monotonic dependencies on the F layer thickness [13, 19]. This unusual dependence occurs because the transmitted Cooper pair amplitudes can interfere with the reflected ones from the boundaries of the F/S systems due to their oscillatory nature. Therefore, the transition temperature, as a function of the F layer thickness, usually exhibits several oscillations before it saturates at large thicknesses of the F layer. The non-monotonic behavior of transition temperatures is both theoretically predicted [19, 20, 21] and experimentally observed [22, 23, 24]. In some cases, when the interference between the transmitted and reflected pair amplitudes is sufficiently strong, the transition temperature drops to zero in a certain range of F layer thicknesses but reappears when the thickness is increased. The reentrant phenomenon with the F layer thickness has been experimentally and theoretically confirmed [19, 20, 21, 22, 23, 24, 25, 26, 27, 28].

Another fascinating phenomenon exhibited by F/S heterostructures is the induction of long-range triplet pairing correlations in F/S systems with inhomogeneous magnetization, where S is in the ordinary s-wave pairing state [29, 30, 31, 32, 33, 34]. As discussed in previous paragraphs, the proximity length of the "singlet" pair amplitudes in the F region is usually short because the exchange field tends to align the spins of singlet Cooper pairs. However, unlike the singlet state where two electrons with opposite spins are paired, the pairing of $m = \pm 1$ triplet states that consist of electrons with same spin is compatible to the nature of the exchange field. Accordingly, equal-spin triplet pairing correlations may survive in the F region for a much longer distance, comparable to the proximity length of N/S systems, than singlet pair amplitudes.

It seems intuitively at first sight that the existence of these "s-wave" triplet pairing states violates the Pauli exclusion principle. However, by allowing a time delay in the correlation functions of the triplet state, these states may be generated in physical systems and their existence will not be restricted by the Pauli principle. Specifically, two types of triplet pairing correlations may be present in F/S systems and they are conventionally defined as [33],

$$f_0(\mathbf{r},t) \equiv \frac{1}{2}[\langle\psi_\uparrow(\mathbf{r},t)\psi_\downarrow(\mathbf{r},0)\rangle + \langle\psi_\downarrow(\mathbf{r},t)\psi_\uparrow(\mathbf{r},0)\rangle], \tag{1.9a}$$

$$f_1(\mathbf{r},t) \equiv \frac{1}{2}[\langle\psi_\uparrow(\mathbf{r},t)\psi_\uparrow(\mathbf{r},0)\rangle - \langle\psi_\downarrow(\mathbf{r},t)\psi_\downarrow(\mathbf{r},0)\rangle], \tag{1.9b}$$

where t is the time. It is clear that these $S = 1$ triplet correlations $f_0(\mathbf{r},t)$ and $f_1(\mathbf{r},t)$ correspond to $m = 0$ and $m = \pm 1$ (equal-spin pairing) components of the triplet pairing state, respectively. Both $m = 0$ and $m = \pm 1$ components must vanish when there is no time delay, i.e., $t = 0$, in agreement with the Pauli principle. Thus, the Pauli exclusion principle requires $f_0(\mathbf{r},t)$ and $f_1(\mathbf{r},t)$ to be odd in time [33]. For this reason, these types of pairing are also called "odd triplet superconductivity". It is important to note here that both types of the triplet pairing correlations in Eq. 1.9 may not be simultaneously induced in F/S systems as one has to consider the symmetry of the problem [34]. For the N/S layered structures in the absence of exchange fields, the effective Hamiltonian commutes with both $\mathbf{S}$ (the total spin operator of the Cooper pairs) and S_z. Therefore, the total spin and its z-component are conserved, and neither $f_0(\mathbf{r},t)$ nor $f_1(\mathbf{r},t)$ exists even when $t \neq 0$. For F/S layered structures with the exchange fields of all F layers aligned in the same direction (parallel or antiparallel), the effective Hamiltonian commutes with S_z, but not with $\mathbf{S}$, since the exchange fields break the rotational symmetry. As a result, only $f_0(\mathbf{r},t)$, that characterizes $m = 0$ can be induced when $t \neq 0$. For F/S systems with the presence of magnetic inhomogeneity, the effective Hamiltonian does not commute with $\mathbf{S}$ nor S_z. Therefore, both the $m = 0$ and the long-range $m = \pm 1$ components may emerge at $t \neq 0$.

It is worthwhile to note that the odd triplet pairing was first proposed by Berezinskii in 1974 to predict a possible superfluid phase of helium-3 [35]. Although this phase is not seen in later experiments on helium-3, it is observed in various kinds of experiments on F/S heterostructures. In an early experiment, it is found that the differential resistance of cobalt wires in cobalt/aluminum junctions exhibits a long-range decay length [36].

Although this finding conflicts with the short-range decay of singlet superconductivity in F/S bilayers, it is compatible with the picture of the odd triplet superconductivity. In another spectacular experiment on Josephson junctions [37], the long-range odd triplet superconductivity is also observed by comparing the critical current of the Josephson junctions containing cobalt and other magnetic alloys with the Josephson junctions containing only cobalt. In contrast to the junctions containing only cobalt, the critical current of junctions with noncollinear magnetic configurations (the magnetization of the magnetic alloys is canted with respect to that of Co layers) decays much more slowly as the thickness of the magnetic layers is increased. This is consistent with what we have discussed in the previous paragraph: the magnetic inhomogeneity is responsible for the generation of the $m = \pm 1$ triplet component and the proximity length of $m = \pm 1$ is large compared to that of the $m = 0$ triplet component and the usual singlet pair amplitudes. Additional experimental evidence for the long-range proximity effects is found in similar Josephson junctions with the insertion of magnetic layers made of holmium (Ho) [38], known to have a conical magnetic structure. In that experiment, the inherent inhomogeneous magnetism of Ho serves the purpose of generating the long-range triplet component.

F_1SF_2 trilayers, superconductors sandwiched between ferromagnets, are also important examples for researchers to study triplet correlations. By controlling the relative angle, α, of in-plane magnetizations in two F layers, the $m = \pm 1$ long-range triplet correlation can be induced when the magnetic moments of two F layers are noncollinear [34]. In addition, the dependence of superconducting transition temperatures on α have been extensively investigated both theoretically [28, 39, 40] and experimentally [41, 42, 43], owing to their important switching effects: by controlling the relative angle from the parallel to antiparallel configuration, the transition temperatures monotonically increase [44]. This switching effect is due to the fact that the average exchange field contributed by two F layers is smaller in the antiparallel than in the parallel configuration. This remarkable property makes F_1SF_2 trilayers ideal candidates for spin-valve devices as one has the freedom to manipulate the supercurrent by changing this misorientation angle.

The study of spin-polarized transport and tunneling in F/S heterostructures is another important subject in this field [14]. We have mentioned in the beginning of this

section that the process of the Andreev reflection is closely related to superconducting proximity effects. As a consequence of the Andreev reflection, the tunneling conductance in N/S bilayers is predicted to be twice the normal-state tunneling conductance, provided the bias is sufficiently small and the interfacial barrier is very weak [45]. However, if the normal metal is replaced with a half metal, the Andreev reflection of a spin-down hole associated with the incident spin-up electron is forbidden. Therefore, the tunneling conductance in the subgap region, contributed mainly by the Andreev reflection, is completely suppressed. With the knowledge of the subgap tunneling conductance in the $I = 0$ and $I = 1$ limits, one can anticipate that the subgap conductance strongly depends on the strength of the ferromagnets. Indeed, this dependence has been theoretically predicted [46, 47, 48]. Furthermore, this dependence turns out to be an important experimental tool in determining the degree of spin-polarization in materials [49, 50].

Having seen the important role played by the inhomogeneous magnetization in F/S layered systems, the purpose of this thesis is to investigate and understand superconducting proximity effects and their associated switching phenomena in F/S heterostructures with *inhomogeneous magnetization*. In particular, we study two specific types of this kind of heterostructures: F_1F_2S trilayers and conical-ferromagnet/S bilayers. Motivated by the significant discoveries in F_1SF_2 superconducting spin valves, researchers are also interested in another type of spin valve: F_1F_2S trilayers. In stark contrast with the monotonic behavior of the transition temperatures, as functions of α, found in F_1SF_2 superconducting spin valves, the transition temperatures in F_1F_2S trilayers are often predicted [51, 52] to be minimized when the magnetizations of two F layers are perpendicular to each other, i.e., they are non-monotonic functions of α. In this thesis, we will demonstrate that in F_1F_2S trilayers the triplet pairing correlations play a key role in the non-monotonic behavior of the critical temperature through the conversion between the singlet and triplet states. The important α-dependence of transition temperatures and the connection between the transition temperature and odd triplet superconductivity have been confirmed very recently in experiments [53], which we will further analyze in Chap. 3. This significant property makes F_1F_2S layered structures ideal candidates for applications in superconducting spin valves.

In addition to controlling T_c by varying α, we also investigate valve effects on the

charge and spin transport in F_1F_2S trilayers. In previous "non-self-consistent" theoretical studies of F/S bilayers, the superconducting proximity effects are neglected by approximating the singlet pair amplitudes as step functions that vanish in the F regions [46, 47, 48]. Even so, these theoretical results suggest nontrivial qualitative behavior of tunneling conductances due to the effect of an exchange interaction on the Andreev reflections, as discussed earlier. However, to fully take into account proximity effects, self-consistent superconducting order parameters are needed when attempting to both qualitatively and quantitatively study these transport properties [54]. Only when the self-consistency condition is satisfied can the proximity effects be correctly described. Therefore, one of our purposes in this thesis is to put forward a self-consistent approach incorporating proximity effects to study the transport properties in F_1F_2S spin valves. We will show that the self-consistency condition is necessary to ensure that conservation laws are satisfied.

Inspired by the recent experiment [38] on the Josephson junctions, made by sandwiching Ho layers between superconductors, we present in this thesis our theoretical studies on equilibrium properties of conical-ferromagnet/S bilayers. For these bilayers, we are concerned with the interplay between the inherent conical magnetic texture and the proximity effects and, most importantly, their connections to the odd triplet superconductivity. Many of the features observed in experiment such as the oscillation of critical currents are consistent with our theoretical results [55]. In addition, we find a unique reentrant phenomenon that can occur in the conical-ferromagnet/S bilayers: for a range of thicknesses of the magnetic layer, the superconductivity is reentrant with temperature T, that is, as one lowers T the systems turns superconducting, and when T is further lowered it turns normal again. This is the first truly reentrant transition predicted in electronic systems.

This thesis is organized as follows. In Chap. 2, we theoretically study several aspects on the equilibrium properties of F_1F_2S trilayers, including the critical temperatures, T_c, and other relevant quantities. We find, as mentioned above, that $T_c(\alpha)$ is in general a non-monotonic function and can be substantiated by evaluating the condensation free energy. We also study the α-dependence of the odd triplet pairing correlations and their long-range nature. We discuss important implications from the density of states (DOS) in proximity effects. The reverse proximity effects that describe how the magnetization

is modified near the F/S interface are also investigated.

In Chap. 3, we compare our theoretical T_c results of F_1F_2S trilayers with experiments. The non-monotonic behavior of $T_c(\alpha)$ is observed in experiments. We theoretically find that this behavior is anti-correlated with the odd triplet superconductivity: the triplet pairing correlations are maximized when $T_c(\alpha)$ is at its minimum. This is confirmed by experiments.

In Chap. 4, we present studies on the conical-ferromagnet/S bilayers. We investigate the relation between T_c and the thickness d_F of the magnetic layer. We find that the oscillations of $T_c(d_F)$ curves are governed by both the intrinsic periodicity of the magnetization and the characteristic length, ξ_F, associated with the proximity effects. In addition to the reentrance with d_F, we also report examples that can exhibit unusual reentrance with T. We find that both the $m = 0$ and $m = \pm 1$ triplet components can be generated due to the inhomogeneous nature of the conical ferromagnet. The reverse proximity effects and the DOS are also investigated.

In Chap. 5, we compare our theoretical fit to transition temperatures with experimental data of conical-ferromagnet/S bilayers, and find a good agreement between the two [56].

In Chap. 6, we first introduce a self-consistent method, that properly takes into account the proximity effects, to compute transport quantities in F_1F_2S trilayers. Then, we study the α-dependencies of tunneling conductances. We also investigate the important spin transport properties such as the spin transfer torque and spin currents.

In the beginning of each of the following chapters, we will first look back to the important physical consequences of proximity effects in systems of interest in a greater detail. The materials in each chapter are self-contained yet linked to other related chapters via cross-references.

1.3 Bogoliubov-de Gennes equations

Before moving on to the next chapter, we present a general scheme of our theoretical methods. The methods section in each of the following chapters will then diverge further in pertaining to its specific topic. We adopt the Bogoliubov-de Gennes (BdG) [16, 57] equations and numerically find the self-consistent solutions. Other theoretical methods

to study the proximity effects in F/S layered structures include solving the quasiclassical Eilenberger and Usadel equations. However, unlike the BdG equations, they are usually not sufficient in dealing with cases when the F layers in F/S systems are strong ferromagnets [13], since the oscillation period of pair amplitudes is comparable to the Fermi wavevector (see Eq. 1.8). On the other hand, approaches based on BdG equations are appropriate for studying F/S layered structures in the clean limit.

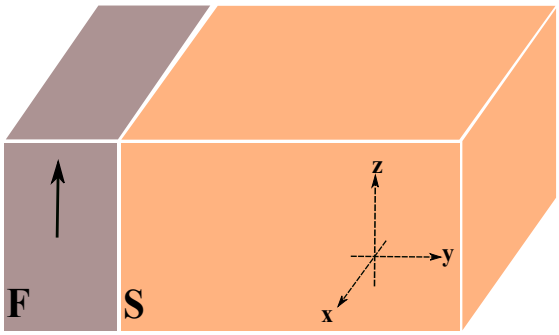

Figure 1.2: Schematic behavior of the F/S bilayers. The exchange field, indicated by an arrow, is a constant inside the F layer and along the z-axis. We assume the system is infinite in the x-z plane and finite in the y-direction.

Because the F/S (or N/S) layered structures are inhomogeneous in space, one needs to extend the effective BCS Hamiltonian, Eq. 1.1, in the original BCS theory to the following expression,

$$\begin{aligned}\mathcal{H}_{eff} &= \int d^3r \left\{ \sum_{\sigma} \psi^{\dagger}_{\sigma}(\mathbf{r}) \left(-\frac{\boldsymbol{\nabla}^2}{2m} - E_F \right) \psi_{\sigma}(\mathbf{r}) + \sum_{\sigma,\sigma'} \psi^{\dagger}_{\sigma}(\mathbf{r}) U_{\sigma\sigma'}(\mathbf{r}) \psi_{\sigma'}(\mathbf{r}) \right. \\ &\left. + \frac{1}{2} \left[\sum_{\sigma,\sigma'} (i\sigma_y)_{\sigma\sigma'} \Delta(\mathbf{r}) \psi^{\dagger}_{\sigma}(\mathbf{r}) \psi^{\dagger}_{\sigma'}(\mathbf{r}) + H.c. \right] \right\}, \end{aligned} \tag{1.10}$$

where σ and σ' are spin indices, $\boldsymbol{\sigma}$ are Pauli matrices, $H.c.$ denotes the Hermitian conjugate, and $U_{\sigma\sigma'}$ is the spin-dependent single particle potential. Here and in subsequent chapters, we adopt the natural units $\hbar = k_B = 1$. As a simple example, we assume that there is no Fermi wavevector mismatch between F and S, and E_F represents the Fermi energy for both F and S. The pair potential $\Delta(\mathbf{r}) \equiv g(\mathbf{r})F(\mathbf{r})$ in Eq. 1.10 is a product of the superconducting coupling constant, $g(\mathbf{r})$, and the pair amplitudes, $F(\mathbf{r}) = \langle \psi_{\uparrow}(\mathbf{r}) \psi_{\downarrow}(\mathbf{r}) \rangle$, as defined earlier. The superconducting coupling constant, $g(\mathbf{r})$,

depends on the superconducting properties of the material. In non-superconducting layers, $g(\mathbf{r})$ vanishes, whereas in superconductors, $g(\mathbf{r})$ is taken as the usual BCS coupling constant for homogeneous superconductors and can be obtained from Eq. 1.3.

This effective BCS Hamiltonian, Eq. 1.10, is generic in describing F/S layered structures. For simplicity, let us consider an example of F/S bilayers with constant exchange fields $\mathbf{h}(\mathbf{r}) = h\hat{\mathbf{z}}$ that only resides in F layers. The schematic geometry is shown in Fig. 1.2. For the spin-dependent single particle potential, we have $U_{\sigma\sigma'} = -(\mathbf{h}\cdot\boldsymbol{\sigma})_{\sigma\sigma'} = -(h\sigma_z)_{\sigma\sigma'}$ in F layers. In close analogy to our discussion in the previous section, our goal is to convert the effective Hamiltonian into a diagonalized form, that is,

$$H_{eff} = E_g + \sum_n \epsilon_n \gamma_n^\dagger \gamma_n, \tag{1.11}$$

where E_g is the superconducting ground state energy, with help from the generalized Bogoliubov transformation,

$$\psi_\uparrow(\mathbf{r}) = \sum_n \left[u_{n\uparrow}(\mathbf{r})\gamma_n - v_{n\uparrow}(\mathbf{r})\gamma_n^\dagger \right] \tag{1.12a}$$

$$\psi_\downarrow(\mathbf{r}) = \sum_n \left[u_{n\downarrow}(\mathbf{r})\gamma_n + v_{n\downarrow}(\mathbf{r})\gamma_n^\dagger \right]. \tag{1.12b}$$

By taking the commutators of H_{eff} with γ_n and $\gamma_n^\dagger$, we have the following conditions:

$$[H_{eff}, \gamma_n] = -\epsilon_n \gamma_n \tag{1.13a}$$

$$[H_{eff}, \gamma_n^\dagger] = \epsilon_n \gamma_n. \tag{1.13b}$$

When performing the generalized Bogoliubov transformation, Eq. 1.12, and using the above conditions, one can obtain two sets of coupled equations. One of them is the following,

$$\epsilon_n u_{n\uparrow}(\mathbf{r}) = \left(\frac{\mathbf{p}^2}{2m} - E_F - h(\mathbf{r}) \right) u_{n\uparrow}(\mathbf{r}) + \Delta(\mathbf{r}) v_{n\downarrow}(\mathbf{r}) \tag{1.14a}$$

$$\epsilon_n v_{n\downarrow}(\mathbf{r}) = -\left(\frac{\mathbf{p}^2}{2m} - E_F + h(\mathbf{r}) \right) v_{n\downarrow}(\mathbf{r}) + \Delta(\mathbf{r}) u_{n\uparrow}(\mathbf{r}), \tag{1.14b}$$

where $u_{n\uparrow}(\mathbf{r})$ and $v_{n\downarrow}(\mathbf{r})$, defined in Bogoliubov transformations, represent particle-like and hole-like wavefunctions, respectively. The other set of the BdG equations for $u_{n\downarrow}(\mathbf{r})$

and $v_{n\uparrow}(\mathbf{r})$ reads,

$$\epsilon_n u_{n\downarrow}(\mathbf{r}) = \left(\frac{\mathbf{p}^2}{2m} - E_F + h(\mathbf{r})\right) u_{n\downarrow}(\mathbf{r}) + \Delta(\mathbf{r}) v_{n\uparrow}(\mathbf{r}) \tag{1.15a}$$

$$\epsilon_n v_{n\uparrow}(\mathbf{r}) = -\left(\frac{\mathbf{p}^2}{2m} - E_F - h(\mathbf{r})\right) v_{n\uparrow}(\mathbf{r}) + \Delta(\mathbf{r}) u_{n\downarrow}(\mathbf{r}). \tag{1.15b}$$

There exists a particle-hole symmetry in BdG equations: if $\binom{u_{n\uparrow}}{v_{n\downarrow}}$ is an eigenfunction with eigenvalue ϵ_n, then $\binom{v_{n\downarrow}}{-u_{n\uparrow}}$ is also an eigenfunction with eigenvalue $-\epsilon_n$. The particle-hole symmetry permits one to determine the eigensolutions for $\binom{u_{n\uparrow}}{v_{n\downarrow}}$ and $\binom{u_{n\downarrow}}{v_{n\uparrow}}$ from only solving Eq. 1.14, by allowing both positive and negative eigenenergies. The pair potential $\Delta(\mathbf{r})$ can be expressed in terms of the quasiparticle and quasihole wavefunctions,

$$\Delta(\mathbf{r}) = \frac{g(\mathbf{r})}{2} \sum_n{}' \left[u_{n\uparrow}(\mathbf{r}) v_{n\downarrow}(\mathbf{r}) + u_{n\downarrow}(\mathbf{r}) v_{n\uparrow}(\mathbf{r})\right] \tanh(\frac{\epsilon_n}{2T}), \tag{1.16}$$

where the prime sign denotes the existence of an energy cutoff for the sum. It is apparent that the solutions to the BdG equations must be solved self-consistently.

If we consider the geometry of F/S structures, as depicted in Fig. 1.2, and assume that the system is infinite in the x-z plane and finite in the y direction, then the above three-dimensional problem is reduced to a quasi-one-dimensional problem. These assumptions allow us to use the set $\exp(i\mathbf{k}_\perp \cdot \mathbf{r})$, where $\mathbf{k}_\perp$ is the transverse momentum, to denote eigenfunctions for the x-z plane. In the y direction, one can numerically solve Eq. 1.14 by expanding the quasiparticle wavefunctions and operators in terms of an appropriate set of orthonormal functions. This expansion enables us to look for self-consistent eigenenergies and eigenfunctions numerically. With the knowledge of self-consistent eigenfunctions, all other important physical quantities, e.g., the magnetization and local density of states can be computed by applying the generalized Bogoliubov transformations. The self-consistent condition is crucial when studying the proximity effects in F/S systems, as we will demonstrate its importance in the following chapters. The generalization of BdG equations to F_1F_2S and Ho/S heterostructures are discussed in more detail in the methods section of subsequent chapters.

Chapter 2

Proximity effects and triplet correlations in ferromagnet/ ferromagnet/superconductor nanostructures

2.1 Introduction

Although ferromagnetism and s-wave superconductivity are largely incompatible because of the opposite nature of the spin structure of their order parameters, they can still coexist in nanoscale F/S systems via superconducting proximity effects [13, 58]. As mentioned in the previous chapter, the fundamental feature of proximity effects in F/S heterostructures is the damped oscillatory behavior of the superconducting order parameter in the F regions [15]. Qualitatively, the reason behind this behavior is because a spin singlet Cooper pair acquires a finite momentum when it encounters the exchange field when entering the ferromagnet. This affects the momenta of individual electrons that compose the Cooper pairs, and modifies both the ordinary and Andreev reflection [12]. As discussed in Chap. 1, this unusual behavior of the superconducting order parameter leads to an oscillatory behavior of the dependence of the superconducting transition temperature, T_c, on the thickness d_F of the ferromagnet in F/S bilayers [13, 19, 22].

Because of these oscillations, the superconductivity may even disappear in a certain range of F thicknesses and reenter just above that range [20, 21, 23, 24, 26, 27, 28].

Another remarkable fact related to F/S proximity effects is that the long-range triplet pairing correlations may be induced in F/S systems where S is in the ordinary s-wave pairing state (see Sec. 1.2 and Refs. [29, 30, 31, 32, 33, 34, 59, 60, 61, 62]). These long-range correlations can extend deep into both the F and S regions. The magnetic inhomogeneity arising from the presence of ferromagnets in F/S systems is responsible for this type of triplet pairing. The components of the triplet pairing correlations are restricted, because of conservation laws, by the magnetic structure in the F layers: only the total spin projection corresponding to the $m = 0$ component can be induced when the exchange fields arising from the ferromagnetic structure are all aligned in the same direction, while all three components ($m = 0, \pm 1$) can arise when the exchange fields are not aligned. Unlike the singlet pair amplitudes, the length scale of the induced long-range triplet pairing correlations is comparable to that of the usual slow decay associated with nonmagnetic metal proximity effects. Recently, experimental observations of long-range spin triplet supercurrents have been reported in several multilayer systems [37, 63, 64], and also in Nb/Ho layered systems [38]. In the last case, the requisite magnetic inhomogeneity arises from the conical magnetic structure inherent to the rare earth compound, Ho, which also gives rise to oscillations [65] in T_c (studies on this particular system will be presented in Chaps. 4 and 5).

Both the short and long spatial range of the oscillatory singlet and odd triplet correlations in the ferromagnetic regions permit control over the critical temperature, T_c, that is, the switching on or off of superconductivity. The long-range propagation of equal-spin triplet correlations in the ferromagnetic regions was shown to contribute to a spin-valve effect that varies with the relative magnetization in the F layers [51]. With continual interest in nonvolatile memories, a number of spin valve type of structures have been proposed. These use various arrangements of S and F layers to turn superconductivity on or off. As mentioned in Chap. 1, recent theoretical work suggests that when two ferromagnet layers are placed in direct contact and adjacent to a superconductor, new types of spin valves [51, 66, 67, 68] or Josephson junctions [29, 69] with interesting and unexpected behavior can ensue. For an F_1F_2S superconducting memory device [66], the oscillatory decay of the singlet correlations can be manipulated by switching the

relative magnetization in the F layers from parallel to antiparallel by application of an external magnetic field. It has also been shown [51], using quasiclassical methods, that for these F_1F_2S structures the critical temperature can have a minimum at a relative magnetization angle that lies between the parallel and antiparallel configuration. This is in contrast with F_1SF_2 trilayers, where (as indicated by both [26, 39, 40, 44] theory and experiment [41, 42, 70]) the behavior of T_c with the relative angle is strictly monotonic, with a minimum when the magnetizations are parallel and a maximum when antiparallel. For SF_1F_2S type structures, the exchange field in these magnets can increase the Josephson current [29], or, in the case of noncollinear alignment [69], induce triplet correlations and discernible signatures in the corresponding density of states.

Following up on this work, an F_1F_2S spin switch was experimentally demonstrated using CoO_x/Fe1/Cu/Fe2/In multilayers [71]. Supercurrent flow through the sample was completely inhibited by changing the mutual orientation of the magnetizations in the two adjacent F layers. A related phenomenon was reported [72] for a similar multilayer spin valve, demonstrating that the critical temperature can be higher for the parallel orientation of relative magnetizations. A spin-valve like effect was also experimentally realized [73, 74] in Fe/V superlattices, where antiferromagnetic coupling between the Fe layers permits gradual rotation of the relative magnetization direction in the F_1 and F_2 layers.

As already mentioned, the $T_c(\alpha)$ behavior in the F_1F_2S geometry is in stark contrast to that observed in the more commonly studied spin switch structures involving F_1SF_2 configurations. There, as the angle α between the (coplanar) magnetizations increases from zero (parallel, P, configuration) to 180° (antiparallel, AP, configuration), T_c increases monotonically. For these systems, it has also been demonstrated that under many conditions they can be made to switch from a superconducting state (at large α) to a normal one [28, 41] in the P configuration by flipping of the magnetization orientation in one of the F layers. The AP state, however, is robust: it is always the lowest energy state regardless of relative strength of the ferromagnets, interface scattering, and geometrical variations. The principal reason for this behavior stems from the idea that the average exchange field overall is smaller for the AP relative orientation of the magnetization. Early experimental data on T_c^{AP} and T_c^P, where T_c^{AP} and T_c^P are the transition temperatures for the AP and P configurations, was obtained in

CuNi/Nb/CuNi [41]. There $\Delta T_c \equiv T_c^{AP} - T_c^P > 0$, was found to be about 6 mK. Later, it was found that ΔT_c can be as large as 41 mK in Ni/Nb/Ni trilayers [42]. Recently, the angular dependence of T_c of F_1SF_2 systems was also measured in CuNi/Nb/CuNi trilayers and its monotonic behavior found to be in good agreement with theory [44]. In addition to the experimental work, the thermodynamic properties of F_1SF_2 nanostructures were studied quasiclassically by solving the Usadel equations [40]. It was seen that these properties are strongly dependent on the mutual orientation of the F layers. The difference in the free energies of the P and AP states can be of the same order of magnitude as the superconducting condensation energy itself. In light of the differences between F_1F_2S and F_1SF_2, it appears likely that a full microscopic theory is needed that accounts for the geometric interference effects and the quantum interference effects that are present due to the various scattering processes.

In this chapter, we consider several aspects of the proximity effects that arise in F_1F_2S spin switch nanostructures. We consider the arbitrary relative orientation of the magnetic moments in the two F layers and study both the singlet and the induced odd triplet correlations in the clean limit through a fully self-consistent solution of the microscopic BdG equations. We also calculate the critical temperature by solving the linearized BdG equations. As a function of the angle α, it is often non-monotonic, possessing a minimum that lies approximately midway between the parallel and antiparallel configurations. Reentrant behavior occurs when this minimum drops to zero. We find that there are induced odd triplet correlations, and we study their behavior. These correlations are often found to be long ranged in both the S and F regions. These findings are consistent with the single particle behavior exhibited by the density of states and magnetic moment in these structures.

2.2 Methods

We consider an F_1F_2S trilayer structure infinite in the x-z plane with a total length d in the y direction, which is normal to the interfaces. The inner ferromagnetic layer (F_2) of width d_{F2} is adjacent to the outer ferromagnet (F_1) of width d_{F1}, and the superconductor has width d_S (see Fig. 2.1). The magnetizations in the F_1 and F_2 layers form angles $\alpha/2$ and $-\alpha/2$, respectively, with the axis of quantization z. The

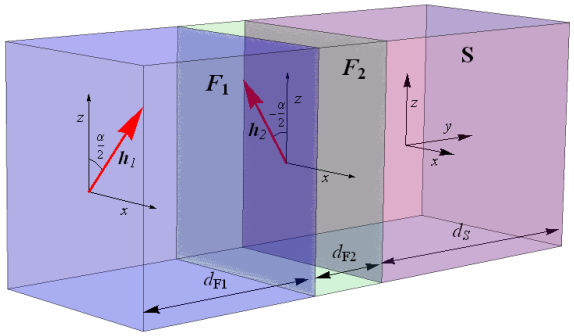

Figure 2.1: Schematic of the F_1F_2S trilayer. The outer ferromagnetic layer F_1 has a magnetization oriented at an angle $\alpha/2$ in the x-z plane, while the inner ferromagnet, F_2, has a magnetization orientation at an angle $-\alpha/2$ in the x-z plane. All relevant widths are labeled.

superconductor is of the conventional s-wave type. We describe the magnetism of the F layers by an effective exchange field $\mathbf{h}(y)$ that vanishes in the S layer. We assume that interface scattering barriers are negligible.

To accurately describe the behavior of the quasiparticle ($u_{n\sigma}$) and quasihole ($v_{n\sigma}$) amplitudes with spin σ, we use the BdG formalism. In our geometry, the BdG equations can be written down after a few steps, described in Ref. [34] and Sec. 1.3, in the quasi-one-dimensional form:

$$\begin{pmatrix} \mathcal{H}_0 - h_z & -h_x & 0 & \Delta(y) \\ -h_x & \mathcal{H}_0 + h_z & \Delta(y) & 0 \\ 0 & \Delta(y) & -(\mathcal{H}_0 - h_z) & -h_x \\ \Delta(y) & 0 & -h_x & -(\mathcal{H}_0 + h_z) \end{pmatrix} \begin{pmatrix} u_{n\uparrow}(y) \\ u_{n\downarrow}(y) \\ v_{n\uparrow}(y) \\ v_{n\downarrow}(y) \end{pmatrix} = \epsilon_n \begin{pmatrix} u_{n\uparrow}(y) \\ u_{n\downarrow}(y) \\ v_{n\uparrow}(y) \\ v_{n\downarrow}(y) \end{pmatrix}, \quad (2.1)$$

where $\mathcal{H}_0 \equiv -\frac{1}{2m}\frac{\partial^2}{\partial y^2} + \epsilon_\perp - E_F$ is the usual single particle Hamiltonian for the quasi-one-dimensional problem, with $\epsilon_\perp$ denoting the kinetic energy associated with the transverse direction, $\mathbf{h}(y) = (h_x(y), 0, h_z(y))$ is the exchange field in the F layers, $\Delta(y)$ is the pair potential, taken to be real, and the wavefunctions $u_{n\sigma}$ and $v_{n\sigma}$ are the standard coefficients that appear when the usual field operators ψ_σ, with the time dependence,

are expressed in terms of the Bogoliubov transformation:

$$\psi_\sigma(\mathbf{r},t) = \sum_n \left(u_{n\sigma}(\mathbf{r})\gamma_n e^{-i\epsilon_n t} + \eta_\sigma v_{n\sigma}(\mathbf{r})\gamma_n^\dagger e^{i\epsilon_n t} \right), \tag{2.2}$$

where $\eta_\sigma \equiv 1(-1)$ for spin down (up). We must include all four spin components since the exchange field in the ferromagnets destroys the spin rotation invariance. Furthermore, $u_{n\sigma}$ and $v_{n\sigma}$ are not decoupled, as the case of a simple F/S bilayer described in Sec. 1.3. To ensure that the system is in an, at least locally, thermodynamically stable state, Eq. 2.1 must be solved jointly with the self-consistency condition, Eq. 1.16, for the pair potential.

Within our assumptions, the triplet correlations are odd in time, in agreement with the Pauli principle, and hence vanish at $t = 0$. Therefore we will consider the time dependence of the triplet correlation functions defined in Eq. 1.9, By using Eq. 2.2, Eq. 1.9 can be rewritten in terms of the quasiparticle amplitudes [33, 34]:

$$f_0(y,t) = \frac{1}{2}\sum_n \left[u_{n\uparrow}(y)v_{n\downarrow}(y) - u_{n\downarrow}(y)v_{n\uparrow}(y) \right] \zeta_n(t), \tag{2.3a}$$

$$f_1(y,t) = \frac{1}{2}\sum_n \left[u_{n\uparrow}(y)v_{n\uparrow}(y) + u_{n\downarrow}(y)v_{n\downarrow}(y) \right] \zeta_n(t), \tag{2.3b}$$

where $\zeta_n(t) \equiv \cos(\epsilon_n t) - i\sin(\epsilon_n t)\tanh(\epsilon_n/2T)$, and *all* positive energy states are in general summed over.

Besides the pair potential and the triplet amplitudes, we can also determine various physically relevant single-particle quantities. One such important quantity is the local magnetization, which can reveal details of the well-known (see among many others, Refs. [13, 16, 75, 76, 77, 78]) reverse proximity effect: the penetration of the magnetization into S. The local magnetic moment $\mathbf{m}$ will depend on the coordinate y and it will have in general both x and z components, $\mathbf{m} = (m_x, 0, m_z)$. We define $\mathbf{m} = -\mu_B \langle \sum_\sigma \Psi^\dagger \boldsymbol{\sigma} \Psi \rangle$, where $\Psi^\dagger \equiv (\psi_\uparrow, \psi_\downarrow)$. In terms of the quasiparticle amplitudes calculated from the self-consistent BdG equations, we have,

$$m_x(y) = -2\mu_B \sum_n \Big\{ u_{n\uparrow}(y)u_{n\downarrow}(y)f_n - v_{n\uparrow}(y)v_{n\downarrow}(y)(1-f_n) \Big\}, \tag{2.4a}$$

$$m_z(y) = -\mu_B \sum_n \Big\{ (|u_{n\uparrow}(y)|^2 - |u_{n\downarrow}(y)|^2)f_n + (|v_{n\uparrow}(y)|^2 - |v_{n\downarrow}(y)|^2)(1-f_n) \Big\}, \tag{2.4b}$$

where f_n is the Fermi function of ϵ_n, and μ_B is the Bohr magneton.

A very useful tool in the study of these systems is tunneling spectroscopy, where information measured by an STM can reveal the local DOS (LDOS). Therefore we have also computed here the LDOS $N(y,\epsilon)$ as a function of y. We have $N(y,\epsilon) \equiv N_\uparrow(y,\epsilon) + N_\downarrow(y,\epsilon)$, where,

$$N_\sigma(y,\epsilon) = \sum_n [u^2_{n\sigma}(y)\delta(\epsilon - \epsilon_n) + v^2_{n\sigma}(y)\delta(\epsilon + \epsilon_n)], \quad \sigma = \uparrow, \downarrow . \tag{2.5}$$

The transition temperature can be calculated for our system by finding the temperature at which the pair potential vanishes. It is much more efficient, however, to find T_c by linearizing [79] the self-consistency equation near the transition, leading to the form

$$\Delta_i = \sum_q J_{iq}\Delta_q, \tag{2.6}$$

where the Δ_i are expansion coefficients of the position dependent pair potential in the chosen basis, and the J_{iq} are the appropriate matrix elements with respect to the same basis. The somewhat lengthy details of their evaluation are given in Ref. [79].

To evaluate the free energy, F, of the self-consistent states, we use the convenient expression [80],

$$F = -2T\sum_n \ln\left[2\cosh\left(\frac{\epsilon_n}{2T}\right)\right] + \left\langle \frac{\Delta^2(y)}{g(y)} \right\rangle_s , \tag{2.7}$$

where here $\langle \ldots \rangle_s$ denotes spatial average. The condensation free energy, ΔF, is defined as $\Delta F \equiv F_S - F_N$, where F_S is the free energy of the superconducting state, and F_N is that of the non-superconducting system. We compute F_N by setting $\Delta \equiv 0$ in Eqs. 2.1 and 2.7.

2.3 Results

In this thesis, when presenting our theoretical results, we adopt dimensionless variables and all dimensionless lengths are denoted by capital letters. In this chapter, all lengths are measured in units of the inverse of k_F. Thus, for example, $Y \equiv k_F y$. The exchange field strength is measured by the dimensionless parameter $I \equiv h/E_F$, where E_F is the band width in S and F (we assume here that there is no Fermi wavevector mismatch),

and h the magnitude of the exchange field $\mathbf{h}$. In describing the two F layers, the subscripts 1 and 2 denote (as in Fig. 2.1) the outer and inner layers, respectively. Whenever the two F layers are identical in some respect, the corresponding quantities are given without an index. Thus, I_2 would refer to the inner layer while simply I refers to both, when appropriate. We study a relatively wide range of thicknesses D_{F1} for the outer layer, but there would be little purpose in studying thick inner layers beyond the range of the standard singlet proximity effect in the magnets. In all cases, we have assumed a superconducting correlation length corresponding to $\Xi_0 = 100$ and measure all temperatures in units of T_c^0, the transition temperature of *bulk* S material. The quantities Ξ_0 and T_c^0 suffice to characterize the BCS singlet material we consider. We use $D_S = 1.5\Xi_0$ unless, as otherwise indicated, a larger value is needed to study penetration effects. Except for the transition temperature itself, results shown were obtained in the low temperature limit. For the triplet amplitudes, dimensionless times τ are defined as $\tau \equiv \omega_D t$. Except for this definition, the cutoff frequency does not play a significant role in the results.

2.3.1 Transition temperature

The transition temperature T_c is calculated directly from the linearization method described in Sec. 2.2. Some of the results are shown in Fig. 2.2. In this figure, we have taken both F layers to be identical and hence both relatively thin. All three panels in the figure display T_c, normalized to T_c^0, as a function of the angle α. The figure dramatically displays, as anticipated in Sec. 2.1, that as opposed to F_1SF_2 trilayers, T_c does not usually, in our present case, monotonically increase as α increases from 0° to 180°, but on the contrary it often has a minimum at a value of α typically below 90°.

The top panel, which shows results for several intermediate values of I with $D_F = 10$, illustrates the above statements. T_c is found in this case to be monotonic only at the smallest value of I ($I = 0.02$) considered. The non-monotonic behavior starts to set in at around $I = 0.04$ and then continues with the minimum T_c remaining at about $\alpha = 80^\circ$. This is not a universal value: we have found that for other geometric and material parameters the position of the minimum can be lower or higher. In the middle panel, we consider a fixed value of $I = 0.1$ and several values of D_F. This panel makes another important point: the four curves plotted in the top panel and the four ones

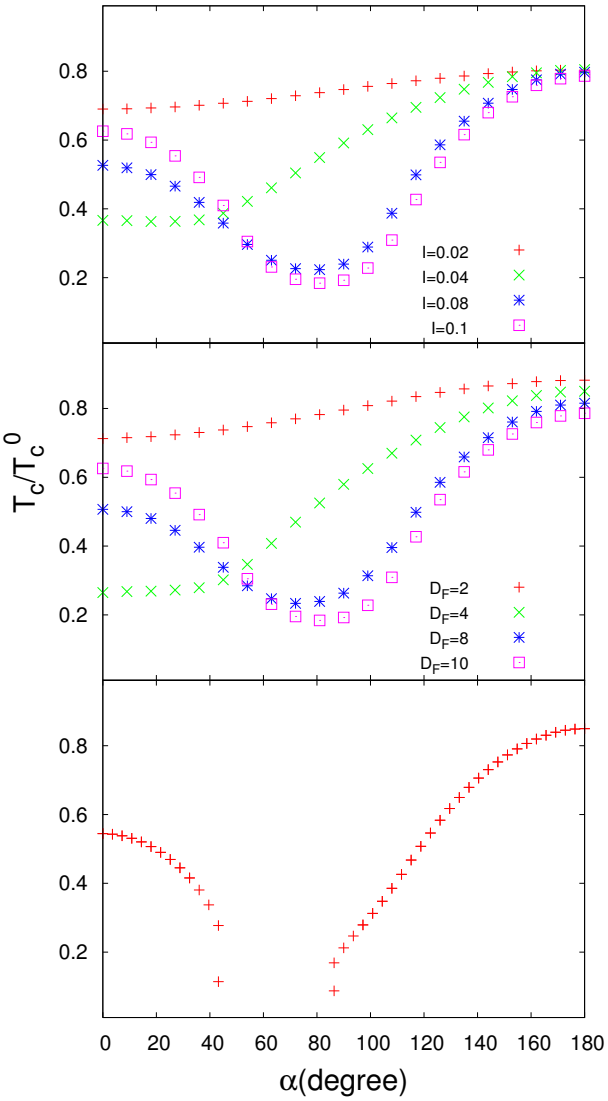

Figure 2.2: Calculated transition temperatures T_c, normalized to T_c^0. In this figure, the two F layers are identical, $D_{F1} = D_{F2} \equiv D_F$ and $I_1 = I_2 \equiv I$. In the top panel, this ratio is shown vs α for different exchange fields at $D_F = 10$. In the middle panel, the same ratio is plotted again vs α for different values of D_F at $I = 0.1$. In the bottom panel, T_c vs α is shown for $D_F = 6$ and $I = 0.15$, a case where reentrance with the angle occurs.

in this panel correspond to identical values of the product $D_F I$. The results, while not exactly the same, are extremely similar and confirm that the oscillations in T_c are determined by the overall periodicity of the Cooper pair amplitudes in the F materials as determined by the difference between the up and down Fermi wavevectors, which is approximately proportional [16] to $1/I$ in the range of I shown.

In the lowest panel of the figure, we show that reentrance with α can occur in these structures. The results there are for $D_F = 6$ and at $I = 0.15$, a value slightly larger than those considered in the other panels. While such reentrance is not the rule, we have found that it is not an exceptional situation either: the minimum in T_c at intermediate α can simply drop to zero, resulting in reentrance. The origin of this reentrance stems from the presence of triplet correlations due to the inhomogeneous magnetization and the usual D_F reentrance in F/S bilayers [13, 20, 21, 26, 27, 28, 79], that is, the periodicity of the pair amplitudes mentioned above.

2.3.2 Pair amplitude: singlet

We now turn to the behavior of the standard, singlet pair amplitude $F(y)$, defined as usual via $\Delta(y) \equiv g(y)F(y)$ and Eq. 1.16, as evaluated from the self-consistent calculations described in Sec. 1.3 and 2.2. The behavior of $F(y)$ is rather straightforwardly described, and has some features representative of conventional proximity effects found in other ferromagnet/superconductor configurations, such as F/S or F_1SF_2 structures. An example is shown in Fig. 2.3, where the spatial behavior of $F(y)$ is shown for a few cases of exchange fields differing in orientation and magnitude, as well as ferromagnet widths.

The top panel shows results for $F(Y)$ as a function of position, at $I = 0.1$, and for several values of α, at $D_F = 10$. We see that in the S layer, the pair amplitude rises steadily over a length scale of order of the correlation length. The variation of the overall amplitude in S with α reflects that of the transition temperature, as was depicted for this case by the (purple) squares in the top panel of Fig. 2.2. One sees that the non-monotonic trends observed in the critical temperature correlate well with the zero temperature pair amplitude behavior. In the F layers, we observe a more complicated behavior and oscillations with an overall smaller amplitude. These oscillations are characteristic of conventional F/S proximity effects, which in this case appear somewhat

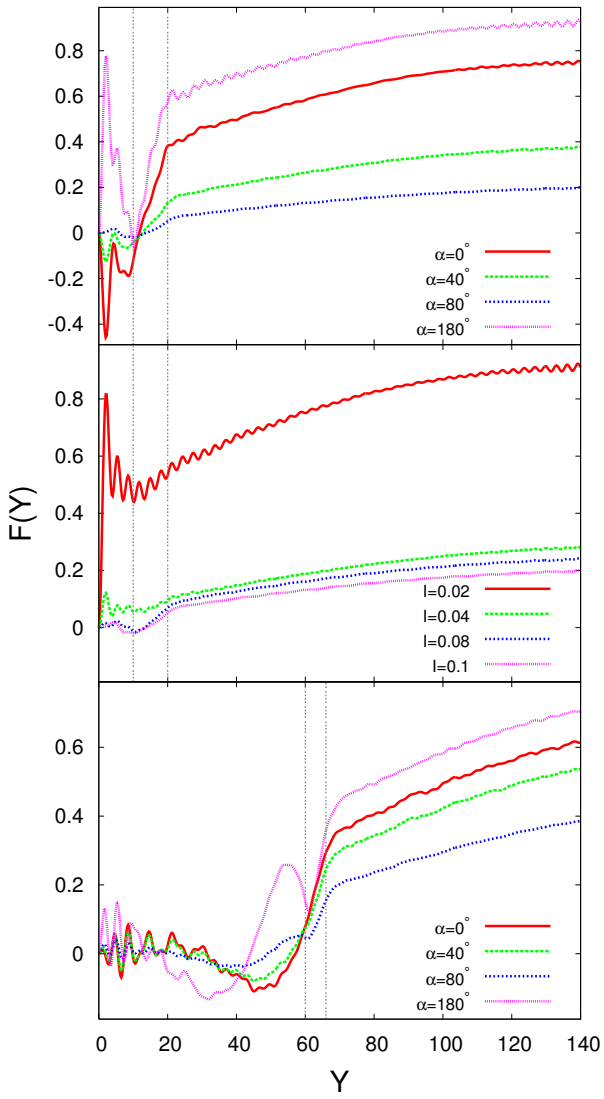

Figure 2.3: Calculated singlet pair amplitude $F(Y)$, normalized to its value in bulk S material, plotted vs $Y \equiv k_F y$. In the top panel, results are shown for different α at $I = 0.1$ and $D_F = 10$. The central panel depicts results for the same D_F, and illustrates the effect of different magnetic strengths, I, at fixed $\alpha = 80°$. The bottom panel shows $F(Y)$ for different α as in the top panel, except for a structure of differing magnet thicknesses: $D_{F1} = 60$, and $D_{F2} = 6$. The dashed vertical lines represent in each case the location of the F_1F_2 and F_2S interfaces.

chaotic because of reflections and interference at the F_1F_2 and end boundaries. This irregular spatial behavior is also due to the chosen value of I and the characteristic spatial periodicity $\approx 2\pi/I$ not matching D_F. These geometric effects can in some cases result in the amplitudes of the singlet pair oscillations in F_1, exceeding those in the superconductor near the interface.

In the central panel, results for several values of I and the same geometry as the top one are shown where the typical location of the minimum in T_c may occur at a relative magnetization angle of $\alpha \approx 80^\circ$. We see that for the case $I = 0.02$, where T_c is high and monotonic with α, singlet correlations are significant and they are spread throughout the entire structure. This is consistent with the top panel of Fig. 2.2, where the critical temperature is highest, and increases only slightly with α. For larger values of I, there is a strong T_c minimum near $\alpha = 80^\circ$ and consequently, the pair amplitude is much smaller. The weakening of the superconductivity in S inevitably leads to its weakening in the F layers.

The bottom panel demonstrates how the pair amplitude in the structure becomes modified when α is varied, in a manner similar to the top panel, except in this case the inner layer is thinner with $D_{F2} = 6$ and the outer layer is thicker with $D_{F1} = 60$. Comparing the top and bottom panels, we clearly see that geometric effects can be quite influential on the spatial behavior of singlet pairing correlations. In this case, the F_2 layer is too thin for $F(Y)$ to exhibit oscillations within it.

2.3.3 Triplet amplitudes

In this subsection, we discuss the induced triplet pairing correlations in our systems. As mentioned in Sec. 2.1, the triplet pairing correlations may coexist with the usual singlet pairs in F/S heterostructures, and their behavior is in many ways quite different; particularly, the characteristic proximity length can be quite large. As a function of the angle α, the possible existence of the different triplet amplitudes is restricted [33, 34] by conservation laws. For instance, at $\alpha = 0^\circ$ (parallel exchange fields) the $m = \pm 1$ component along our z axis of quantization, $f_1(y,t)$, must identically vanish, while f_0 is allowed. This is because at $\alpha = 0^\circ$ the S_z component of the total Cooper pair spin is conserved, although the total spin quantum number S is not. Neither quantity is conserved for an arbitrary α. For directions other than $\alpha = 0^\circ$, restrictions arising from

the symmetry properties can be inferred [34] most easily by projecting the quasiparticle amplitudes along a different axis in the x-z plane via a unitary spin rotation operator, U:

$$U(\theta) = \cos(\theta/2)\hat{\mathbf{1}} \otimes \hat{\mathbf{1}} - i\sin(\theta/2)\rho_z \otimes \sigma_y, \tag{2.8}$$

in the particle-hole space. For the antiparallel case, $\alpha = 180°$, following from the operation of spin rotation above, we have the inverse property that only f_1 components can be induced. In addition, the Pauli principle requires all triplet amplitudes to vanish at $t = 0$. We also note that with the usual phase convention taken here, namely that the singlet amplitude is real, the triplet amplitudes may generally have both real and imaginary parts. The results of triplet amplitudes shown here are calculated at zero temperature and are also normalized to the singlet pair amplitude of a bulk S material.

First, we present in Fig. 2.4 the case of a thick S layer ($D_S = 300$) with two thin F layers ($D_F = 10$). The two F layers have exchange fields of identical magnitude, corresponding to $I = 0.1$, and the angle α is varied. The dimensionless time chosen is $\tau = 4$ (the behavior is characteristic of all times in the relevant range). Of course, the results at $\tau = 0$ are found to vanish identically. As observed in this figure, the results for f_1 vanish at $\alpha = 0°$ and those for f_0 at $\alpha = 180°$ in agreement with the conservation law restrictions. We see that the triplet amplitudes can be quite long ranged in S: this is evident, with our phase convention, for the imaginary parts of f_0 and f_1 at $\alpha = 40°$. Thus, the triplet correlations for this particular magnetization orientation can penetrate all the way to the other end of the S side, even though the S layer is three coherence lengths thick. In addition, one can see that the antiparallel magnetizations in the F layers lead to both the real parts and the imaginary parts of f_1 being short ranged. Noncollinear relative orientations of the exchange fields in the inner and outer F layers may induce both long-range f_0 and f_1 components simultaneously. However, the triplet pairing correlations for $\alpha = 80°$ are not as long ranged as those for $\alpha = 40°$. This can be indirectly attributed to much weaker singlet amplitudes inside S in the former case: the overall superconductivity scale is still set by the singlet, intrinsic correlations.

Motivated by the long-range triplet amplitudes found above for an F_1F_2S structure with relatively thin F layers and a thick S layer, we next discuss, in Fig. 2.5, the case of a thicker outer ferromagnet layer with $D_{F1} = 60$, with $D_S = 150$. The values of τ and I are the same as in Fig. 2.4. Figure 2.5 shows that the triplet amplitudes are

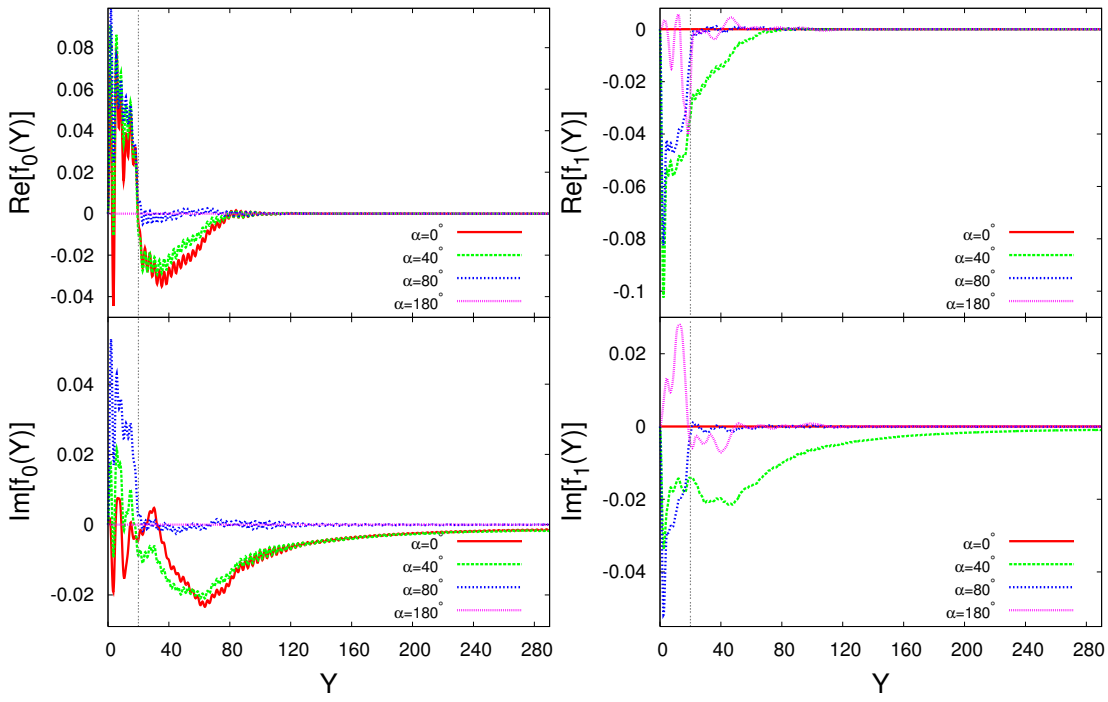

Figure 2.4: The Real and Imaginary parts of the normalized triplet amplitudes f_0 and f_1 (see text) plotted vs Y for a sample with $D_F = 10$, $D_S = 300$ and $I = 0.1$, at dimensionless time $\tau = 4.0$. Results are plotted for different values of α as indicated. See text for discussion. Vertical lines indicate, in this and the next three figures, the F_2S interface. For clarity, the F_1F_2 interface is not included.

more prominent in the F than in the S regions. There is also an underlying periodicity that is superimposed with apparent interference effects, with a shorter period than that found in the singlet pair amplitudes (see bottom panel, Fig. 2.3). Also, the imaginary component of f_0 penetrates the superconductor less than the imaginary f_1 component. For the real f_1 component, the exchange field of the inner layer produces a valley near the interface in the F regions. This feature is most prominent when the exchange fields are antiparallel, in which case the equal-spin triplet correlations are maximized. Aside from this, the triplet amplitudes in S are smaller than in the case above with thicker S and thinner F_1, although their range is not dissimilar. This is mainly because the triplet penetration into S is appreciably affected by finite size effects: when one of the F

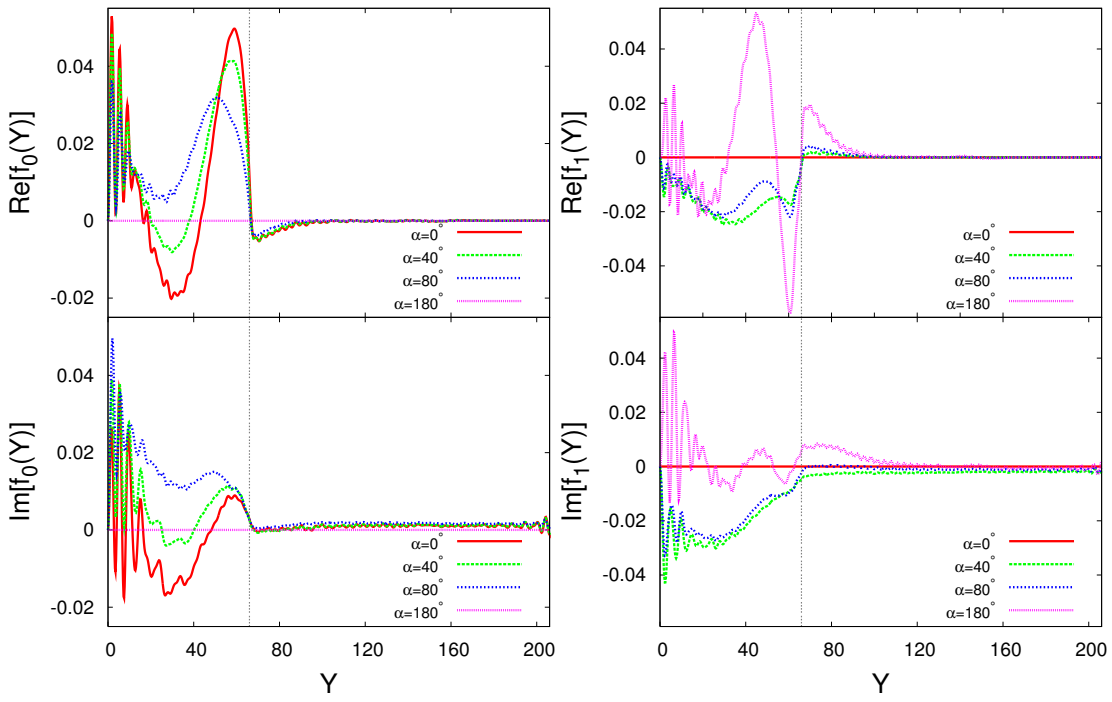

Figure 2.5: The real and imaginary parts of the triplet amplitudes, plotted as in the previous figure, except that the sample has $D_{F1} = 60, D_{F2} = 6$, and $D_S = 150$. See text for discussion.

layers is relatively thick, it is only after a longer time delay τ that the triplet correlations evolve. From Fig. 2.5, one can also see that the triplet f_0 correlations in S are nearly real (i.e. in phase with the singlet) and essentially independent of the angle α.

The triplet penetration is a function of the characteristic time τ scales. We therefore study the dependence of the triplet amplitudes on τ in Fig. 2.6, which shows results corresponding to $D_F = 10$, $D_S = 150$, $\alpha = 40°$, $I = 0.1$, and at four different values of τ. Again, the triplet amplitudes, particularly their imaginary parts, are long ranged. The plots clearly show that at short times, $\tau = 0.8$, the triplet correlations generated at the interface reside mainly in the F region. At larger values of τ, the triplet amplitudes penetrate more deeply into the S side, and eventually saturate. For the range of times shown, the magnitude of the real parts of f_0 and f_1 decays in the S region near the interface due to the phase decoherence associated with conventional proximity effects.

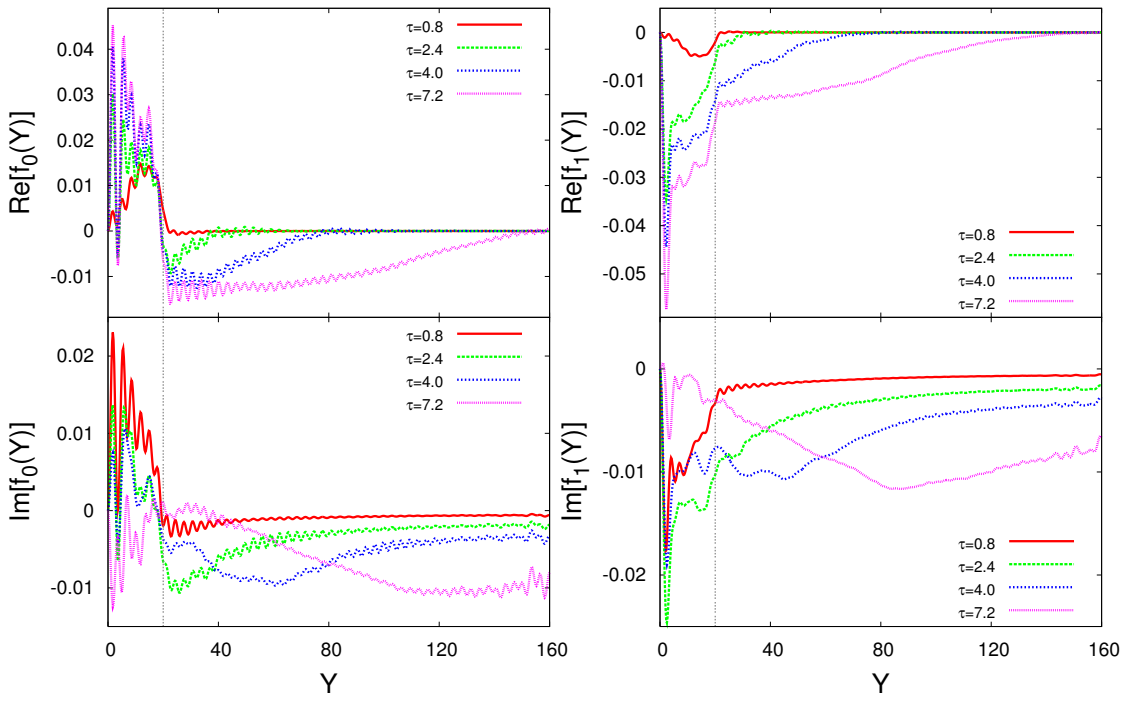

Figure 2.6: The real and imaginary parts of the triplet amplitudes plotted vs Y for the same parameter values and conventions as in Fig. 2.3, at fixed $\alpha = 40°$ for several values of τ as indicated.

For the largest value of $\tau = 7.2$ in the figure, the imaginary parts of f_0 and f_1 do not display monotonic decrease on the S side of the interface, but saturate instead. This is because for these values of τ the triplet amplitudes have already pervade the entire S.

We also investigated the dependence of the triplet amplitudes on the magnitude of the exchange field at a set time, $\tau = 4$. Fig. 2.7 illustrates the real and imaginary parts of the complex f_0 (left panels) and f_1 (right panels). The geometric parameters are $D_F = 10$ and $D_S = 150$, and we consider four different I values at fixed relative orientation, $\alpha = 40°$. In our discussion below, we divide these four different values into two groups, the first group includes the two smaller values, $I = 0.02$ and $I = 0.04$, and the second group includes the two somewhat larger ones, $I = 0.08$ and $I = 0.1$. In each group, the triplet amplitudes are similar in shape but different in magnitude. For the first group, there are no nodes at the F_2S interface for the f_0 components, while

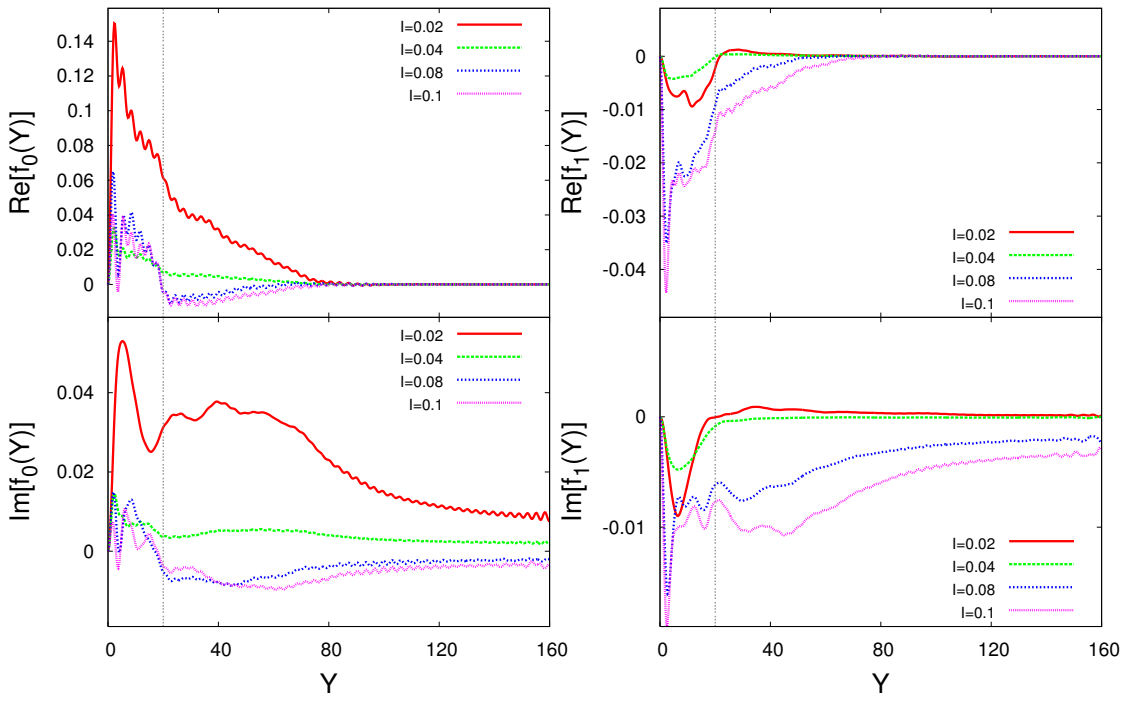

Figure 2.7: The triplet amplitudes f_0 and f_1 plotted as a function of position at fixed $\alpha = 40°$ and $\tau = 4$ for several values of I. We have here $D_F = 10$, and $D_S = 150$.

the f_1 components cross zero near it. For the second group, the opposite occurs: the f_0 components cross zero while the f_1 components do not. Also, the ratio of Re[f_0] at $I = 0.04$ to Re[f_0] at $I = 0.02$ is comparable to the ratio for the corresponding singlet amplitudes. This can be inferred, see Fig. 2.2, from the transition temperatures at $I = 0.02$, which are higher than at $I = 0.04$. Furthermore, the transition temperatures for the first group are monotonically increasing with α, while for the second group, they are non-monotonic functions with a minimum at around $\alpha = 80°$. Therefore, the f_0 triplet amplitudes are indeed correlated with singlet amplitudes and the transition temperatures also reflect their behaviors indirectly.

There is an interesting relationship involving the interplay between singlet and equal-spin triplet amplitudes: when T_c is a non-monotonic function of α, the singlet amplitudes, which are directly correlated with T_c, at the angle where $T_c(\alpha)$ has a minimum

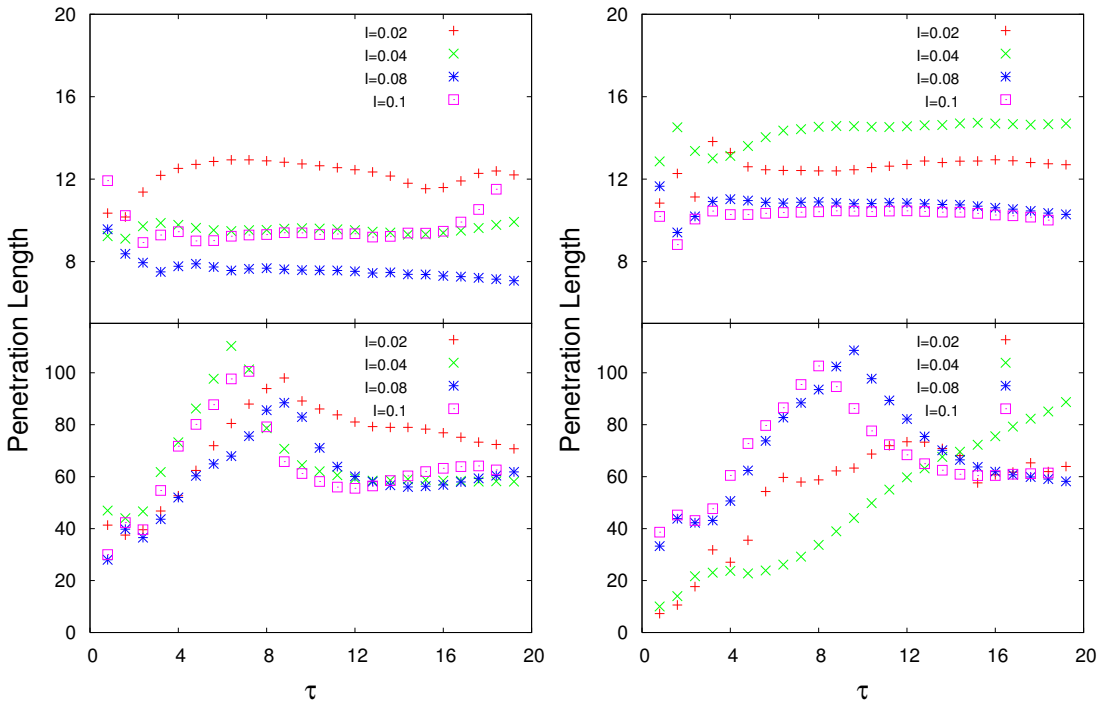

Figure 2.8: Study of the triplet penetration lengths, see Eq. 2.9, vs τ. In this figure, $D_F = 10$, $D_S = 150$, and $\alpha = 40°$. Left panels: lengths as extracted from $f_0(Y)$ for several values of I in the F regions (top panel) and in the S region (bottom panel). The right panels contain the same information, arranged in the same way, but with the penetration length extracted from $f_1(Y)$. The lengths eventually saturate.

are partly transformed into equal-spin triplet amplitudes. By looking at the central panel of Fig. 2.2, one sees that the transition temperatures for $I = 0.08$ and $I = 0.1$ nearly overlap, while the $I = 0.02$ case has a much higher transition temperature around $\alpha = 80°$. The singlet pair amplitudes, at zero temperature, follow the same trend as well: at $I = 0.02$, $F(Y)$ is much larger than the other pair amplitudes at different I values (see the middle panel of Fig. 2.3). The f_1 component for these cases, however, shows the opposite trend (see, e.g., the right panels of Fig. 2.7): for $I = 0.08$ and $I = 0.1$, the equal-spin correlations extend throughout the S region, but then abruptly plummet for $I = 0.02$. This inverse relationship between ordinary singlet correlations and f_1 is suggestive of a singlet-triplet conversion for these particular magnetization in

each ferromagnet layer.

Having seen that the triplet amplitudes generated by the inhomogeneous magnetization can extend throughout the sample in a way that depends on τ, we now proceed to characterize their extension by determining a characteristic triplet proximity length. We calculate the characteristic lengths, l_i, from our data for the triplet amplitudes, by using the same definition as in Ref. [34]:

$$l_i = \frac{\int dy |f_i(y,\tau)|}{\max |f_i(y,\tau)|}, \quad i = 0, 1, \tag{2.9}$$

where the integration is either over the superconducting or the magnetic region. The normalization means that these lengths measure the range, not the magnitude, of the induced correlations. In Fig. 2.8 we present results for the four lengths thus obtained, for a sample with $D_F = 10$, $D_S = 150$, and $\alpha = 40°$, at several values of I. The left panels show these lengths for the f_0 component, and the right panels show the results for the corresponding f_1 component. The triplet penetration lengths in the F region are completely saturated, even at smaller values of τ, for both f_0 and f_1. This saturation follows only in part from the relatively thin F layers used for the calculations in this figure: the same saturation occurs for the geometry of Fig. 2.5 where $D_{F1} + D_{F2} = 66$, although of course at much larger values of l_i. The triplet correlations easily pervade the magnetic part of the sample. On the other hand, the corresponding penetration lengths for both triplet correlations f_0 and f_1 in the S region are substantially greater and, because D_S is much larger, do not saturate but possess a peak at around $\tau = 8$ in all cases except for f_1 at $I = 0.04$ where it is beyond the figure range. The behavior for the sample with larger F thicknesses is, on the S side, qualitatively similar.

2.3.4 Thermodynamics

Given the self-consistent solutions, we are also able to compute the thermodynamic functions. In particular, we obtained the condensation free energies $\Delta F = F_S - F_N$ by using Eq. 2.7. In Fig. 2.9, we plot calculated results for ΔF at zero T, equivalent to the condensation energy. We normalize ΔF to $N(0)\Delta_0^2$, where $N(0)$ denotes the density of states at the Fermi level and Δ_0 denotes the bulk value of the singlet pair potential in S (see Sec. 1.1): thus we would have $\Delta F = -0.5$ for pure bulk S. The three panels in this figure correspond to those in Fig. 2.2. The geometry is the same and the symbol

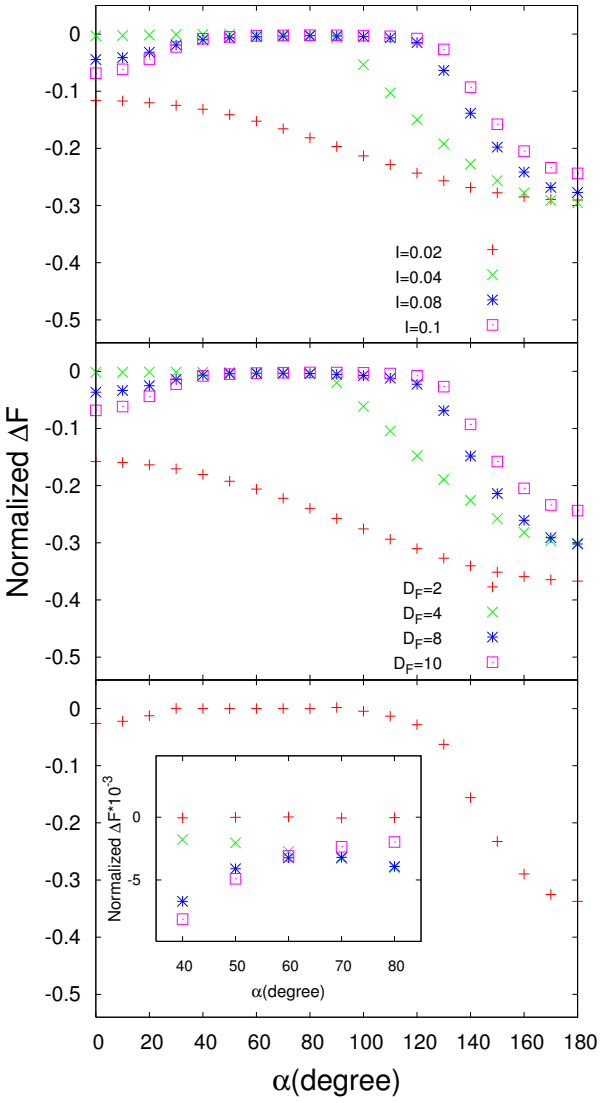

Figure 2.9: Normalized condensation free energies ΔF vs α, at $T = 0$. The three panels are for the same geometry and parameter values as in Fig. 2.2, and the symbols have the same meaning. Thus, the top panel corresponds to $D_F = 10$ and several values of I, while the middle panel is for $I = 0.1$ and several values of D_F. The bottom panel corresponds to the reentrant case shown in the corresponding panel of Fig. 2.2. The inset shows the difference between truly reentrant cases and those for which the condensation energy is small (see text) in the range of $\alpha = 40°$ to $\alpha = 80°$.

meanings in each panel correspond to the same cases, for ease of comparison. In the top panel, we see that the ΔF curves for $I = 0.02$ and $I = 0.04$ are monotonically decreasing with α. This corresponds to the monotonically increasing T_c. One can conclude that the system becomes more superconducting when α is changing from parallel to antiparallel: the superconducting state is getting increasingly more favorable than the normal one as one increases the tilt from $\alpha = 0°$ to $\alpha = 180°$. The other two curves in this panel, which correspond to $I = 0.08$ and $I = 0.1$, show a maximum near $\alpha = 80°$. Again, this is consistent with the transition temperatures shown in Fig. 2.2. Comparing also with the middle panel of Fig. 2.3, we see that the singlet amplitude for $I = 0.02$ is much larger than that for the other values of I. This is consistent with Fig. 2.9: ΔF is more negative at $I = 0.02$ and the superconducting state is also more stable. The middle panel of Fig. 2.9 shows ΔF for different ferromagnet thicknesses. The curves are very similar to those in the top panel, just as the top two panels in Fig. 2.2 were found to be similar to each other. Therefore, both Fig. 2.2 and Fig. 2.9 show that the superconducting states are thermodynamically more stable at $\alpha = 180°$ than in the intermediate regions ($\alpha = 40°$ to $\alpha = 80°$). From the top two panels in Fig. 2.9, we also see that ΔF at $\alpha = 180°$ can be near -0.3 in this geometry; this is a very large value, quite comparable to that in pure bulk S. However, in the region of the T_c minima near $\alpha = 80°$, the absolute value of the condensation energy can be over an order of magnitude smaller, although it remains negative (see below). The bottom panel of Fig. 2.9 shows ΔF for the reentrant case previously presented in Fig. 2.2, for which $D_F = 6$ and $I = 0.15$. The main plot shows the condensation energy results, which vanish at intermediate angles. Because ΔF in the intermediate non-reentrant regions shown in the upper two panels can be very small, in the vertical scale shown, we have added to the lowest panel an inset where the two situations are contrasted. In the inset, the (red) plus signs represent ΔF for the truly reentrant case and the other three symbols have the same meaning as in the middle panel, where no reentrance occurs. The inset clearly shows this difference: ΔF vanishes in the intermediate region only for the reentrant T_c case, but remains slightly negative otherwise. The pair amplitudes for the reentrant region are found self-consistently to be identically zero. Thus, one can safely say that in the intermediate region the system must stay in the normal state and other self-consistent superconducting solutions do not exist. Evidence for reentrance with α

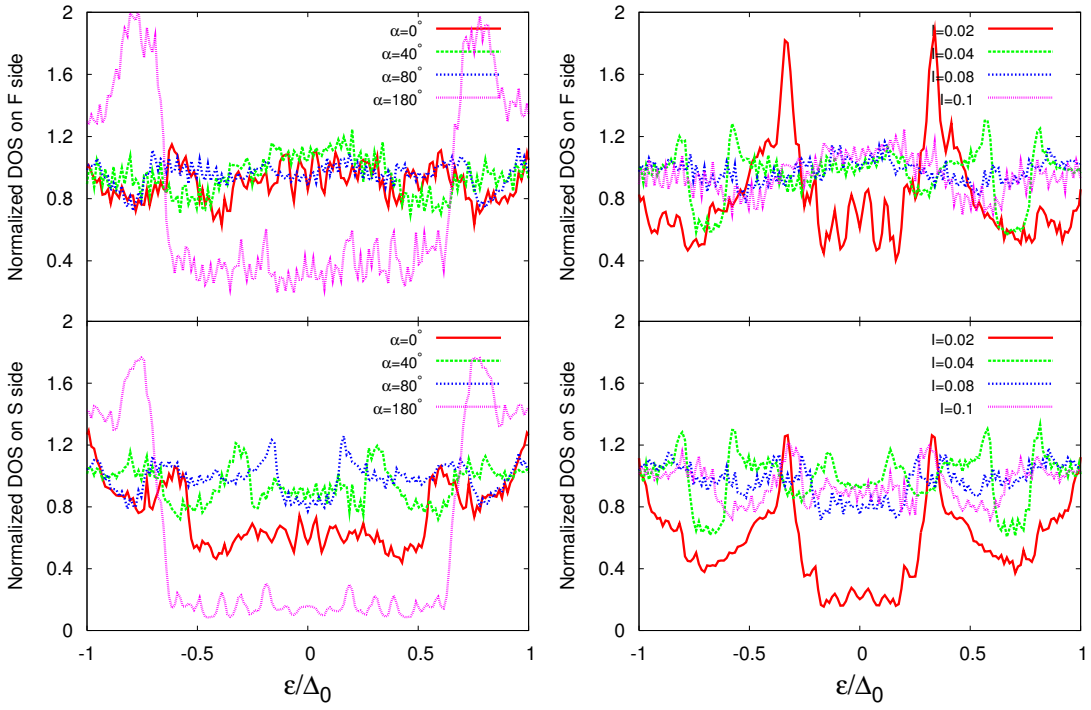

Figure 2.10: LDOS integrated over the F layers (top panels) and the S layer (bottom panels). In all cases $D_F = 10$, $D_S = 150$, and $T = 0.05T_c^0$. The left panels show results for $I = 0.1$ and the indicated values of α, while in the right panels we have $\alpha = 40°$ and several values of I.

in F_1F_2S is therefore found from both the microscopic pair amplitude and also from T_c: it is also confirmed thermodynamically. That superconductivity in F_1F_2S trilayers can be reentrant with the angle between F_1 and F_2 layers makes these systems ideal candidates for spin valves.

2.3.5 DOS

Next, we present our results for the local DOS (LDOS) in F_1F_2S systems. All plots are normalized to the corresponding value in a bulk sample of S material in its normal state. The top panels in Fig. 2.10 show the normalized LDOS integrated over the entire magnetic portion of the sample, while in the bottom panels the LDOS is integrated over

the S region. In all four cases, we set $D_F = 10$ and $D_S = 150$. In the left panels, we have fixed $I = 0.1$, and present results for several angles, whereas in the right panels, we take a fixed $\alpha = 40^\circ$ and show results for several values of I as indicated. In the top left panel (F side), we see no energy gap for any value of α, however, a flat valley between the two peaks when $\alpha = 180^\circ$ resembles a characteristic feature of the DOS in bulk superconductors. However, the plots at the other three angles, where the transition temperature and condensation energies are much lower, are very near the value of the DOS in its normal state throughout all energies. This is also consistent with the top panel of Fig. 2.3, where the Cooper pair amplitudes in this case are larger inside F most significantly at $\alpha = 180^\circ$. The singlet amplitudes at $\alpha = 0^\circ$ are also larger than in the other noncollinear configurations, but its superconducting feature in the LDOS is not as prominent. This could be due to the contributions from the triplet pairing correlations: we know from the spin symmetry arguments discussed above that the f_1 component of the induced triplet amplitude does not exist at $\alpha = 0^\circ$, and therefore it cannot enhance the superconducting feature in the DOS. On the contrary, both singlet and triplet amplitudes can contribute when $\alpha = 180^\circ$. Thus, the LDOS results in the F side reflect the signature of induced triplet amplitudes in F_1F_2S systems.

The left bottom panel displays the integrated LDOS over the entire S layers for the same parameters as the top one. Again, the plot for $\alpha = 180^\circ$, corresponding to the highest T_c and the most negative condensation energy, possesses a behavior similar to that of pure bulk S material, although the wide dip in the DOS does not quite reach down to zero. On the other hand, the LDOS at $\alpha = 80^\circ$, the case with the most fragile superconductivity, has a shallow and narrow valley. The DOS plots on the left side are very similar to the normal state result both at $\alpha = 40^\circ$ and at $\alpha = 80^\circ$. In summary, the depth and the width of the dip are mostly correlated with the singlet pair amplitudes. The left panels also support our previous analysis: the slight difference between the normal states and superconducting states in the intermediate angle region is reflected in the DOS. The right panels reveal how the magnetic strength parameter, I, affects the integrated DOS. As we can see from the middle panel in Fig. 2.3, the singlet Cooper pair amplitudes for this case drop significantly when $I \geq 0.04$. The right panels in Fig. 2.10 confirm this information, that is, the integrated DOSs in both the F and S sides have a very noticeable dip in the F side, and a near gap on the S region for $I = 0.02$, while

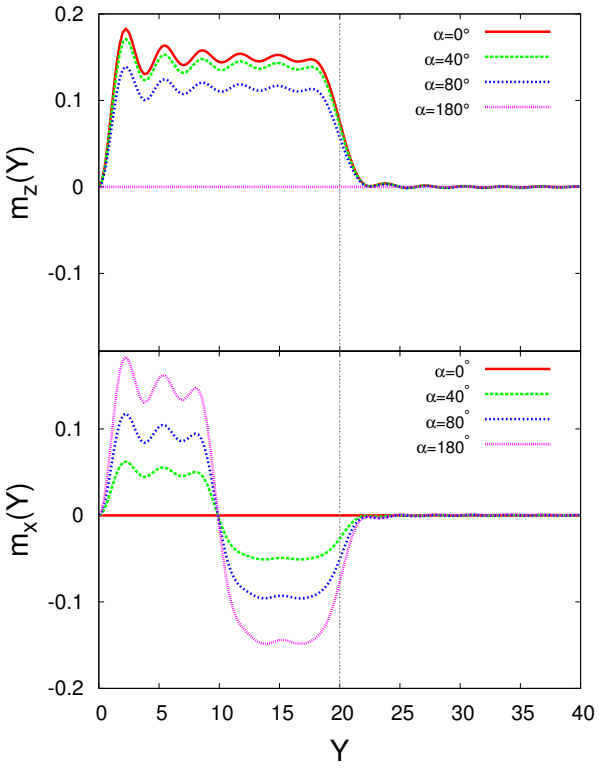

Figure 2.11: The z component (top panel) and the x component (bottom panel) of the local magnetization, plotted as a function of Y for several α values. We use $D_F = 10$, $D_S = 150$, and $I = 0.1$ in this figure.

for the other values of I the evidence for superconductivity in the DOS is much less prominent.

2.3.6 Local magnetization

Finally, it is also important to study the reverse proximity effects: not only can superconductivity penetrate into the ferromagnets, but conversely the electrons in S near the interface can be spin polarized by the presence of the F layers. This introduction of magnetic order in S is accompanied by a corresponding decrease of the local magnetization in F_2 near the S interface. In Fig. 2.11, we show the components of the local magnetization, as defined in Eqs. 2.4. The parameters used are $D_F = 10$, $D_S = 150$,

and $I = 0.1$ and results are shown for different values of α. The local magnetization results shown are normalized by $-\mu_B(N_\uparrow + N_\downarrow)$, where $N_\uparrow = k_F^3(1+I)^{3/2}/6\pi^2$ and $N_\downarrow = k_F^3(1-I)^{3/2}/6\pi^2$. From the figure, one sees at once that both the sign and average magnitude of the m_x and m_z components inside the F material are in accordance with the values of the angle α and of the exchange field ($I = 0.1$). As to the reverse proximity effect, we indeed see a nonzero value of the local magnetization in S near the the interface. The penetration depth corresponding to this reverse effect is independent of α. Unlike the singlet and triplet amplitudes, which may spread throughout the entire structure, the local magnetization can only penetrate a short distance. This is consistent with results from past work [33].

2.4 Summary and conclusions

In summary, we have investigated in this chapter the proximity effects in F_1F_2S trilayers by self-consistently solving the BdG equations. One of the most prominent features of these systems, which make them different from F_1SF_2 structures is the non-monotonicity of $T_c(\alpha)$, as the angle α between adjacent magnetizations is varied. For F_1SF_2 systems, the critical temperature is always lowest for parallel ($\alpha = 0^\circ$) orientations, chiefly due to the decreased average exchange field as α increases and the two F's increasingly counteract one another. In contrast, we find that the F_1F_2S configurations can exhibit, for particular combinations of exchange field strengths and layer thicknesses, critical temperatures that are lowest for relative magnetization orientations at an intermediate angle between the parallel and antiparallel configurations. In some cases the drop in T_c from the parallel state, as α is varied, is large enough that superconductivity is completely inhibited over a range of α, and then reemerges again as α increases: the system exhibits reentrant superconductivity with α. We have also calculated the singlet pair amplitude and condensation energies at zero temperature, revealing a behavior that is entirely consistent with these findings.

We have studied the odd triplet amplitudes that we find are generated, and found that both the opposite spin pairing (with $m = 0$) amplitude, f_0, and the equal-spin pairing amplitude (with $m = \pm 1$), f_1, can be induced by the inhomogeneous exchange fields in the F layers. Also of importance, we have shown that the triplet pairing

correlations can be very long ranged and extend throughout both the F and S regions, particularly for relatively thick S and F layers. We have characterized this penetration by calculating and analyzing properly defined characteristic lengths. We have also shown that the inner F_2 layer, when its exchange field is not aligned with that of the outer F_1 layer, plays an important role in generating the triplet amplitudes. When both magnets are thin, there is an indirect relationship between the singlet pairing amplitudes that govern T_c and the f_1 amplitudes that govern the behavior of equal-spin pairing. We have also presented calculations of the energy resolved DOS, spatially averaged over the S or F regions, demonstrating clear signatures in the energy spectra, which can be identified depending on the relative magnetization vectors in the F_1 and F_2 regions. We have determined that the extent of magnetic leakage into the S region as extracted from a calculation of the components of the local magnetization, is rather short ranged. Throughout this chapter, we have emphasized the potential of these structures as ideal candidates for spin valves.

Chapter 3

Comparison of theory with experiment: superconductor/spin-valve heterostructures

In this chapter, we compare the theory of proximity effects in superconductor/spin-valve heterostructures as discussed in Chap. 2 with experiments from our collaborators, A. Jara *et al* [53]. In Chap. 2, we demonstrated important physical properties of F_1F_2S trilayers, including the non-monotonic behavior of $T_c(\alpha)$ as well as the emergence of both $m = 0$ and $m = \pm 1$ triplet components when magnetizations are noncollinear. In addition, we predicted the existence of the singlet-to-triplet conversion in these trilayers.

Thin-film multilayers of S and F materials are a convenient platform for experimental studies of the proximity-induced triplet condensate [41, 63, 81, 82, 83, 84, 85, 86, 87]. The advantages of the F/S thin-film multilayers include: (i) well-established methods of the multilayer deposition, (ii) easy and controllable manipulation of the magnetic state of the F layers via application of an external magnetic field, and (iii) suitable for our theoretical description of the condensate owing to the translational symmetry in the multilayer plane. Here, we compare our theoretical fit with experimental studies on the dependence of T_c in CoO(2 nm)/Co/Cu/Co/Nb(17 nm) multilayers on the in-plane

angle α between the magnetic moments of the Co layers (see Fig. 3.1) The 2 nm thick CoO film is antiferromagnetic at cryogenic temperatures and its purpose is to pin the direction of the top Co layer via the exchange bias phenomenon [88]. The sole purpose of introducing the nonmagnetic Cu spacer layer is to decouple the magnetic moments of the Co layers and it is chosen to be thick enough ($d_n < 4$ nm) so that both the direct and the RKKY [89] exchange interactions between the Co layer are negligibly small. Furthermore, as we will demonstrate below, the F/S multilayer thin films we consider here exhibit exactly the same characteristics to those that have already been discussed in Chap. 2 for F_1F_2S trilayers. Three series of multilayers, each series with varying thickness of one of the layers (free magnetic layer d_f, pinned magnetic layer d_p, and nonmagnetic layer d_n), were deposited. The three multilayer series reported in this chapter were designed to elucidate the dependence of the triplet condensate pair amplitude on the spin-valve parameters. The description of the series geometries is as follow:

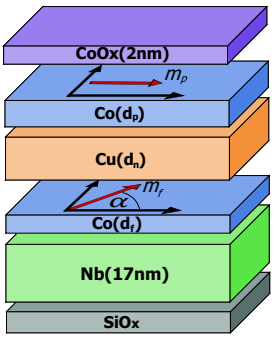

Figure 3.1: Schematic of the CoO(2 nm)/ Co(d_p)/ Cu(d_n)/ Co(d_f)/ Nb(17 nm) multilayer, where α is the in-plane angle between the magnetic moments of the Co layers. (Courtesy of A. A. Jara.)

Series 1: CoO(2 nm)/ Co(2.5 nm)/ Cu(6 nm)/ Co(d_f)/ Nb(17 nm) with d_f ranging from 0.5 nm to 1.0 nm

Series 2: CoO(2 nm)/ Co(2.5 nm)/ Cu(d_n)/ Co(0.6 nm)/ Nb(17 nm) with d_n ranging from 4 nm to 6.8 nm

Series 3: CoO(2 nm)/ Co(d_p)/ Cu(6 nm)/ Co(0.6 nm)/ Nb(17 nm) with d_p ranging from 1.5 nm to 5.5 nm.

3.1 Theoretical methods

The theoretical method we adopted here has previously been thoroughly discussed in Sec. 2.2 and Refs. [34, 58, 79]: therefore, we only present here the essential components necessary for our discussion. We modeled the Co/Cu/Co/Nb heterostructures as $F_p/N/F_f/S$ layered systems, where F_p and F_f are the outer (pinned) and inner (free) magnets. They play the same roles as F_1 and F2 layers in Chap. 2. N denotes the normal metallic intermediate layer. As stated in Chap. 2 and beginning of this chapter, the layers are assumed to be infinite in the x-z plane with a total thickness d in the y direction, which is perpendicular to the interfaces between layers. In accordance with the experiment, F_p has width d_p, and a fixed direction of magnetization. The normal layer with width d_n is sandwiched between this pinned layer and a magnetic layer F_f of width d_f, with an experimentally controlled magnetization direction. The superconducting layer of thickness d_S is in contact with the free layer. To accurately describe the physical properties of our systems with sizes in the nanometer scale and moderate exchange fields, we again numerically solve the microscopic BdG equations in a fully self-consistent manner. The quasi-one-dimensional BdG equations, Eq. 2.1, introduced in Sec. 2.2 are appropriate and adopted in this chapter. To model the scattering that usually occurs at interfaces, the single-particle Hamiltonian, $\mathcal{H}_0 = -1/(2m)d^2/dy^2 - E_F + U(y)$, now contains an effective interfacial scattering potential described by delta functions of strength H_j (j denotes the different interfaces), namely:

$$\begin{aligned} U(y) =& H_1\delta(y - d_p - d_n - d_f) + H_2\delta(y - d_p - d_n) \\ &+ H_3\delta(y - d_p), \end{aligned} \tag{3.1}$$

where $H_j = k_F H_{Bj}/m$ is written in terms of the dimensionless scattering strength H_{Bj}. As noted in Chap. 2, the exchange fields are assumed to have the form $h_x(y) = h\sin(-\alpha/2)$ and $h_z(y) = h\cos(-\alpha/2)$ in F_f, where h is the magnitude of exchange field. In F_p, we have $h_x(y) = h\sin(\alpha/2)$ and $h_z(y) = h\cos(\alpha/2)$. We have assumed that the quantization axis lies along the z direction, but one can easily obtain the spin dependent

quasiparticle amplitudes with respect to a different spin quantization axis rotated by an angle θ in the x-z plane via the rotation matrix, Eq. 2.8 [34].

To determine T_c, we adopt the linearization method described in Sec. 2.2. More details of this efficient technique are discussed in Ref. [44, 79]. To analyze the correlation between the behavior of the superconducting transition temperatures and the existence of the odd triplet superconducting correlations in our systems, we compute the induced triplet pairing amplitudes according to Eqs. 2.3 [33, 34]. As discussed in Chap.1 and 2, these triplet pair amplitudes are odd in time t and vanish at $t = 0$, in accordance with the Pauli exclusion principle.

3.2 Analysis

In this subsection, we present our theoretical analysis and compare the theoretical results with the experimental data. The fitting process is rather time-consuming since for every parameter set, one must evaluate T_c numerically as a function of the misalignment angle α, making a least squares fit unfeasible. The same situation occurs in Refs. [44, 56]. As in those works, we search within plausible regions of the parameter space, and display here results of the best fit that we have found, which is not necessarily the best possible fit. There are a number of parameters at one's disposal and, when computing the theoretical values of T_c, we first have to keep the number of fitting parameters as small as possible. All of the relevant physical parameters that are related to the properties of the materials involved, such as the exchange field, and the effective superconducting coherence length, are required to be the same for all of the different samples when performing the fitting. However, for parameters that are affected by the fabrication processes, such as the interfacial barrier strength, one can reasonably assume, as we do, that their values somewhat vary from sample to sample. We do find that the variation is small between different samples in each series. For the material parameters, we have found that the best value of the effective Fermi wavevector is $k_F = 1\mathring{A}^{-1}$ and the effective superconducting coherence length $\xi_0 = 11.5\,\mathrm{nm}$. For the dimensionless exchange field $I \equiv h/E_F$, we have used, for Co, $I = 0.145$ which is consistent with previous [34] work. The superconducting transition temperature for a putative pure superconducting sample with the same quality as the material in the layers, we have

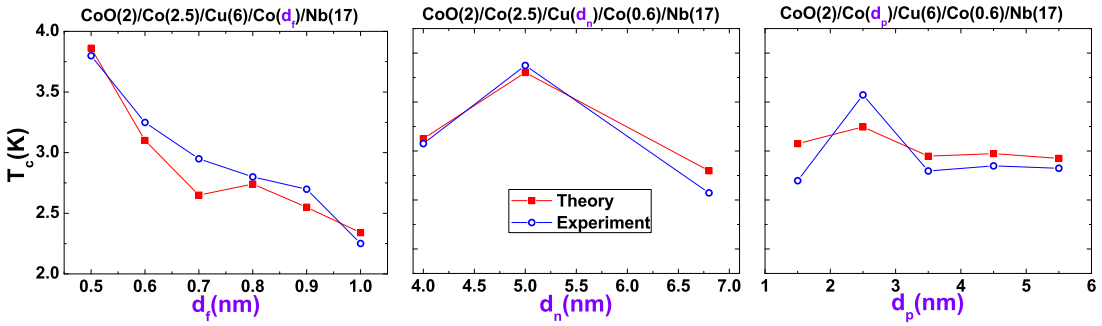

Figure 3.2: Experimental data and theoretical fitting of T_c in the P state as a function of: (left panel) the Co free layer thickness d_f (with $d_n = 6\,\text{nm}$ and $d_p = 2.5\,\text{nm}$), (center panel) the Cu normal metal layer thickness d_n (with $d_p = 2.5\,\text{nm}$ and $d_f = 0.6\,\text{nm}$), and (right panel) the Co pinned layer thickness d_p (with $d_n = 6\,\text{nm}$ and $d_f = 0.6\,\text{nm}$).

used $T_c^0 = 4.5$ K. This is the same value as previously found [44]. It is of course lower than that of the true bulk transition temperature of Nb. All of these parameters are kept invariant across all of the different samples, as mentioned earlier. Only the three interfacial barrier strengths are treated as adjustable from sample to sample during the fitting process. We assume, however, that the barrier strength is the same on both sides of the normal metal layer while that between the free ferromagnetic layer and the superconductor are weaker. For each series, the barrier varies somewhat from batch to batch. They are found to be as follows: $H_{B1} = 0.2$ and both H_{B2} and H_{B3} vary from 0.64 to 0.7 for different batches in the d_f series. For the d_p series, we have $H_{B1} = 0.15$, $0.53 < H_{B2}$ and $H_{B3} < 0.58$. The d_n series have H_{B1} ranges from 0.3 to 0.45 and $H_{B1} = H_{B2} = 0.62$. The thicknesses of the different layers are taken of course from their experimental values. As in Ref. [56], we find a thin magnetic "dead layer" between the normal metal and the free ferromagnetic layer of a small thickness in the range from $0.27\,\text{nm} \sim 0.35\,\text{nm}$.

We now compare the experimental and theoretical values of T_c as a function of layer thicknesses and angle α for three different batches of samples: in the first, we vary d_f, in the second, d_n, and in the last, d_p. First, in Fig. 3.2, we present comparisons between experiment and theory, for the T_c results in the parallel state ($\alpha = 0°$) as a function of thickness for the three different series mentioned above. In all three series, the experimental and theoretical T_c are in very good agreement with each other. For the

d_f series, one should notice that both experimental and theoretical T_c are very sensitive to the thicknesses of the free layers. When the thickness of the free ferromagnetic layer is increased, T_c decreases non-monotonically by almost 50%. However, the d_n and d_p series do not show the same sensitivity, even though the ranges of thicknesses for these two series are much larger compared to that of the d_f series. This lower sensitivity is physically reasonable for the following reason: because of the presence of ferromagnets, we find that the magnitude of the singlet pairing amplitude decreases rapidly beyond the boundary, in non-S regions away from the F/S interface. The exchange field reduces the proximity effect. Thus, the size effects from the thicknesses of normal metal layers and fixed ferromagnetic layers are less. We also observe the trend that both theoretical and experimental T_c are often found to be a non-monotonic function of the thicknesses of the F layers. In fact, except for the experimental T_c for d_f series, which does not show a clear oscillatory behavior, all other series clearly exhibit the non-monotonicity of T_c. The oscillatory behavior of transition temperatures as one varies the thickness is standard in hybrid F/S heterostructures due to the oscillatory character of the pair amplitude itself (see Chaps. 1 and 2 and Ref. [15]). The reason for the exception found might be that the data points are too widely spaced. This non-monotonic behavior has been noted in past works [19, 22] and is often found [52] in F_1F_2S trilayers.

In Fig. 3.3, we present a detailed comparison of theoretical and experimental results for ΔT_c as a function of angle α between the magnetizations in the free and fixed layers for the d_f, d_n, and d_p series. Each panel in the first row in Fig. 3.3 represents different samples for d_f series. Results for the d_n and d_p series are plotted in the second and third row, respectively. One can clearly see that the behavior of the highly non-monotonic angular dependencies of the theoretical results presented here describe very well the experimental results, not only qualitatively but also quantitatively: the magnitudes of the experimental and theoretical results for ΔT_c are comparable: both the experimental and theoretical results indicate that the switching effects are in about 25 mK range. It is well worth recalling that in other recent work [44] the results for the magnitude of this quantity differed by more than one order of magnitude. In contrast, here, taking into account the existence of numerical and experimental uncertainties (the former we estimate at ~ 1.5 mK), we find theory and experiment are in very good agreement. This great improvement over Ref. [44] follows from the more careful treatment of the interface

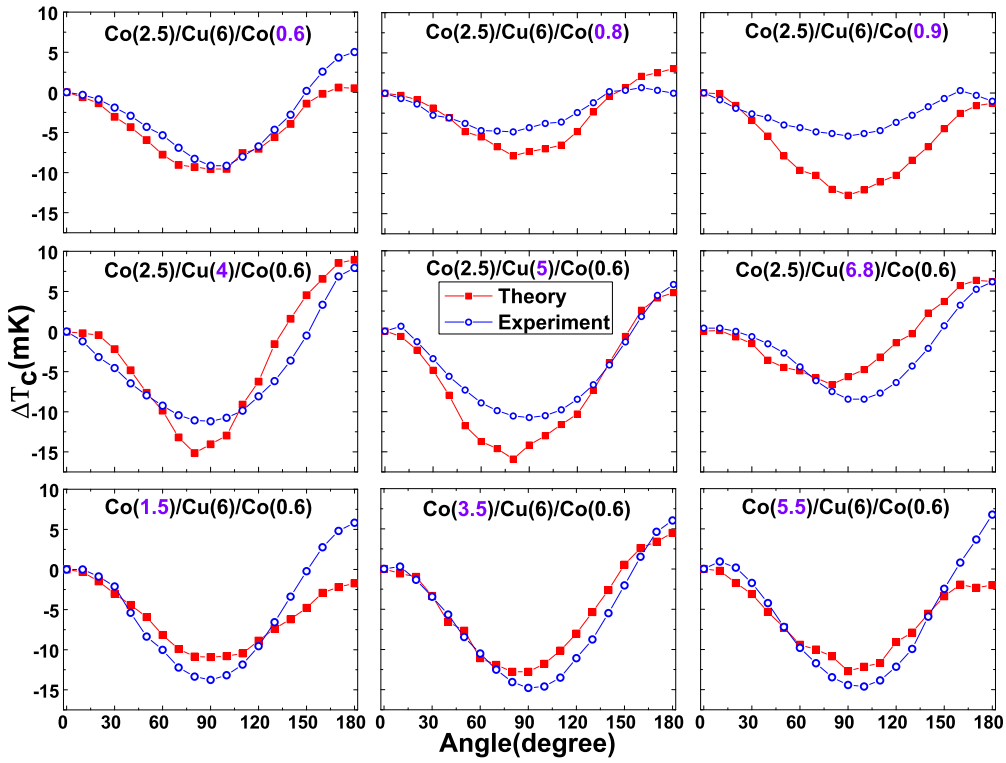

Figure 3.3: Experiment and theory comparisons of ΔT_c [defined as $\Delta T_c(\alpha) \equiv T_c(\alpha) - T_c(0)$] as a function of relative magnetization angle are shown for the three batches of samples: (Top row) three different free layer thicknesses, $d_f = 0.6\,\text{nm}$, $0.8\,\text{nm}$, $0.9\,\text{nm}$, and with $d_p = 2.5\,\text{nm}$, $d_n = 6\,\text{nm}$. (Middle row) three different nonmagnetic layer thicknesses: $d_n = 4\,\text{nm}$, $5\,\text{nm}$, $6.8\,\text{nm}$, and with $d_f = 0.6\,\text{nm}$, $d_p = 2.5\,\text{nm}$. (Bottom row) three different pinned layer thicknesses: $d_p = 1.5\,\text{nm}$, $3.5\,\text{nm}$, $5.5\,\text{nm}$, and with $d_f = 0.6\,\text{nm}$, $d_n = 6\,\text{nm}$.

barriers from sample to sample and a much more extensive search in the parameter space. For the d_f series, we see that the switching range for both the experimental and theoretical $T_c(\alpha)$ varies non-monotonically when d_f is increased. This occurs for the same reason already mentioned in the discussion of Fig. 3.3: the behavior of $T_c(\alpha)$ is very sensitive to the inner ferromagnetic layer thicknesses due to the proximity effects. Similarly, we observe that the switching ranges are less sensitive to the thickness of the outer ferromagnetic layer (see that in d_p series) and also to the normal metal layer thickness in d_n series.

We now turn to the role that induced triplet correlations in the non-monotonic behavior of $T_c(\alpha)$. This has been the subject of recent theoretical interest [51, 52, 67] but little has been done on quantitatively comparing theory and experiment. To examine this question in a quantitative way, we have computed the induced odd triplet pairing correlations. These correlations, as well of course as the ordinary singlet correlations, can be self-consistently calculated using the methods previously described. As noted in Chaps. 2 and 3, with the presence of non-homogeneous magnetizations, the triplet pair amplitudes can generally be induced when $t \neq 0$. We present our study in terms of the quantity

$$F_t(y,t) \equiv \sqrt{|f_0(y,t)|^2 + |f_1(y,t)|^2}, \tag{3.2}$$

where the quantities involved are defined in Eq. 2.3. This quantity accounts for both triplet components, the equal-spin and opposite spin triplet correlations. The reason to use this quantity is that via Eq. 2.8, one can easily show that, when the spin quantization axis is rotated by an angle θ, the rotated triplet pair amplitudes $\tilde{f}_0$ and $\tilde{f}_1$ after the transformation are related to the original f_0 and f_1 by:

$$\tilde{f}_0(y,t) = f_0(y,t)\cos\theta - f_1(y,t)\sin\theta, \tag{3.3a}$$

$$\tilde{f}_1(y,t) = f_0(y,t)\sin\theta + f_1(y,t)\cos\theta. \tag{3.3b}$$

Therefore, the quantity $F_t(y,t)$ that we focus on obviates any ambiguous issues related to the existence of generally noncollinear "natural" axes of quantization in the system.

We have computed this quantity as a function of position and α. It turns out to be particularly useful to focus on the average value of $F_t(y,t)$ in the pinned layer $\mathrm{F_p}$. We normalize this averaged quantity, computed in the low T limit, to the value of the singlet pair amplitude in the bulk S. This normalized averaged quantity is plotted, as a function

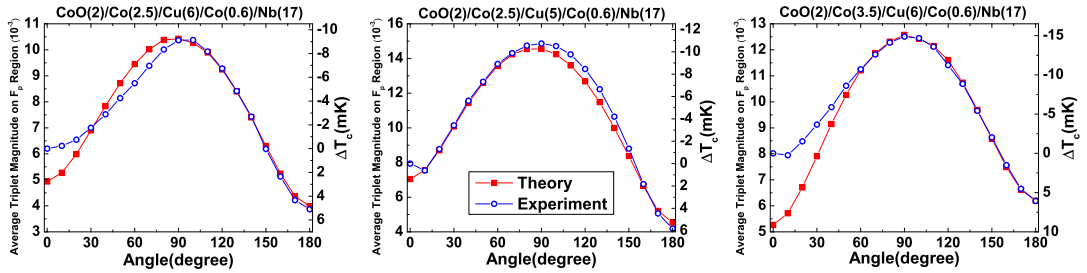

Figure 3.4: Average triplet amplitudes in the pinned ferromagnet layer as a function of relative magnetization angle. The quantity plotted is the average of $F_t(y,t)$ (Eq. 3.2) in this region, at $\omega_D t = 4$. The quantity ΔT_c is also shown (right scale). Red squares are the theoretical triplet amplitudes (left scale) and the blue circles are the experimental ΔT_c (right inverted scale) as a function of angle. The ΔT_c data corresponds to one set chosen from each batch of samples in Fig. 3.3. Left panel: from the d_f series, Middle panel: from the d_n series, Right panel: from the d_p series.

of α in Fig. 3.4 (left vertical scale) at a dimensionless characteristic time $\omega_D t = 4.0$. This time value is unimportant, provided it be nonzero, of course. In the three panels, an example taken from each of the series is displayed, as explained in the caption. One can observe that the maxima of this average F_t occur when $\alpha = \pi/2$ and its minima are either at $\alpha = 0$ or $\alpha = \pi$. In the same figure (right vertical scale), the experimental values of $\Delta T_c(\alpha)$, for the same cases which have minima near $\pi/2$, are plotted in an inverted scale. The agreement is truly striking. The anti-correlation can be easily understood: the magnitude of the low T singlet pair amplitudes is of course positively correlated to T_c. Here, the fact that the triplet pair amplitudes are anti-correlated to T_c (or to the singlet amplitudes) indicates a singlet-triplet conversion process (see also Subsec. 2.3.3): when more singlet superconductivity leaks into the ferromagnet side, T_c is suppressed and triplet superconductivity is enhanced. The average magnitude of the triplet pair amplitudes in the free and normal layer regions is only weakly dependent on α: of importance is the propagation of triplet pairs throughout the entire system, generated by the symmetry breaking interfaces and magnetic inhomogeneity created from the two misaligned ferromagnets. This clearly demonstrates a singlet to triplet process which is related to the non-monotonicity of the transition temperature.

In conclusion, the theoretical prediction we made in Chap. 2 on the non-monotonic

behavior of superconducting transition temperatures T_c, as a function of the misorientation angle between magnetic moments of F layers, was experimentally observed in CoO/Co/Cu/Co/Nb multilayer thin films. Our numerical self-consistent solutions of the BdG equations quantitatively and accurately describe this behavior. We also verified theoretically that this non-monotonic behavior is correlated to the penetration of the odd triplet superconductivity in Co/Cu/Co spin valves: the average triplet amplitudes in the pinned layer are maximized when $T_c(\alpha)$ is at its minimum. This anti-correlation is connected with the singlet-to-triplet conversion.

Chapter 4

Proximity effects in conical-ferromagnet/superconductor bilayers

4.1 Introduction

We begin this chapter by reviewing the fundamental physics of the F/S heterostructures. As discussed in Chap. 2, the oscillations of the superconducting wavefunctions in F/S systems are one of the most salient features governing proximity effects in F/S systems and form the basis for switching applications that require manipulation of the superconducting transition temperature T_c through the variation of experimental parameters. Due to the oscillatory nature of the Cooper pair amplitudes, the dependence of T_c on the thickness of the ferromagnetic layer, d_F, in F/S layered structures is oscillatory as well. Furthermore, due to the quantum interference effects, the superconductivity in F/S may disappear for a certain d_F range. This superconducting reentrant behavior with d_F has been found experimentally in Nb/$Cu_{1-x}Ni_x$ and Fe/V/Fe trilayers [23, 24, 25] and it is well understood theoretically [13, 19, 20, 21, 26, 27, 28].

Another important fact about F/S proximity effects is the generation of induced triplet pairing correlations. These can be generated by the presence of spin active interfaces [59, 60, 61, 90], or (and this is the case we will focus on in this chapter) in

systems with clean interfaces and inhomogeneous F structures [29, 30, 32, 33, 34]. The simplest such cases are F_1SF_2 or F_1F_2S layers (see Chap. 2) in which the magnetizations of the two F layers are misaligned. The importance of the odd triplet correlations lies in their long-range nature in the magnet, i.e., their proximity lengths can be, in principle, comparable to those found in the usual superconducting proximity effects involving nonmagnetic metals (see Sec. 1.2 and 2.1). Since the exchange fields tend to align the electronic spins of the Cooper pair electrons, the proximity length for singlet pairing is very short and dependent on the magnitude of exchange field. However, the triplet pairing correlations can involve electron pairs with both spins aligned along the local magnetization direction, and thus be much less sensitive to the mechanism of exchange fields, penetrating much deeper in F than their singlet counterparts. The possible appearance of both $m = 0$ and $m = \pm 1$ components of the induced triplet correlations is controlled by the symmetry of the system and by conservation laws (see Ref. [34] and Sec. 1.2). All three components ($m = 0$ and $m = \pm 1$) can arise if the direction of exchange fields differs in the ferromagnets, e.g. the exchange fields of F_1 and F_2 are not aligned in [34] F_1SF_2 or F_1F_2S types of trilayers (see Chap. 2). These long-range characteristics of triplet correlations have been experimentally detected in ferromagnetic multilayers by taking advantage of their magnetic inhomogeneity [37, 63, 64].

Besides the misalignment of ferromagnets, another possibility to generate long-range triplet correlations is to use a ferromagnet with an intrinsic inhomogeneous magnetic texture [91]. Such structures are inherent to either known elements or chemical compounds. Examples of this kind of ferromagnets include most prominently Ho [92], which has a conical magnetic structure at low temperatures. A similar conical magnetic structure is found in metallic Erbium [93], MnSi thin films [94], and Fe(Se,Te) compounds [95]. Indeed, it has been experimentally confirmed that the long-range triplet correlations are induced in Nb/Ho/Co multilayers [38] with the periodicity of Ho playing an important role in triplet supercurrents. Superconducting phase-periodic conductance oscillations have also been observed in Al/Ho bilayers [92] where the thickness of Ho is much larger than the penetration length of singlet amplitudes. This finding can be explained in the framework of the triplet proximity effects. Theoretically, the spin-polarized Josephson current in S/Ho/S junctions has been studied [96] via quasiclassical Green function techniques. The triplet supercurrent in Ho/Co/Ho trilayers was

also investigated in the diffusive [97] and clean [98] regimes. The long-range effects can, however, be limited by interface quality and impurities [99]. These earlier works show that ferromagnets with an intrinsic conical magnetic structure are of particular interest when studying superconducting proximity effects in F/S nanostructures. Triplet generation in F/S systems, where the magnetic structure of F is inhomogeneous, requires only a *single* F layer, an obvious advantage from the fabrication point of view. Although all the odd triplet components can also be induced in misaligned F/S structures with multiple F layers, such as F_1F_2S trilayers (see Chap. 2), the situation is quite different. In that case one studies the switching effect that occurs with the angle between the exchange fields and studies the physics behind. Here, motivated by the recent experiments mentioned above, we explore the importance of the geometry and the inherent conical magnetism in the single F layer system.

In addition to the standard reentrance with d_F mentioned above, we report in this chapter that superconductivity in conical-ferromagnet/superconductor bilayers can be reentrant *with temperature*. That is, the Cooper pair amplitude in such structures can be non-vanishing in a range $T_{c1} < T < T_{c2}$. Reentrant superconductivity associated with magnetic ordering of this kind was first observed in the ternary rare-earth compounds $ErRh_4B_4$ and $HoMo_6S_8$ [100, 101, 102, 103, 104] more than thirty years ago. Upon cooling, these compounds first become superconducting at a critical temperature T_{c2}. Upon further cooling they become magnetic. Magnetism and superconductivity then coexist [105] over a very narrow [106] T range: the onset of long-range ferromagnetic order is nearly immediately followed by the destruction of superconductivity at a second critical temperature T_{c1}. Thus, the reason for the disappearance of the superconductivity at T_{c1} is essentially the presence of the magnetism. That nonuniform magnetic ordering can appear in the presence of superconductivity is consistent with the prediction made by Anderson and Suhl [107].

The reentrance we find in conical-ferromagnet/superconductor bilayers is very different from that in $ErRh_4B_4$ and $HoMo_6S_8$. There, the high T phase is paramagnetic and the low T phase is ferromagnetic. In our case, the magnetic order remains unchanged: it is the same above T_{c1}, below T_{c2}, and *in between*. Reentrance occurs also [108] in some quasi-one-dimensional compounds, but there the low T phase is insulating. In our case, we have true reentrance: the lowest T and highest T phases are the same, whereas

in the entire range in between, superconductivity and magnetism harmoniously coexist. This is unique. Superconducting reentrance occurs also in granular films [109], but it involves the turning on and off of the intergrain Josephson coupling. We are able to evaluate here the thermodynamic functions of the system as it undergoes the transitions (the lower one is also of the second order) and from their behavior one can glimpse the reasons for the occurrence of the reentrance. The physical reasons that account for the reentrance with T in conical-ferromagnet/superconductor bilayers are attributed to the proximity effects associated with the interference of Cooper pair amplitudes and the generation of triplet pairing correlations, resulting in a nontrivial competition between the entropies and condensation energies.

In this chapter, we present results for various properties of the proximity effects in F/S bilayers, where the F layer has a conical magnetic structure. We numerically find the self-consistent solutions to the BdG equations [57] and use them to compute important physical quantities. By linearizing the BdG equations, we calculate the critical temperature as a function of magnet thickness, exchange field strength and periodicity, and other parameters. We then discuss the effects of varying the superconductor thickness to coherence length ratio. We show that depending on the width of the superconductor, and for a broad range of magnetic strengths, reentrant behavior as a function of magnet thickness can arise. We find that under certain conditions, the superconductivity can also be reentrant with temperature [65]. To clarify these reentrant phenomena, we investigate the thermodynamic functions associated with the various ways reentrance can arise. We find that all components of the odd triplet correlations can be induced and discuss their long-range nature. We then characterize the important triplet long-range behavior by introducing the corresponding proximity lengths. We find that these lengths oscillate as a function of d_F, and depend on details of the magnetic texture. Reverse proximity effects are also studied to determine the magnetic influence on the superconductor: we calculate the local magnetization vector, revealing greater penetration into S for weaker exchange fields. Lastly, the spectroscopic information is presented by means of the local density of states in order to demonstrate consistency with the T_c results.

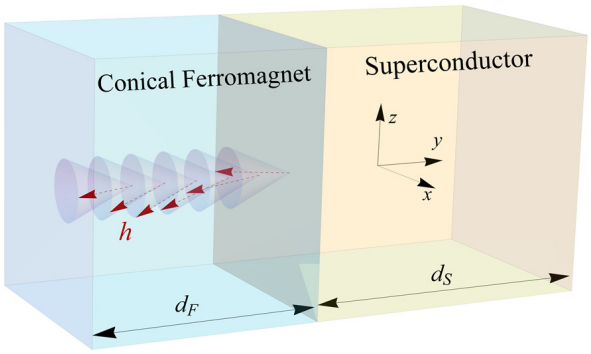

Figure 4.1: Diagram of the conical ferromagnet-superconductor bilayer studied. The conical magnetic structure is described by an exchange field $\boldsymbol{h}$ (see Eq. 4.1). The system is infinite in the $x-z$ plane and finite in y. The relevant widths are labeled.

4.2 Methods

The procedures we employ to self-consistently solve the BdG equations and to extract the relevant quantities are very similar to those previously described in Secs. 1.3 and 2.2. It is unnecessary to repeat details here. We consider F/S bilayers that consist of one ferromagnetic layer with spiral exchange fields and a superconducting layer with s-wave pairing. The geometry is depicted in Fig. 4.1. Our systems are infinite in the x-z plane and finite along the y-axis. Their total thickness is denoted by d: the F layer has a width of d_F and the S layer has a width of $d_S = d - d_F$. The left end of the bilayers is the $y = 0$ plane. We assume that the interface lies in the x-z plane and the exchange field $\mathbf{h}$, which is present only in F, has a component that rotates in this plane plus a constant component in the y direction perpendicular to the interface:

$$\mathbf{h} = h\left\{\cos\alpha\hat{\mathbf{y}} + \sin\alpha\left[\sin\left(\frac{\beta y}{a}\right)\hat{\mathbf{x}} + \cos\left(\frac{\beta y}{a}\right)\hat{\mathbf{z}}\right]\right\}, \tag{4.1}$$

where the helical magnetic structure has a turning angle β, and an opening angle α. We will take a, the lattice constant, as our unit of length and vary the strength h. The spatial period of the helix is $\lambda = 2\pi a/\beta$.

The effective Hamiltonian of our system is given by Eq. 1.10. Unlike our previous studies on F_1F_2S where the vector form of exchange fields only contains the in-plane components, but as for a conical ferromagnet, it contains an additional out-of-plane

component (along y-axis in our convention). Thus, it is inevitable to introduce the purely imaginary Pauli matrix, σ_y. To apply the BdG formalism to spatially inhomogeneous systems, we first invoke the generalized Bogoliubov [110] transformation, $\psi_\rho(\mathbf{r}) = \sum_n \left[u_{n\rho}(\mathbf{r})\gamma_n + v^*_{n\rho}(\mathbf{r})\gamma^\dagger_n\right]$, where $u_{n\rho}(\mathbf{r})$ and $v_{n\rho}(\mathbf{r})$ are quasiparticle and quasihole wavefunctions, and the creation operator $\gamma^\dagger_n$ and annihilation operator γ_n obey the usual fermionic anti-commutation relations. Note that the phase convention for the Bogoliubov transformation we adopted here is different than that for F_1F_2S trilayers in anticipation of the emergence of complex matrix elements in BdG equations. By recasting the effective Hamiltonian into a diagonalized form, via the commutation relations between $\mathcal{H}_{eff}$ and field operators, and making use of the quasi-one-dimensional nature of the problem, one arrives at the BdG equations,

$$\begin{pmatrix} \mathcal{H}_0 - h_z & -h_x + ih_y & 0 & \Delta(y) \\ -h_x - ih_y & \mathcal{H}_0 + h_z & -\Delta(y) & 0 \\ 0 & -\Delta(y)^* & -(\mathcal{H}_0 + h_z) & h_x + ih_y \\ \Delta(y)^* & 0 & h_x - ih_y & -(\mathcal{H}_0 - h_z) \end{pmatrix} \begin{pmatrix} u_{n\uparrow}(y) \\ u_{n\downarrow}(y) \\ v_{n\uparrow}(y) \\ v_{n\downarrow}(y) \end{pmatrix} = \epsilon_n \begin{pmatrix} u_{n\uparrow}(y) \\ u_{n\downarrow}(y) \\ v_{n\uparrow}(y) \\ v_{n\downarrow}(y) \end{pmatrix}, \quad (4.2)$$

where $\mathcal{H}_0$ is the usual single particle Hamiltonian for the quasi-one-dimensional problem (see the text below Eq. 2.1). With the phase convention we adopted here, the self-consistency relation becomes,

$$\Delta(y) = \frac{g(y)}{2} \sum_n{}' \left[u_{n\uparrow}(y)v^*_{n\downarrow}(y) - u_{n\downarrow}(y)v^*_{n\uparrow}(y)\right] \tanh(\frac{\epsilon_n}{2T}), \quad (4.3)$$

As usual, we find T_c by linearizing the self-consistency relation, Eq. 4.3, and using a perturbation expansion as discussed in Sec. 2.2.

Once a full set of self-consistent solutions is obtained, all the additional quantities of interest can be computed. For example, the triplet correlations corresponding to $m = 0$ and $m = \pm 1$, respectively [33, 34], can be written with our geometry and phase conventions associated with the Bogoliubov transformation in terms of the quasiparticle and quasihole wavefunctions:

$$f_0(y,t) = \frac{1}{2} \sum_n \left[u_{n\uparrow}(y)v^*_{n\downarrow}(y) + u_{n\downarrow}(y)v^*_{n\uparrow}(y)\right] \zeta_n(t), \quad (4.4a)$$

$$f_1(y,t) = \frac{1}{2} \sum_n \left[u_{n\uparrow}(y)v^*_{n\uparrow}(y) - u_{n\downarrow}(y)v^*_{n\downarrow}(y)\right] \zeta_n(t), \quad (4.4b)$$

where $\zeta_n(t) \equiv \cos(\epsilon_n t) - i \sin(\epsilon_n t) \tanh(\epsilon_n/(2T))$. As discussed in Sec. 4.1, both f_0 and f_1 have to vanish at $t = 0$ to comply with the Pauli principle.

Another important physical quantity, which can be determined experimentally by tunneling spectroscopy, is the local density of states (LDOS). This quantity often reveals important information about the superconducting features of the sample studied. In our quasi-one-dimensional model, the LDOS $N(y, \epsilon)$ depends spatially only on y. It can be easily rewritten, as shown in Chap. 2, in terms of the wavefunctions.

Just as the superconducting order parameter is changed by the presence of ferromagnets, near the interface, the ferromagnetism can also be modified by the presence of the superconductor [16, 75, 76, 77, 78, 111, 112]. As stated in Sec. 2.2, the reverse proximity effect is best described by considering the local magnetization, $\mathbf{m}$, which is in our case three-dimensional. In terms of the wavefunctions and with the phase convention in mind, the three components can be written as:

$$\begin{aligned} m_x(y) =& -\mu_B \sum_n \Big\{ \left(u^*_{n\uparrow}(y)u_{n\downarrow}(y) + u^*_{n\downarrow}(y)u_{n\uparrow}(y)\right) f_n \\ &+ \left(v_{n\uparrow}(y)v^*_{n\downarrow}(y) + v_{n\downarrow}(y)v^*_{n\uparrow}(y)\right)(1 - f_n) \Big\}, \end{aligned} \tag{4.5a}$$

$$\begin{aligned} m_y(y) =& i\mu_B \sum_n \Big\{ \left(u^*_{n\uparrow}(y)u_{n\downarrow}(y) - u^*_{n\downarrow}(y)u_{n\uparrow}(y)\right) f_n \\ &+ \left(v_{n\uparrow}(y)v^*_{n\downarrow}(y) - v_{n\downarrow}(y)v^*_{n\uparrow}(y)\right)(1 - f_n) \Big\}, \end{aligned} \tag{4.5b}$$

$$\begin{aligned} m_z(y) =& -\mu_B \sum_n \Big\{ \left(|u_{n\uparrow}(y)|^2 - |u_{n\downarrow}(y)|^2\right) f_n \\ &+ \left(|v_{n\uparrow}(y)|^2 - |v_{n\downarrow}(y)|^2\right)(1 - f_n) \Big\}, \end{aligned} \tag{4.5c}$$

where f_n is the Fermi function of ϵ_n and μ_B is the Bohr magneton. Here expressions for all three components are needed due to the conical-type magnetizations.

4.3 Results

In the results shown here, all the dimensionless thicknesses are measured in units of a, as mentioned above, and denoted by capital letters in our conventions (see the beginning of Sec. 2.3). For the conical magnetic structure, we take angular values (see Eq. 4.1)

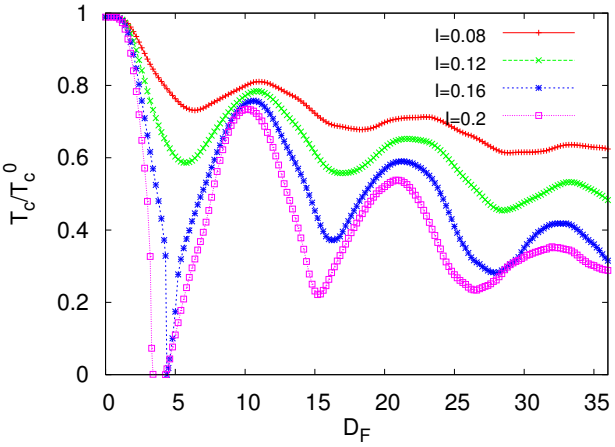

Figure 4.2: Calculated transition temperatures T_c, normalized to T_c^0, vs D_F for several values of the dimensionless exchange field I (see text). In this figure D_S is fixed for all values of I to be $1.5\Xi_0$. The lines connecting data points are guides to the eye.

$\alpha = 4\pi/9$ and $\beta = \pi/6$, which are [92, 113] appropriate to Ho, in which case, the magnet thickness $D_F = 12$ contains one full period of the spiral exchange field. We will denote this dimensionless spatial period by Λ in the following subsections. For materials other than Ho, many of the results can be read off by rescaling Λ to an appropriate value. Throughout this chapter, the dimensionless superconducting coherence length is fixed to be $\Xi_0 = 100$. As in previous chapters, the dimensionless exchange field, I, is measured in terms of the Fermi energy: $I \equiv h/E_F$. We set the Fermi wavevector in S to equal $1/a$. We take the "Debye" cutoff value to be $\omega_D = 0.04E_F$. As usual, this value is irrelevant except for setting the overall transition temperature. Temperatures are given in dimensionless form in terms of T_c^0, the transition temperature of the bulk S material. When discussing the triplet amplitudes, which are time dependent, we use the dimensionless time $\tau \equiv \omega_D t$ as usual. Vertical dashed lines shown in figures, when present, denote the F/S interface.

4.3.1 Transition temperatures

To investigate the details of the predicted oscillatory nature of the d_F dependence of T_c, as discussed in Sec. 4.1, we calculated T_c as a function of D_F for several I and D_S, the width of superconductors. These results are shown in Fig. 4.2 and Fig. 4.3. The D_F

range in both figures includes three complete periods of the spiral magnetic order. This is reflected in the results shown: the presence of multiple oscillations in the included range of D_F is the most prominent feature in Figs. 4.2 and 4.3. The oscillations in T_c arise, as we discuss below, from a combination of the periodicity of the spiral magnetic structure and the usual T_c oscillations which arise, even when the magnet is uniform, from the difference [13, 15] in the wavevectors of the up and down spins (see Sec. 1.2). In Fig. 4.2, one can also see that with stronger exchange fields the oscillation amplitudes are larger. Despite this increase of the amplitudes with the exchange field (they are approximately proportional to I), the overall T_c decreases when the exchange field increases. This is consistent with expectations: a stronger exchange field destroys the superconductivity more efficiently. As mentioned in Sec. 4.1, when the exchange field is strong enough, the systems can become normal in some range $D_{F1} < D_F < D_{F2}$. Indeed, reentrance with d_F can be seen to occur in Fig. 4.2 near $D_F = 4$ at $I = 0.2$. Another feature seen in this figure is the decrease of the amplitude oscillations with increasing D_F. This arises simply because the singlet Cooper pair amplitudes in S near the F/S boundary decay more strongly at a larger d_F and therefore the effect of the pair amplitude oscillations in F is weaker [44].

In a F/S bilayer, where the ferromagnet is homogeneous, the periodicity of the T_c oscillations is governed by the exchange field, or equivalently, by the magnetic coherence length [16] $\Xi_F = 1/I$. Here, where a bilayer with a conical inhomogeneous ferromagnet is considered, the intrinsic spiral magnetic order with spatial period Λ plays an equally important and competing role in the T_c oscillations. In other words, both the strength and the periodicity of exchange fields influence the overall decay and the oscillatory nature of the superconducting transition temperatures. The existence of two different spatial periodicities leads to the obvious consequence that the $T_c(D_F)$ curves are not describable in terms of one single period. However, when I is not very strong ($I \lesssim 0.1$), the minima of T_c are near the locations where $D_F = \Lambda/2$, $3\Lambda/2$, and $5\Lambda/2$ and similarly, the T_c maxima occur near $D_F = \Lambda$, 2Λ, and 3Λ. This indicates that the magnetic periodicity is dominant. Roughly speaking, the maxima and the minima are correlated with the strongest and weakest spatial average of the exchange field components in F. As I increases and Ξ_F decreases, deviations become obvious. Figure 4.2 shows that the distances between two successive maxima decrease when the exchange fields increase.

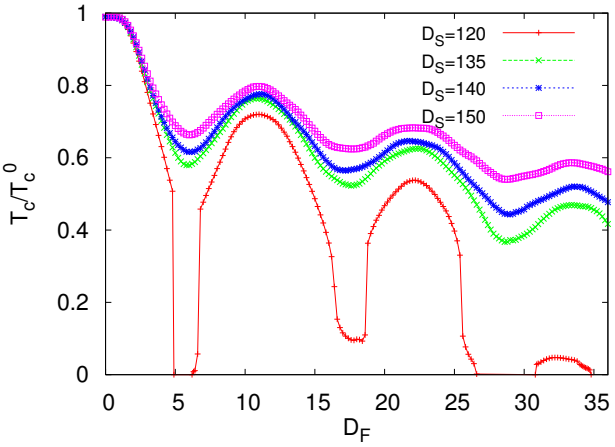

Figure 4.3: Transition temperatures T_c vs D_F at $I = 0.1$ and several D_S. The lines are guides to the eye.

The existence of the multiple oscillations discussed above has been confirmed experimentally. In Ref. [56], T_c in Nb/Ho bilayers was measured as a function of d_F. The results exhibit an overall decay with Ho thickness, on which there are superimposed oscillations which are correlated with, but not simply described by the spatial wavelength λ of the Ho structure. Comparison with the theoretical results discussed here will be made in next chapter, using I as an adjustable parameter. Values near $I = 0.1$ were found to provide the best fit. The other parameters were extracted from other known properties of Ho and Nb or (e.g. d_S) from the experimental sample geometry. The results of the comparison were extremely satisfactory, showing a clear agreement in all the features of the rather intricate $T_c(d_F)$ experimental curves. It was also found that one of the samples was close to being reentrant with d_F at a value very close to that predicted by theory.

In Fig. 4.3, we present T_c results for several values of D_S, ranging from $1.2\Xi_0$ to $1.5\Xi_0$, with a fixed exchange field $I = 0.1$. One can see that the distance between successive maxima is an extremely weak function of D_S. This agrees with our previous discussion: the oscillatory nature in T_c is chiefly dependent on the exchange fields and magnet structure. Since superconductivity is more robust for larger D_S, the ferromagnet lowers the overall T_c for thinner superconductors as evidenced in Fig. 4.3. Figure 4.3 also demonstrates that not only can a strong I lead to D_F reentrances, but also a thinner

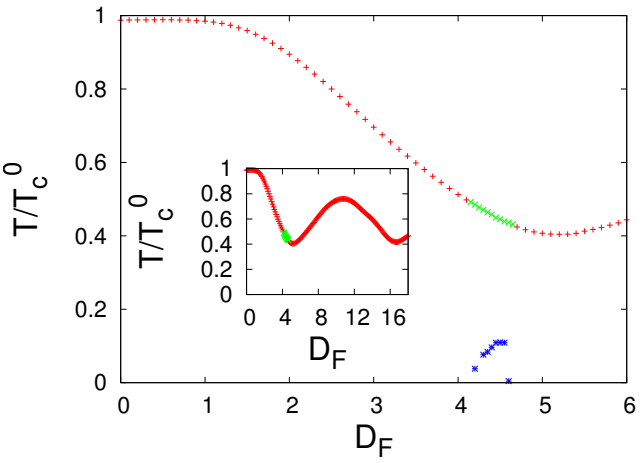

Figure 4.4: Normalized transition temperature T_c vs D_F at $I = 0.15$ and $D_S = 1.5\Xi_0$. Main plot: The upper points ((red) + , (green) $\times$ signs) are the usual critical temperature (T_{c2}), leading to the superconducting state as T is lowered. In the region $4 \lesssim D_F \lesssim 5$ (highlighted by the (green) $\times$ signs) a second transition back to the normal state appears at the (blue) star points forming the lower "dome". The inset shows a broader range of magnet widths, revealing the overall periodicity of T_{c2}.

D_S. Interestingly, at the smallest value of D_S considered, there are two D_F reentrance regions, one near $D_F = 5$ and the other near $D_F = 27$. As discussed above, these D_F reentrances in both Figs. 4.1 and 4.2 are mainly due to the interference between the transmitted and reflected Cooper pair condensates that are oscillatory in the F region.

Next, we report two examples where superconductivity in F/S bilayers, with F being conical ferromagnets, exhibits not only the usual reentrance with d_F but also, at some fixed values of d_S, h, and d_F, reentrance with T, that is, superconductivity exists only in a temperature range $T_{c1} < T < T_{c2}$, where T_{c1} is finite. The first example plotted in Fig. 4.4, with parameters defined in the caption, shows temperature reentrance occurred near the first minimum of the $T_c(D_F)$ curve. In the inset, we see that the overall behavior of T_c consists of the expected damped oscillations with approximately the D_F periodicity of Λ. The main plot shows in more detail the structure near the first minimum. There we also see a lower small dome-shape plot ((blue) stars) with a maximum at $D_F \approx 4.5$. The system is in the normal phase inside the dome and, at constant D_F, it is in the superconducting phase between the two curves. In the D_F range, including the dome,

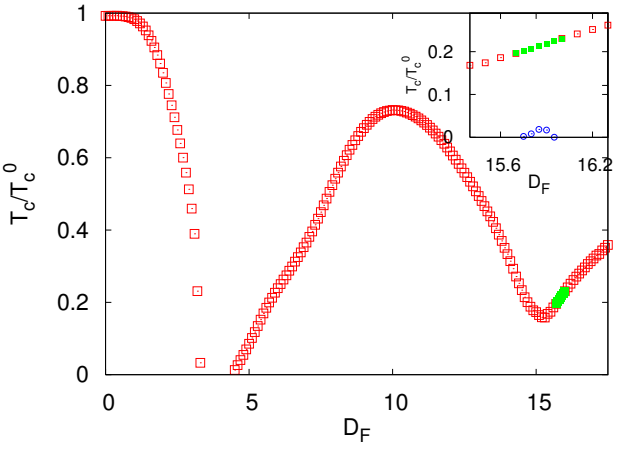

Figure 4.5: Calculated transition temperatures T_c vs D_F for $D_S = 148$ and $I = 0.2$. The main plot shows ((red) symbols) the overall T_c behavior from $D_F = 0$ to $D_F = 1.5\Lambda$. Reentrance with D_F near $D_F = 4$ is seen. In this case there is also reentrance with temperature in the region indicated by (green) solid squares near D_F=16. The inset is a blow up of this region: superconductivity exists only in the region $T_{c1} < T < T_{c2}$, where T_{c2} is depicted by the upper (green) squares and T_{c1} by the (blue) circles.

the system upon cooling first becomes superconducting at a higher temperature T_{c2}, and with further cooling, returns to the normal phase at a lower temperature T_{c1}.

We have also demonstrated here whether this kind of reentrance can occur near some of the other minimum of $T_c(D_F)$. These locations appear favorable for such an occurrence since superconductivity is relatively weak near these minima. Also, reentrance with D_F is after all an extreme case of a minimum $T_c(D_F)$. We have found that other T-reentrant examples can indeed be found, although by no means universally. We plot the other example of reentrance occurring near the second minimum of $T_c(D_F)$. At this larger value of D_F, it should be much easier to grow Ho in the spiral structure. In Fig. 4.5, the main plot shows $T_c(D_F)$ for the parameter values specified in the caption. The first minimum of $T_c(D_F)$ drops to zero and is an example of D_F reentrance. In the region near the second minimum ((green) solid squares), reentrance with T occurs. The region of interest is enlarged in the inset (note that, in Fig. 4.4, we plotted the region of interest in the main plot and a wider region of $T_c(D_F)$ in the inset). There the upper (green) solid squares represent T_{c2} and the small dome of lower (blue) circles represent T_{c1}. Again, inside the dome, but not outside of it, the superconductivity is reentrant in

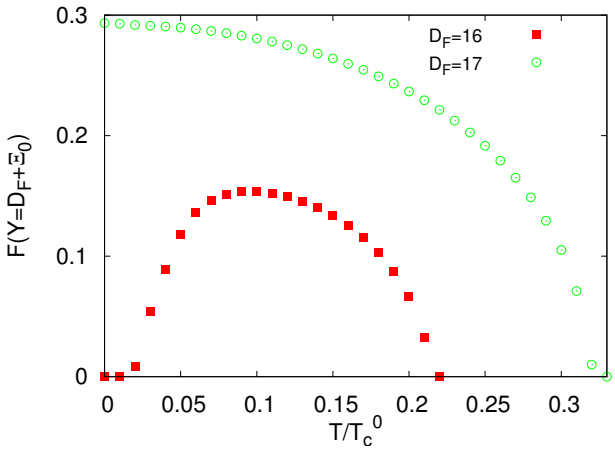

Figure 4.6: The singlet pair amplitude, normalized to its value for bulk S material, at a location one coherence length inside S from the F/S interface, plotted as a function of T. The (red) squares are for $D_F = 16$ and the (green) circles are for $D_F = 17$. All other parameters are as in Fig. 4.5.

T. Reentrance in this case occurs at the second minimum rather than the first because there is no upper transition associated with the first minimum: the system is normal. Near the second minimum, the oscillatory effects are not as strong, and as as a result, the system becomes reentrant in T. This can be viewed as a "compromise": near the second minimum, as opposed to the first, superconductivity is not completely destroyed but it becomes "fragile" and can disappear upon lowering T. The physics involved from a thermodynamic point of view will be discussed in the following subsection.

4.3.2 Thermodynamics of reentrance phenomena

To understand the reentrance phenomena in T, it is most useful to examine the thermodynamics of the two transitions and in the region between them. From the condensation free energy ΔF, which can be evaluated as explained in connection with Eq. 2.7, other quantities such as the condensation energy and entropy are easily obtained. For reentrance with D_F, it is sufficient to look at the free energy at constant low T.

Here we first discuss these quantities for the example shown in Fig. 4.5. Considering the reentrance with T, it is illuminating to consider the T dependence of the singlet pair amplitude $F(Y)$ well inside the S material. Thus, we focus on $F(Y)$ one coherence

length from the interface: $Y = D_F + \Xi_0$. This quantity, normalized to its value in bulk S material, is plotted in Fig. 4.6 as a function of T for two contrasting values of D_F, one at $D_F = 16$ where reentrance occurs (see Fig. 4.5) and at a very nearby value, $D_F = 17$, which lies just outside the reentrance region and exhibits typical behavior. Figure 4.6 ((green) circles) demonstrates that in the latter case the amplitude behaves qualitatively as the order parameter does in a conventional BCS superconductor: it decreases very slowly near $T = 0$ and eventually drops to zero very quickly but continuously near T_c, indicating the occurrence of a second order phase transition. This transition occurs at $T_c/T_c^0 = 0.32$ in agreement with Fig. 4.5. However, the behavior of the pair amplitude in the reentrant region ((red) squares in Fig. 4.6) is quite different. There are two transition temperatures: below a very low but finite temperature, $T_{c1}/T_c^0 = 0.02$, the singlet pair amplitude vanishes and the system is in its normal state. $F(Y)$ then begins to rise continuously, has a maximum at a temperature T_m, (where $T_m/T_c^0 \approx 0.1$) and eventually drops to zero continuously again at an upper transition $T_{c2}/T_c^0 \approx 0.22$. In the region $T_{c1} < T < T_{c2}$ the system is in the superconducting state. Both transitions are of the second order. The values of T_{c1} and T_{c2} from the vanishing of the amplitude, seen in Fig. 4.6, agree with those calculated directly from linearization of the self-consistent equation plotted in Fig. 4.5.

We now turn to the condensation free energy, ΔF, and entropy, ΔS, for the same T-reentrant case. ΔF is shown in the top panel of Fig. 4.7 as calculated from Eq. 2.7 and normalized by $2E_0$, where E_0 is the condensation energy of bulk S material at $T = 0$. The lower panel shows the normalized condensation entropy, defined as the $\Delta S \equiv -d\Delta F/d(T/T_c^0)$. The meaning of the symbols in this figure is the same as in the previous one. When the system is near (but outside) the reentrant region, the behavior of both quantities plotted is qualitatively the same as that found in textbooks for bulk BCS superconductors. Quantitatively, the magnitude of ΔF for our systems are much smaller than that for bulk S where we would have $\Delta F = -0.5$ at $T = 0$ in our units. The value of T_c in the non-reentrant case can also be identified from where the free energies of the normal and superconducting states are the same ($\Delta F(T) \equiv 0$), and it agrees with both Figs. 4.5 and 4.6. Moreover, the vanishing of the entropy difference at a finite T_c confirms the occurrence of a second order phase transition. The value of this transition temperature is consistent with all above results.

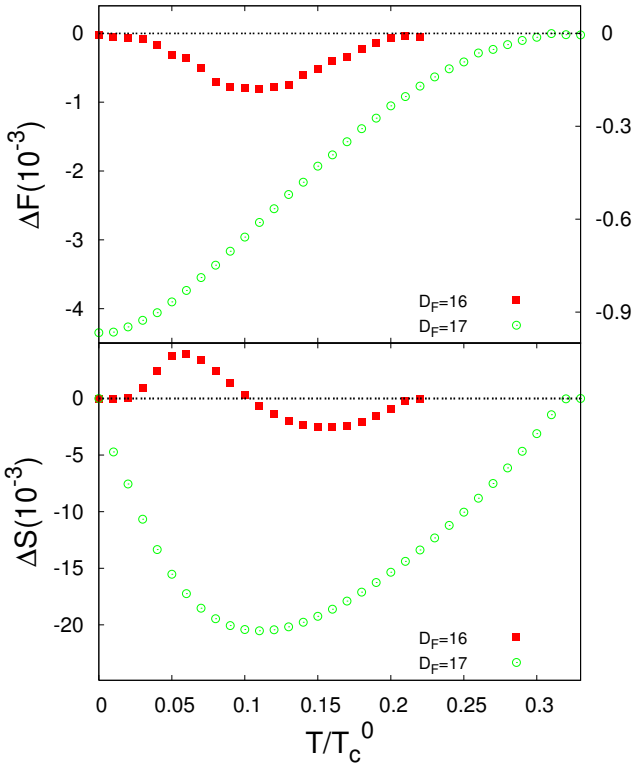

Figure 4.7: The normalized condensation free energies, $\Delta F = F_S - F_N$, vs T/T_c^0 are shown in the top panel for the same cases presented in Fig. 4.6. The (red) squares and right scale are for $D_F = 16$. The (green) circles and left scale are for $D_F = 17$. The bottom panel shows the normalized (see text) entropy differences, $\Delta S = S_S - S_N$ vs T/T_c^0, on the same vertical scale. The meaning of the symbols is the same as in the top panel.

The story for the reentrant case is quite different. Although the values of ΔF are much smaller compared to those in the standard case, one can still find that the minimum of ΔF occurs at approximately the same value T_m where the singlet pair amplitudes have a maximum. Thus, the superconductivity is most robust at $T = T_m$. The two transition temperatures T_{c1} and T_{c2} can also be determined from the top panel of Fig. 4.7 and match with those found in Fig. 4.5 and 4.6. In the two T ranges $T < T_{c1}$ and $T > T_{c2}$, the normal state is the only self-consistent solution to the basic equations, as evident from Fig. 4.6. The vanishing ΔF when $T < T_{c1}$ implies that the electrons do not then condensate into Cooper pairs. This is exactly what happens for

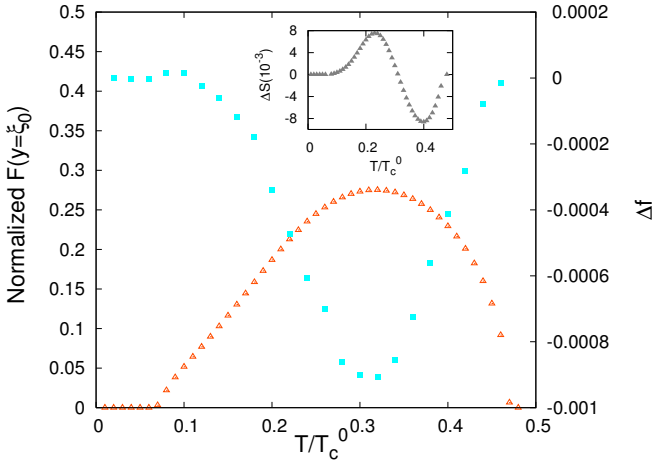

Figure 4.8: Behavior of the pair amplitude and the thermodynamics corresponding to Fig. 4.4. In the main plot, the (red) triangles and left vertical scale display the normalized (see text) singlet Cooper pair amplitude $F(Y)$, one correlation length inside S. This quantity vanishes at the upper transition temperature (about $0.47T_c^0$) and again at the lower transition of about $0.07T_c^0$. The (blue) squares and right scale are the normalized condensation free energy, Δf. The inset shows the normalized entropy difference $\Delta S \equiv -(d\Delta f/d(T/T_c^0))$.

pure superconductors when $T > T_c$.

There are some remarkable facts about the behavior of ΔS in the reentrant case. First, the vanishing of ΔS (along with that of ΔF) in Fig. 4.7 indicates that the system undergoes second order phase transitions at both T_{c1} and T_{c2}. Also, ΔS is positive for $T_{c1} < T < T_m$, where T_m is again the value of T at which the singlet pair amplitude reaches its maximum *and* ΔF its minimum. That the entropy of the superconducting state is higher than that of the normal state indicates that the normal state at $T_{c1} < T < T_m$ is *more* ordered than the superconducting one. This truly unusual fact, which is the root cause of the reentrance, is due to the oscillating nature of both the Cooper pair condensates and of the exchange field, which leads to an uncommonly complicated structure for the pair amplitude. Above T_m, the superconducting state becomes more ordered than the normal state: ΔS is negative. From Figs. 4.6 and 4.7, we see that the singlet pair amplitudes, the condensation free energies, and the entropy differences of reentrant case in the range $T_m < T < T_{c2}$ have a similar trend to those of non-reentrant

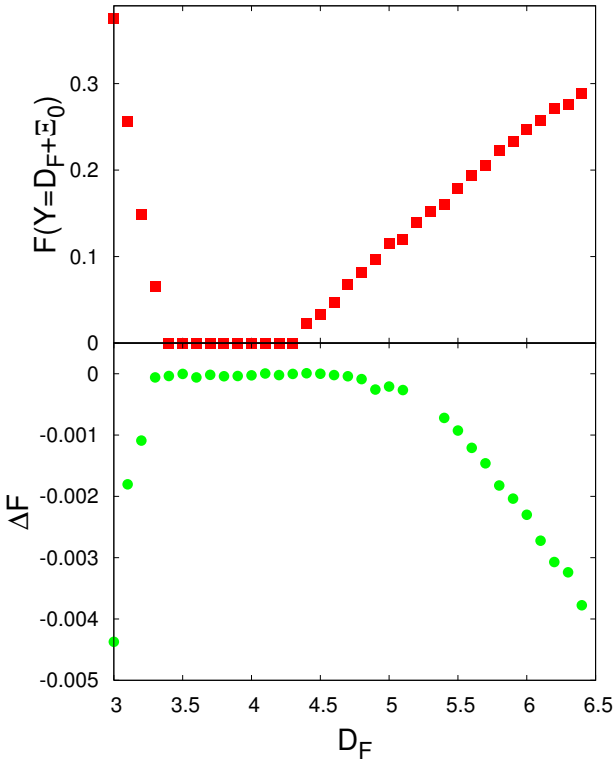

Figure 4.9: Reentrance with D_F. Top panel: normalized singlet pair amplitude, computed at a location one coherence length inside S from the interface, as a function of D_F. Bottom panel: normalized condensation free energy, $\Delta F = F_S - F_N$, vs D_F at $T = 0$.

case in the range $0 < T < T_c$. We have also found examples of non-reentrant cases in which there is a finite temperature T_m at which ΔF has a minimum but upon further lowering T, ΔF remains negative all the way to $T = 0$.

The singlet pair amplitudes and thermodynamics for the case where the reentrance with T occurs at the first minimum of $T_c(D_F)$ phase diagram are also shown in Fig. 4.8. One can immediately see that these quantities exhibit similar behavior to those discussed above and they are consistent with the $T_c(D_F)$ phase diagram. However, by comparing the magnitudes of both pair amplitudes and condensation free energies between these two cases, we find that the first-minimum reentrance are thermodynamically more stable than the second-minimum reentrance.

The situation in the more common D_F reentrance region, where we find that the system does not become superconducting when it is heated from $T = 0$, is different from that of T reentrance. A case where T_c vanishes in the range $D_{F1} < D_F < D_{F2}$ for $I = 0.2$ was seen in Fig. 4.2. To further analyze this D_F reentrance, we again calculated the singlet pair amplitudes inside S at one coherence length from the interface in the zero temperature limit. The top panel of Fig. 4.9 shows the normalized $F(D_F + \Xi_0)$ as a function of D_F for the same parameters as the $I = 0.2$ case in Fig. 4.2. The singlet amplitudes drop to zero in the same range as where T_c vanishes in Fig. 4.2: the normal state is the only self-consistent solution and the superconductivity is completely destroyed in this D_F range. One can also see that the order parameter is continuous, but its derivative is discontinuous at D_{F1} and D_{F2}. In the bottom panel, we plot the corresponding condensation free energies (at $T = 0$) as a function of D_F. The D_F range and the temperature are the same as the top panel. The condensation free energies vanish in the same D_F reentrance region although their extreme smallness (at the level of our numerical uncertainty as can be gauged by the size of the points) at slightly larger values of D_F makes it difficult to verify in this panel that the regions are exactly the same. Unlike the derivatives of the singlet pair amplitudes, the derivatives of ΔF at D_{F1} and D_{F2} appear to be continuous.

The physical origins of these two kinds of reentrance are not identical. As mentioned in Sec. 4.1, the interference effects of oscillating Cooper pair wavefunctions are responsible for the D_F reentrance, provided that I is strong and D_F is not too thick. D_F reentrance does not require a nonuniform magnet. The conical-ferromagnet structure introduces an additional nonuniform magnetic order which may coexist with nonuniform superconductivity, as predicted in Ref. [107]. This additional nonuniformity, with its concomitant introduction of triplet correlations and of a new periodicity, can produce, as we have shown, reentrant behavior in T, as opposed to the simpler behavior seen near the first minimum in the main plot of Fig. 4.5. Thermodynamically, the reentrance with T is due to the competition between entropy and energy [65], and driven by the high entropy of the disordered superconducting state. When $T < T_m$, ΔS is positive and the roles of the normal and superconducting phases are exchanged: the high entropy phase is the superconducting one. Further lowering of T brings the system back to normal state. For the case where T reentrance occurs near the first minimum of $T_c(D_F)$, one

can find that not only is D_S thinner but also I is greater than the one that occurs near the second minimum. The first minimum of $T_c(D_F)$ in the main plot of Fig. 4.5 drops to zero and becomes a D_F reentrance region. Because a stronger I and a thinner D_S are unfavorable to superconductivity, the system can not sustain T reentrance there. Thus, a delicate balance of geometrical and material parameters is required.

4.3.3 Singlet to triplet conversion

In this subsection, we will discuss the general properties of the induced triplet pairing correlations in F/S bilayers with F being a conical ferromagnet. As mentioned in Sec. 4.1, in the presence of inhomogeneous exchange fields in the F layers both the $m = 0$ and $m = \pm 1$ triplet pair amplitudes are *allowed* by conservation laws and the Pauli principle, but this says *nothing* about their size or shape, or whether they will exist at all. Thus, detailed calculations are needed. The intrinsically inhomogeneous magnetic textures discussed here provide unique opportunities to study the triplet proximity effects in F/S systems containing only a single F layer. Triplet correlations in the ballistic regime for both F_1SF_2 and F_1F_2S trilayers have been found in previous work [33, 34, 52] and have been discussed in Chap. 2 to be long ranged and the expectation [38] that they will also be in our case is fulfilled. We will here discuss and characterize this and other aspects (such as the effect of the strength of the exchange fields on the triplet pair amplitudes) of the triplet pairing correlations in F/S bilayers where the magnets maintain a spiral exchange field. Results presented in this subsection are all in the low T limit.

To exhibit the long-range nature of both types of triplet amplitudes, we show in Fig. 4.10 both the triplet and singlet pair amplitudes for a thick F layer as a function of position, as given by the dimensionless coordinate Y. In this and the next figure, Fig. 4.11, we will focus on the real parts of the generally complex (see Eqs. 4.4) f_0 and f_1, since we have found that, for the cases shown, their imaginary parts are smaller by at least a factor of 2 to 5, and their behavior is similar to that of real parts. To properly compare singlet and triplet quantities, both the singlet amplitude $F(Y)$ and the triplet amplitudes are normalized in the same way: to the value of the singlet amplitude in bulk S material. For visibility, we have multiplied the triplet pair amplitudes by a factor of 10. In the left and right columns of Fig. 4.10, we show the real parts of both f_0 and

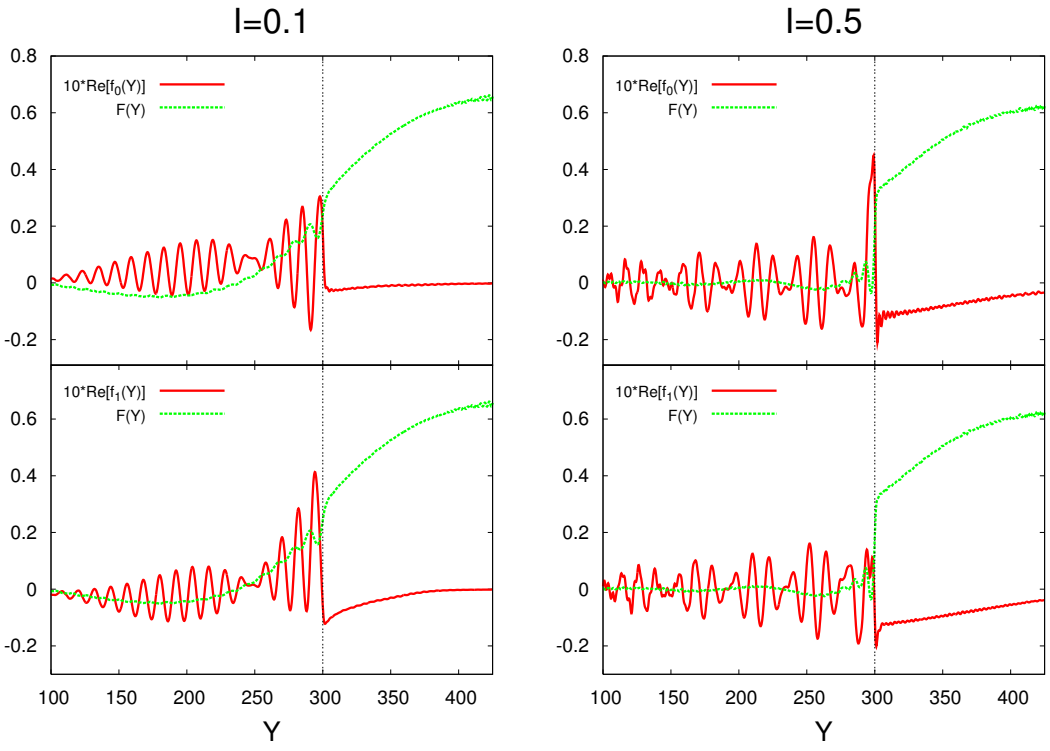

Figure 4.10: Comparison between the spatial dependencies of the singlet pair amplitude and the induced triplet correlations at the two indicated values of I, at $D_S = 150$, $D_F = 300$ and $T = 0$. The S region is to the right of the dashed vertical line. Both singlet, $F(Y)$, ((green) curves higher in the S region) and triplet, $f_0(Y)$, $f_1(Y)$, pair amplitudes are normalized to the value of $F(Y)$ in pure bulk S material. For this comparison, the normalized induced triplet pair amplitudes, which are evaluated at $\tau = 9.6$, are multiplied by a factor of 10. The real parts of $f_0(Y)$ and $f_1(Y)$ are shown ((red) curves strongly oscillating in the F region)).

f_1 when $I = 0.1$ and $I = 0.5$, respectively. The ferromagnet has a large thickness: $D_F = 3\Xi_0 = 2D_S$. The triplet correlations, which we recall vanish at equal times, are computed at a value of the dimensionless time $\tau = 9.6$. One sees right away that both the f_0 and f_1 components can be induced simultaneously. This is always the case in our structures, as opposed to what occurs in F_1F_2S and F_1SF_2 trilayers where the f_0 and f_1 components can be induced simultaneously only when the exchange fields in these F layers are noncollinear. Secondly, the induced triplet correlations on the F side are long ranged compared to the singlet amplitudes. The singlet amplitudes decay with a short [16] proximity length $2\pi\Xi_F \approx 2\pi/I$ due to the pair-breaking effect of the exchange field. In contrast, the proximity length for the triplet amplitudes as seen in Fig. 4.10 is much longer: it is of the order of Ξ_0, and does not strongly depend on I. The triplet amplitudes spread over the F side with an oscillatory behavior. This difference is more pronounced when $I = 0.5$, where the decay length Ξ_F is much shorter than Ξ_0, and the singlet amplitudes diminishes much faster than when $I = 0.1$. For both $I = 0.1$ and $I = 0.5$, one can also see that the singlet amplitudes begin to rise from the F/S interface and saturate in the S side about one superconducting coherence length from the interface. This agrees with previous work [16]. Another interesting feature seen in the $I = 0.5$ case is that the peak height of the f_1 component near the interface is not much higher than that of its other peaks, as happens with its f_0 counterpart. In other words, the subsequent peak heights in the F regions are comparable to that of the peak nearest to the interface.

In delineating the role of triplet correlations in other experimentally relevant quantities, it is necessary to understand their time dependence. Due to the self-consistent nature of the proximity effects and the fact that the triplet condensate amplitudes are odd in time, their time dependence is in general nontrivial. We illustrate this in Fig. 4.11, where we show the spatial dependence of both the $m = 0$ and $m = \pm 1$ components of the triplet amplitude for several τ. The parameters used here are the same as in the right panels ($I = 0.5$) of Fig. 4.10. For an easier comparison with Fig. 4.10, we have again multiplied the normalized triplet amplitudes by a factor of 10. Figure 4.11 shows that at small times triplet correlations are generated only near the interface. (We have of course verified that they always vanish when $\tau = 0$). One can extract information about the proximity length from the growing increase of peak heights in the F regions.

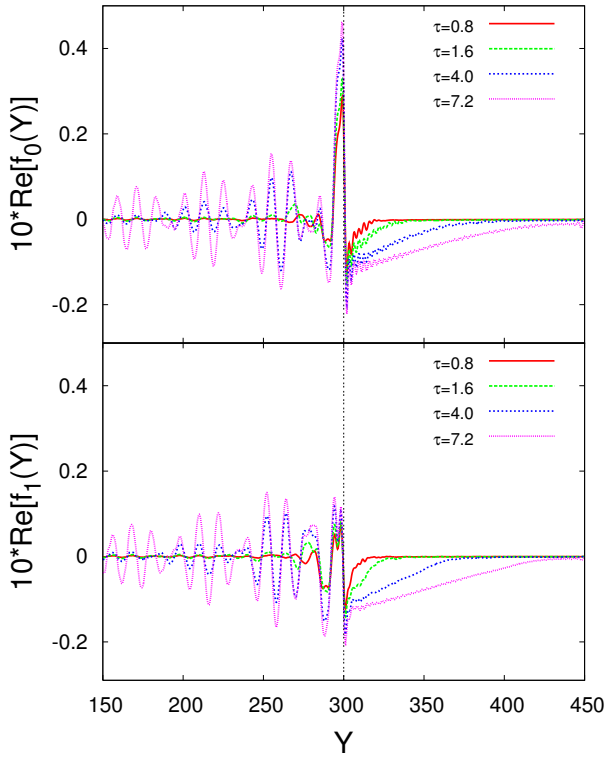

Figure 4.11: Real parts of the induced triplet pair amplitudes, normalized as in the previous figure, for different characteristic times τ. In these plots, $D_S = 150$, $D_F = 300$ and $I = 0.5$. The top panel shows the real part of $f_0(Y)$ and the bottom one that of $f_1(Y)$.

The peak heights grow faster when they are deeper inside the ferromagnet. Moreover, Fig. 4.11 clearly demonstrates that the triplet correlations penetrate into F regions as τ increases, in the range studied. Remarkably, the peaks of the f_1 component that are not nearest to the interface grow very fast in time and have heights that are comparable to the peak nearest to the interface, consistent with our remarks in our discussion of Fig. 4.10. In contradistinction with the oscillating behavior of the triplet amplitudes in the F regions, one can see that both f_0 and f_1 decay monotonically into the S side without any oscillations. However, the triplet correlations still spread over into the S regions at larger values of τ, just as they do in the F layer.

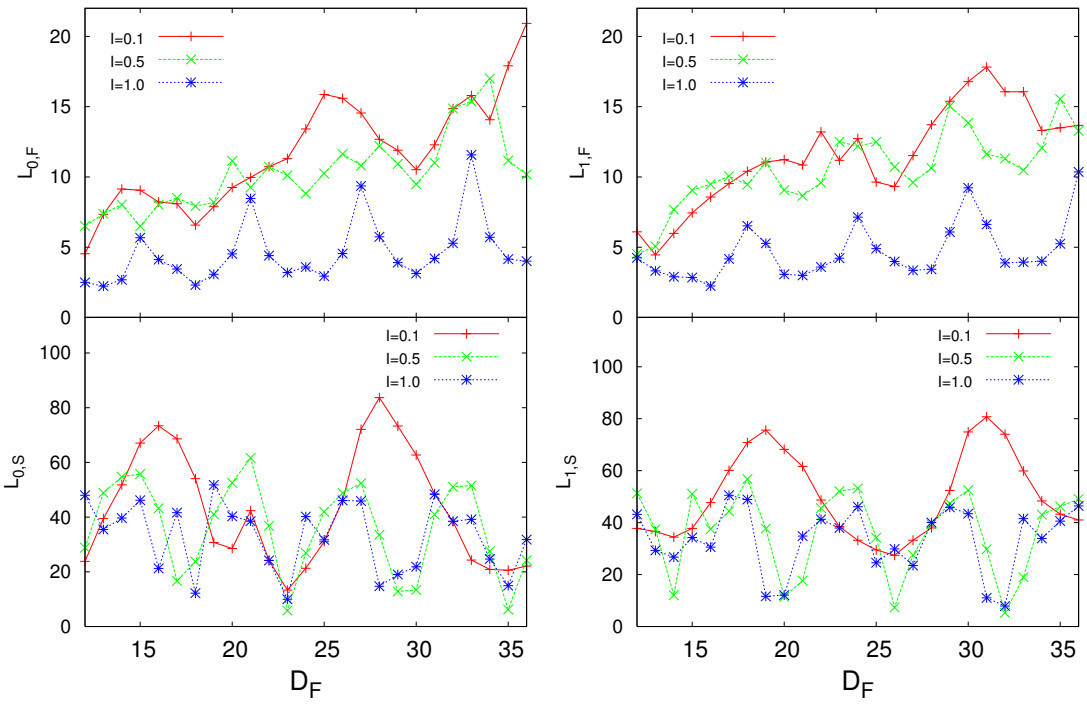

Figure 4.12: The proximity lengths $L_{i,M}$ (see Eq. 2.9) of the induced triplet pair amplitudes vs D_F for different I, at $\tau = 4.0$ and $D_S = 150$. The left panels show the proximity lengths $L_{0,F}$ and $L_{0,S}$ (from f_0 in the F and S regions) and the right panels $L_{1,F}$ and $L_{1,S}$, similarly extracted from f_1. The lines are guides to the eye.

In the above paragraphs, we have discussed the long-range nature and other properties of the triplet amplitudes in our system when the conical ferromagnet is very thick. In the following paragraphs, we will consider the proximity effect of induced triplet pairing correlations for smaller scale conical-ferromagnets. To quantify this effect we introduce a set of proximity lengths $L_{i,M}$, defined as in Eq. 2.9, with the first index denotes the spin component as usual, and the second index M denotes the region in which the given function is evaluated. If the decays were exponential, these lengths would coincide with the characteristic length in the exponent. Obviously, in the present situation, the decays are more complicated, but the $L_{i,M}$ can easily be extracted numerically. They depend on D_S, D_F, I, and τ. The range of D_F we will consider is from Λ to 3Λ. In Fig. 4.12, we plot these proximity lengths on both the F and S sides for

three different values of I at $\tau = 4.0$. The left panels show the f_0 proximity lengths and the right panels that were extracted from f_1. Recall that $I = 1$ corresponds to the half-metallic limit. We first consider the F side (top two panels). One can see that both $L_{0,F}$ and $L_{1,F}$ are correlated to the strength of the exchange fields. Figure. 4.12 displays a period of near $\Lambda/2$ for both $L_{0,F}$ and $L_{1,F}$ at $I = 1.0$. We also see that the peak heights slowly increase with increasing D_F. Also, the locations of the maxima (minima) of $L_{0,F}$ are locations of minima (maxima) of $L_{1,F}$. This is as one might expect from the rotating character of the field. On the other hand, at $I = 0.1$ or $I = 0.5$ the periodicity is not clear since, for reasons already mentioned, the intermingling of periodicities becomes more complicated. Overall, the proximity lengths are larger than those in the half-metallic limit. However, one can still say that both $L_{0,F}$ and $L_{1,F}$ gradually increase, although with fluctuations, with D_F.

The superconductor on the S side is intrinsically s-wave but because of the F layer, triplet correlations can be induced in it, near the interface, as seen in Figs. 4.10 and 4.11. Their decay, which is now monotonic, can be equally characterized by the proximity lengths defined in Eq. 2.9. Results are plotted in the bottom panels of Fig. 4.12. The minimum of $L_{0,S}$ is, for all three values of I, at $D_F = 23$, which is near 2Λ. The maxima of $L_{0,S}$ for $I = 0.1$ are at $D_F = 16$ and $D_F = 28$, which are not far from 1.5Λ and 2.5Λ, respectively. On the other hand, for $L_{1,S}$, the maxima for $I = 0.1$ are at $D_F = 19$ and $D_F = 31$, and there is a minimum at $D_F = 26$. The locations of these maxima are still near 1.5Λ and 2.5Λ and they are only slightly different than what they are for $L_{0,S}$ case. If one recalls the above discussion of Fig. 4.3, maxima of T_c occur when D_F is close to an integer multiple of Λ. Since a higher T_c is correlated with a higher singlet pair amplitude, this suggests again that there exists a conversion between singlet and triplet Cooper pairs. The dependence of $L_{0,S}$ and $L_{1,S}$ at $I = 1.0$ on D_F is harder to characterize because the high value of I reduces the scale of the overall proximity effect in S (i.e. the depletion of the singlet amplitude). At $I = 0.5$, one still finds that the approximate periodicity of $L_{0,S}$ and $L_{1,S}$ is roughly $\Lambda/2$. The proximity lengths $L_{0,S}$ and $L_{1,S}$ are again anti-correlated at $I = 0.5$: the maxima (minima) locations of $L_{0,S}$ are near the minimum (maximum) locations of $L_{1,S}$.

Recent experiments [38] in systems that consist of two superconducting Nb electrodes coupled via a Ho/Co/Ho trilayer have revealed that the long-range effect of triplet

supercurrents was much more prominent at particular thicknesses of the Ho layers. The magnetic coherence length of Ho in the experiment was $\sim 5\,\mathrm{nm}$, which would correspond in our notation to $I \sim 0.1$ [56]. In the experiment, the Ho thickness was symmetrically varied and the critical current, I_c, at $T = 4.2\,\mathrm{K}$ was measured. Peaks of I_c corresponding to $D_F = 0.5\Lambda$ and $D_F = 2.5\Lambda$ were found. These experimental findings are consistent with our theory. Here, we have shown (see Fig. 4.12) that $L_{1,S}$ has maxima near 1.5Λ and 2.5Λ when $I = 0.1$ in the D_F range we have considered. We found another maximum at $D_F \sim 0.5\Lambda$, not included in the range shown. The penetration lengths associated with S are as important as those associated with F when discussing the triplet proximity effects because the system can open up the corresponding channels only when both of them are long ranged. We believe that no obvious peak near 1.5Λ was observed because of the layout of their symmetric system. Therefore, one can conclude that the conical magnetic structures play an important role in the triplet proximity effects. Both experiment and theory confirm that the existence of the long-range proximity effects depends on the relation between the thickness of the magnetic layers and the wavelength of their magnetic structure.

Having seen in the previous two figures that triplet amplitudes may substantially pervade even rather thick Ho layers at moderate values of τ, it is of interest to investigate the τ dependence of the proximity lengths in these nanoscale F/S systems for times roughly up to 2π in our dimensionless units. We therefore present in Fig. 4.13 the triplet proximity lengths as a function of D_F for $I = 0.5$ at different values of τ. The panel arrangement is as in the previous figure. Thus, in the top panels where we plot $L_{0,F}$ and $L_{1,F}$, we see that both of them depend only weakly on τ, in the range considered. This is in part due to the relatively thin F layers included in the plot. The triplet amplitudes vanish at $\tau = 0$ but can saturate quickly through the F region as soon as τ increases. In contrast, on the much thicker ($D_S = 150$) S side (bottom panels), both $L_{0,S}$ and $L_{1,S}$ increase with τ, as is consistent with expectation from the knowledge of previous chapter involving F/S systems with misaligned exchange fields [34]. Furthermore, the overall shape of the proximity lengths on the S side does not change with τ and only the magnitude evolves. Quite remarkably, the minima of $L_{0,S}$ and $L_{1,S}$ are very deep, and the value of these lengths at their minima is almost τ independent and nearly the same at all minima in the range plotted. The minima are separated by $\Lambda/2$. If one compares

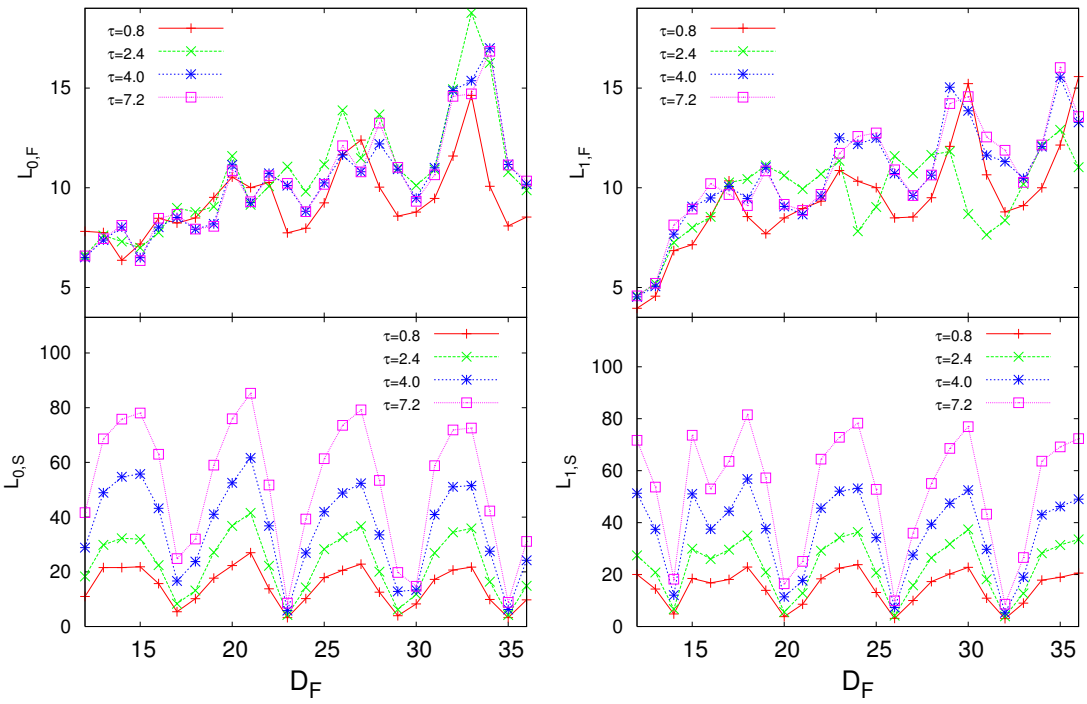

Figure 4.13: Triplet proximity lengths vs D_F for $I = 0.5$, $D_S = 150$, at different τ values. The left panels show $L_{0,F}$ and $L_{0,S}$, and the right panels show $L_{1,F}$ and $L_{1,S}$. The lines are guides to the eye.

the left and right panels, one can see that the locations of maxima in one approximately coincide with the position of minima in the other: the left and right panels are again complementary to each other as was the case with the plots in Fig. 4.12.

4.3.4 Local magnetization and LDOS

Next, we discuss other important physical quantities that are related to the proximity effects, including the local magnetization, $\boldsymbol{m}(y)$, and the the local DOS (LDOS). Considering that the ferromagnetism can drastically alter the superconductivity, one might wonder about the opposite case: how the local magnetizations behave near the F/S interface. These so-called reverse proximity effects have been studied [16, 75, 76, 77,

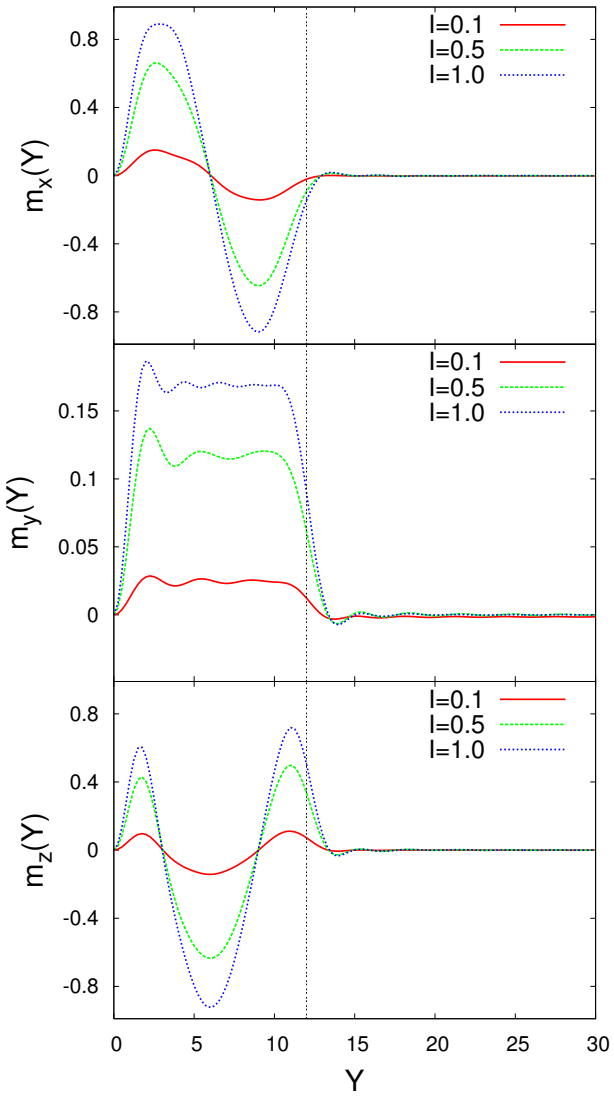

Figure 4.14: Normalized (see text) local magnetization components plotted as a function of Y for several values of I. From top to bottom, x, y, and z-components are shown. We use $D_F = \Lambda$ and $D_S = 150$ in this figure.

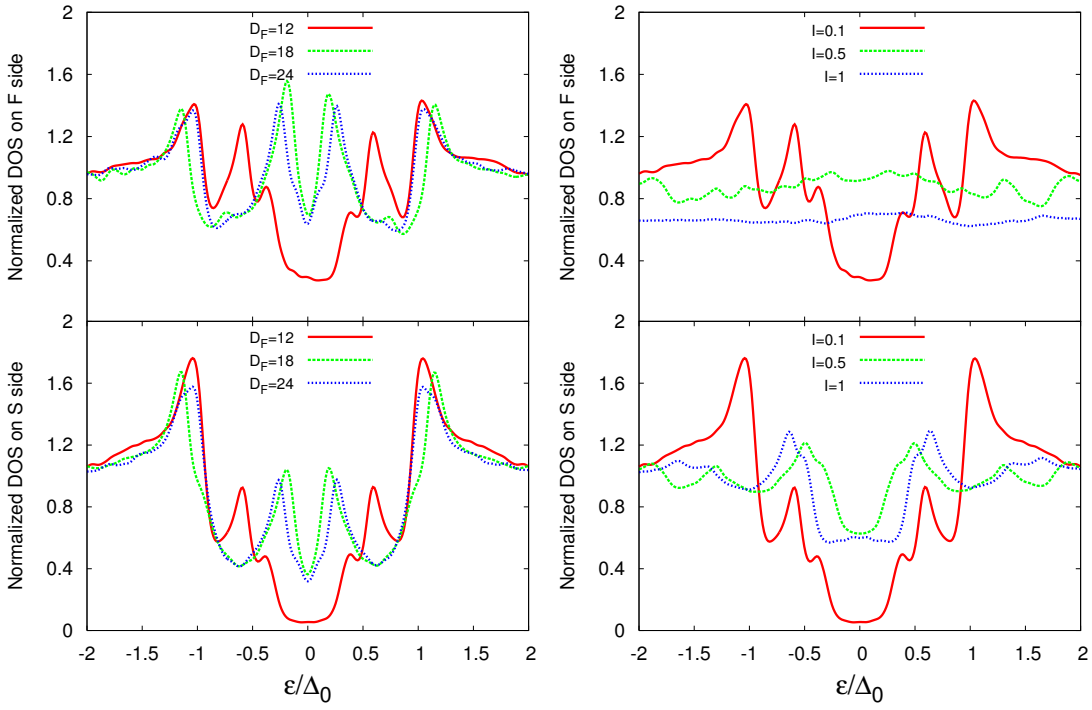

Figure 4.15: LDOS averaged over the F regions (top panels) and S regions (bottom panels), plotted vs energy. On the left panels, the integrated LDOS is shown for different D_F and $I = 0.1$. On the right panels, the integrated LDOS is shown for different I and $D_F = \Lambda$. In all cases, the superconductor width is set to $D_S = 150$.

78, 52, 90, 111, 112] for a number of multilayer F/S configurations, including F_1F_2S trilayers discussed in Chap. 2, with uniform exchange fields in each magnetic layer. Here, the space-varying exchange fields in F oscillate in the x-z plane and are constant along the y direction (see Fig. 4.1). We computed the local magnetizations using Eqs. 4.5 for $D_S = 150$, $D_F = \Lambda$ and three different values of I. The results are normalized in the usual [52, 77] manner (see the discussion of the local magnetization in Sec. 2.3) so that for a putative bulk F material with a uniform internal field characterized by the parameter I the quantity plotted would have the value $[(1+I)^{3/2}-(1-I)^{3/2}]/[(1+I)^{3/2}+(1-I)^{3/2}]$. In Fig. 4.14, each component of $\boldsymbol{m}$ is shown in a separate panel and their behavior plotted throughout the whole conical magnet region and some distance into S near the interface. Consider first the x component: the corresponding component of the internal

field (see Eq. 4.1) vanishes at the outer interface ($Y = 0$) and goes smoothly to zero at the F/S interface, which in this case is at $Y = D_F = \Lambda$. As a consequence, one can see that the m_x component undergoes a full period of oscillation in the F material. The maximum and minimum values as a function of I are numerically what they should be, given our normalization. However, as Fig. 4.14 clearly shows, the self-consistently determined m_x does not vanish at the F/S interface but instead penetrates a short distance inside S. This is a manifestation of the reverse proximity effect. For the other transverse component, m_z, the situation is more complicated. The field component h_z, out of phase with h_x, does not vanish smoothly at $Y = 0$ nor at $Y = D_F$. Therefore, the corresponding m_z component in F is squeezed, and in addition to the peak at $Y = \Lambda/2$, which has the expected location and value, there are two smaller peaks at intermediate values. At the interface between materials, penetration of this component is appreciably more considerable than for m_x. The longitudinal component m_y, which is induced by the uniform h_y component, behaves qualitatively as transverse components in uniform ferromagnet F/S structures [28]. Penetration into the S layer occurs over a relatively short distance, except at the smallest value of I where it is relatively larger, although the overall scale is of course smaller. The value of m_y in the F layer is again the expected one, consistent with our normalization.

Finally, we wish to discuss the LDOS. Here, we will present the results for the LDOS, as in Chap. 2, summed over spins, integrated over either the F or the S layer, and normalized as usual to its value in the normal state of bulk S material. The results are given in Fig. 4.15 where the energy scale of the horizontal axis is in units of the superconducting gap of bulk S material, Δ_0. The left panels of Fig. 4.15 show the LDOS integrated over the F (top) and S regions (bottom) for $D_F = \Lambda$, 1.5Λ, and 2Λ. The superconductor has a thickness $D_S = 1.5\Xi_0$, and F has a relatively weak exchange field, $I = 0.1$. For $D_F = \Lambda$, one can clearly see, for the integrated DOS in the S side, peaks near $\varepsilon/\Delta_0 = \pm 1$ as in the ordinary bulk spectrum. There is an additional subgap structure, including proximity induced bound states at smaller energies, followed by a very deep dip-nearly a minigap. Overall, the DOS structure contains traces of the familiar DOS for a pure bulk superconductor. On the F side, the integrated LDOS at this value of D_F still exhibits BCS-like peaks at $\varepsilon/\Delta_0 = \pm 1$ and a subgap dip, but the whole structure is much weaker and the depth of the dip much smaller. It is indicative

of the superconducting correlations present in the F region. In contrast, the subgap superconducting features in the integrated LDOS for larger D_F values ($D_F = 1.5\Lambda$ and 2Λ) are much less prominent, although the peaks near $\varepsilon/\Delta_0 = \pm 1$ remain. Nonetheless, there are still shallow and discernible signatures in the gap region, in both the F and S layers. For these two larger values of D_F, the results (as compared on the same side) are remarkably similar. This is surprising at first since we have already seen that $T_c(D_F)$ has, in this range of I, maxima near $D_F = \Lambda$ and $D_F = 2\Lambda$ and a local minimum at $D_F = 1.5\Lambda$, as shown in Fig. 4.3. From that, one might naively guess that the integrated LDOS for $D_F = 2\Lambda$ should behave similarly when $D_F = \Lambda$, with a different integrated LDOS for $D_F = 1.5\Lambda$. This expectation is incorrect because, as one can see on a closer inspection of Fig. 4.3, T_c at $D_F = \Lambda$ is higher than that at $D_F = 2\Lambda$, although both are near the local maxima. Furthermore, T_c at $D_F = 1.5\Lambda$ is closer to the T_c value at $D_F = 2\Lambda$ than to that at $D_F = \Lambda$. Since T_c is associated with the magnitude of the singlet pair amplitudes, in which the LDOS is indirectly correlated to, one should conclude that the LDOS corresponding to $D_F = 2\Lambda$ should be similar to $D_F = 1.5\Lambda$ rather than $D_F = \Lambda$. Indeed, the results confirm this notion.

On the right panels of Fig. 4.15, we present the integrated LDOS on both the F and the S sides for different exchange fields, $I = 0.1$, $I = 0.5$, and $I = 1.0$, at $D_F = 12 = \Lambda$. We see that when I is increased from $I = 0.1$, the integrated LDOS on the F side becomes quite flat (at the value $(1/2)[(1+I)^{1/2} + (1-I)^{1/2}]$ as per our normalization) and essentially devoid of a superconducting signature. On the S side, the integrated LDOS at $I = 0.5$ and $I = 1.0$ still retains some vestiges of the structure seen in the $I = 0.1$ case. However, the integrated LDOS at $I = 0.5$ on the S side is slightly different than that at $I = 1.0$. The dip for $I = 1.0$ is wider than for $I = 0.5$, in a way more superconducting-like. What happens is that at larger values of I the mismatch between the Fermi wavevector in S and the Fermi wavevectors in the up and down bands in F increases. This diminishes the penetration of the Cooper pairs into S and hence the overall scale of the proximity effects. We recall that the overall dimensionless scale of the proximity effect in F is roughly $\Xi_F = 1/I$. Consequently, superconductivity is impaired in S over a smaller scale when it is in contact with a stronger ferromagnet. Having said that, one might argue that at $I = 0.1$ the integrated LDOS on the S side should have a smaller dip than the other two curves for stronger I. However, we have to consider here

also the overall behavior of the T_c vs I curves at a constant D_F. This behavior is once again oscillatory but with a superimposed decay. The overall decay results in T_c being higher at $I = 0.1$ than at either $I = 0.5$ or $I = 1$, but the oscillations produce a higher value of T_c at $I = 1$ than at $I = 0.5$. This explains the progression of the curves. All the above discussion and results indicate that the LDOS can provide, if properly analyzed, another perspective and additional information on the superconducting nature of our bilayers.

4.4 Conclusions

In this chapter, we have studied several aspects of proximity effects in F/S bilayers, where the ferromagnet has a conical structure characteristic of rare earths such as Ho, by numerically solving the self-consistent BdG equations. We have calculated $T_c(D_F)$, the critical temperature as a function of magnet thickness, for different parameter values. The $T_c(D_F)$ curves exhibit a fairly intricate oscillatory behavior which is found to be related to both the strength I (as they would for a uniform magnet) and the periodicity Λ of the conical exchange fields inherent in the magnet. As is the case for F/S structures in which F is uniform, we observe reentrant behavior with D_F when I is strong enough. The physical reason behind this D_F reentrance in our bilayers is similar to that in ordinary F/S structures, but the additional periodicity associated with the magnet, which in many cases dominates the oscillations, makes the behavior more complicated. As a function of D_S, we find that $T_c(D_F)$ can also exhibit D_F reentrance even at a small I when D_S is of the order of the superconducting coherence length. The additional oscillations produced by the magnetic structure also lead to effects not found in F_1F_2S trilayers, namely pure reentrance with temperature: superconductivity occurs in a finite temperature range $T_{c1} < T < T_{c2}$. We report two examples of this reentrance at a very small D_F ($D_F \sim 0.5\Lambda$) [65] and a somewhat larger $D_F > \Lambda$, where it should be experimentally easier to realize. To elucidate the physics underlying these reentrant phenomena, we have evaluated the singlet pair amplitudes and thermodynamic functions. The competition between condensation energy and entropy is responsible for the T reentrance: the superconducting state may be, under certain circumstances, the high entropy state, leading to recovery of the normal state as T is lowered. The calculated

thermodynamic quantities are fully consistent with the $T_c(D_F)$ phase diagrams and the singlet pair amplitudes. This entropy competition driven situation is very different than other singlet superconducting T-reentrant cases associated with the field induced situations. Temperature reentrance involving magnetic order has been long known to occur in spin glasses [114], but the lowest T and high T phases (spin glass and paramagnetic, respectively) are not the same. However, the T reentrance reported in this chapter is unique: both the lowest T and highest T are in the non-superconducting ferromagnetic phase.

When a magnet has a conical structure, both the $m = 0$ and $m = \pm 1$ odd triplet components can be induced simultaneously. This, however, is not the case in uniform-magnet bilayers: at least two uniform misaligned F layers are needed to generate the $m = \pm 1$ component. We studied the odd triplet pair amplitudes in our bilayers and found them to be long-ranged in both the S and F layers. We have analyzed the time delay dependence of the odd triplet amplitudes. The results are consistent with previous work on both F_1SF_2 and F_1F_2S trilayers (see Chap 2), but the additional Λ periodicity leads to important differences. We characterized the triplet long-range behavior by introducing the appropriately defined lengths. We found that the relevant proximity length oscillates with D_F and these oscillations depend on the strength and periodicity of the exchange field. Our methods are likely appropriate for many experimental conditions, as evidenced by the consistency of our results with recent tunneling experiments [38].

We have also considered the reverse proximity effects: the influence of the superconductivity on the magnetism. We found that all three components of the local magnetization penetrate in slightly different ways into the S layer. At a larger I this is a short-range phenomenon, but it is otherwise for weak magnetism. Both m_x and m_z oscillate in the F regions to reflect the spiral exchange field. Finally, the calculated LDOS reveals important information and discernible signatures linked to the proximity effects in these bilayers and are correlated to the superconducting transition temperatures.

Chapter 5

Comparison of theory with experiment in conical-ferromagnet/superconductor bilayers

In this chapter, we compare the theoretical results on Holmium/Niobium (Nb/Ho) bilayers with experiments of our collaborators, F. Chiodi *et al* [56], in particular, the transition temperatures, T_c, as functions of Ho thicknesses. As explained in previous chapters, the singlet pair amplitude oscillates in position within the F layer and induces oscillations in the supercurrent of a SFS Josephson junction and in the critical temperature (T_c) of a F/S bilayer. In experiments, many oscillation periods have been observed in the supercurrent of SFS junctions [115, 116, 117] ; however, F/S bilayers only exhibited reentrant superconductivity followed by one oscillation and then saturation [22, 25, 118, 119, 120]. In Chap. 4, we theoretically predicted multiple T_c oscillations with d_F in F/S bilayers with F being conical-magnets. Multiple T_c oscillations with d_F are also observed experimentally in Ho/Nb systems [56] , and their comparisons with theory are reported in this chapter.

It was recently found that spin-polarized triplet Cooper pairs, in which the spins

align parallel rather than antiparallel, can be generated by coupling an s-wave superconductor to an inhomogeneous F [82, 121, 122, 123]. This striking possibility opens up a whole new field of research, in which superconductivity and ferromagnetism act cooperatively to create long-range, spin polarized, dissipation-free currents. Of most relevance to this chapter, the intrinsic conical magnetism of Ho has been shown to generate a triplet supercurrent which was able to penetrate a 16-nm-thick film of Co [38] (see also Secs. 1.2 and 4.1). The critical temperature T_c of Nb/Ho thin film bilayers are measured experimentally whilst varying the Ho layer thickness d_{Ho} in the $0.5 - 15\,\mathrm{nm}$ range. Multiple T_c vs d_{Ho} oscillations superimposed on a decaying background are observed. These cannot be simply explained within the standard singlet pairing framework, and arise from both the spin-splitting effect of the exchange field and from its inhomogeneity, responsible for the spin-polarized triplet correlations.

5.1 Samples

Holmium is a rare-earth ferromagnet, which possesses a helical magnetic structure below 133 K. At low temperatures ($T < 19\,\mathrm{K}$), Ho is a conical ferromagnet: its atomic moment of $10.34\,\mu_B$ forms an angle $\alpha = 80^\circ$ with the crystallographic c-axis, which is perpendicular to the sample plane, thus having a small constant out-of-plane component. Its in-plane component rotates along the c-axis, making a helix with an average turn angle of $\beta = 30^\circ$ (see Eq. 4.1) per atomic layer, giving a helical period of $\lambda = 3.34\,\mathrm{nm}$ (see Ref. [124]). Two series of Nb/Ho/Cu trilayer thin films were prepared (labeled here as T1 and T2) by our experimental collaborators. The Nb and Cu thicknesses were kept constant, while the Ho layer thickness was varied between samples. The T1 and T2 structures are: Nb(16)-Ho[4.4-15]-Cu(13) and Nb(15)-Ho[1.1-13]-Cu(13), where the layer thicknesses are noted in nm units in the parentheses. The Cu layer was included to prevent oxidation of the Ho.

5.2 Oscillatory transition temperatures

From Fig. 5.1, one can clearly see experimental data (blue dots) exhibit ∼4 oscillations, superimposed on a slow decay, which could correspond to the beginning of a reentrance

similar to those observed in homogeneous F/S films. Oscillations are more evident in T2 since there the Nb layer is thinner, and therefore Ho has a stronger effect, leading to smaller T_c and larger oscillation amplitudes [25]. This effect is consistent with our discussion on Fig. 4.3 in Chap. 4. There we predicted the oscillation amplitudes decrease when the aspect ratio of the S thickness to the coherence length increases.

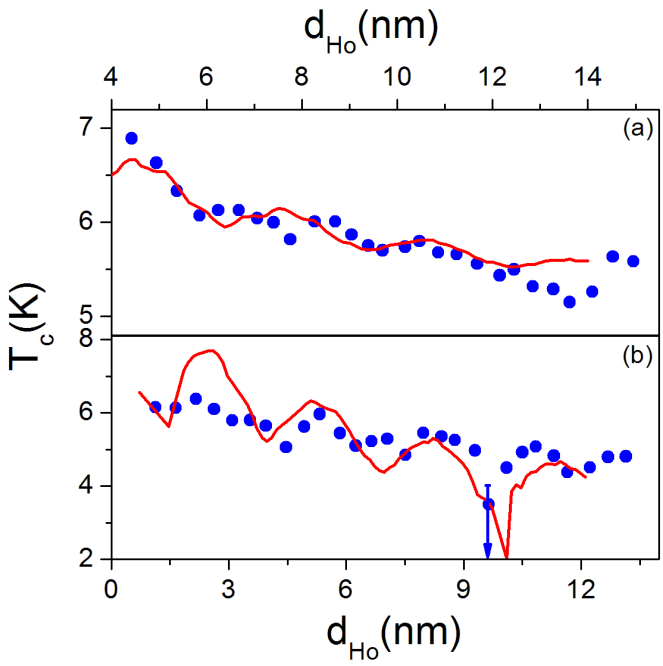

Figure 5.1: T_c vs the thickness of Ho layer, d_{Ho}, for the T1 (a) and the T2 (b) series (dots) compared to the solution of the BdG equations (lines). The theoretical curve fitting the T1 series was calculated using $\xi_{Ho} = 3.2\,\text{nm}$, $T_c^0 = 9\,\text{K}$ and an overall T_c shift of 1.4 K while the fitting of the T2 series was calculated using $\xi_{Ho} = 2.1\,\text{nm}$, $T_c^0 = 9\,\text{K}$ with an overall T_c shift of 2 K. The transition for the T2 sample with $d_{Ho} = 9.6\,\text{nm}$ (see arrow) is not complete ($T_c < 4.2\,\text{K}$); however, the beginning of the transition is visible (see text).

To compare our results with theory, we have calculated the transition temperature of Nb-Ho bilayers using a fully microscopic procedure based on the exact numerical diagonalization of the self-consistent BdG equations, as described in previous chapters [44, 65, 79]. This method can effectively handle the geometrical effects inherent

to finite systems, as well as the triplet correlations generated by the presence of the nonuniform magnetization in Ho [33, 34]. The $m = 0$ and $m = \pm 1$ triplet amplitudes are all found to be non-vanishing and similar in importance, as discussed in Chap. 4. The bilayers are theoretically modeled as being infinite in the transverse direction. The helical magnetic structure of Ho is described by a spiral local exchange field whose angle with the c-axis α, turning angle β, and helical period λ, are stated above and in the previous chapter. Whenever possible, we set the relevant parameters to their corresponding experimental values, keeping the adjustable ones to a minimum. Thus, we set the Ho and Nb layers thicknesses d_{Ho} and d_S, and the critical temperature T_c^0 of a bulk Nb sample to their measured values. In the thin Nb layer, we set the effective correlation length and the average Fermi velocity to standard values, respectively $\xi_S = 10\,\text{nm}$ and $v_S = 4.4 \times 10^5\,\text{m/s}$ [125]. The dimensionless Ho exchange field I, which determines the ferromagnetic coherence length ξ_{Ho}, is an adjusted parameter. The calculated T_c is shown in Fig. 5.1 as a function of $(d_{Ho} - d_{dl})$, to account for the measured magnetic dead layer $d_{dl} \sim 1\,\text{nm}$. We obtain the correct T_c decay, reproducing the experimental shape of T_c as a function of d_{Ho}. However, the theory data (red curves in Fig. 5.1) need to be shifted slightly up (by $\sim 1.5\,\text{K}$) to agree quantitatively with the experimental values. These shifts occur (as previously seen in [44]) due to the actual samples not quite conforming to the ideal assumptions of the theory. We find, on the other hand, that the results are very sensitive to the value of d_s, thus it is remarkable that a good agreement is found without adjusting this parameter from its experimental value. The d_{Ho} range of the T2 series is rather extensive and includes the small d_{Ho} range where the T_c oscillations are more pronounced. Of particular interest is the sharper minimum found near 10 nm. According to our theory, this is due to the near emergence of a reentrance region in d_{Ho}: the system is very close to being non-superconducting at this thickness value, as found experimentally (see arrow in Fig. 5.1). The fitted values of the parameter I used here give $\xi_{Ho} = 3.2\,\text{nm}$ for the T1 series and $\xi_{Ho} = 2.1\,\text{nm}$ for the T2 series. These are both consistent with $\xi_{Ho} \sim 5\,\text{nm}$ found experimentally [38]. Due to the ratio $\xi_{Ho}/\lambda \sim 1$, the oscillations in T_c are governed by a combination of both the helical period λ and the ferromagnetic coherence length ξ_{Ho}, leading to an overall intricate behavior. We have stressed this important point in the previous chapter

5.3 Conclusions

In agreement with the theoretical modeling of inhomogeneous F/S junctions, experiments show complex oscillations of T_c vs d_{Ho}, resulting from the contributions of both singlet and triplet Cooper pairs. The presence of a behavior which is already quasi reentrant in d_{Ho}, and which is in agreement with the theory, is particularly intriguing. In Chap. 4, our theoretical finding demonstrates that not only inhomogeneous F/S junctions can exhibit reentrance in d_{Ho} but also in T. The quasi-reentrance reported here may be a useful guidance for future researchers to look for the reentrance in T in Ho/Nb thin-film layered structures.

Chapter 6

Tunneling conductance and spin transport in clean ferromagnet/ ferromagnet/superconductor heterostructures

6.1 Introduction

Over the last two decades, significant progress in fabrication techniques has allowed the development of sputniks devices, such as spin valves [14], that utilize both charge and spin degrees of freedom. In addition to traditional spin valves that consist of magnetic materials only, researchers are also interested in superconducting spin valves, including F/S layered structures as mentioned in previous chapters, that exhibit superconducting switching effects. Their potential applications in spintronics include magnetic memory technology where information storage is accomplished via control of the magnetic moment bit. It is then crucial to have precise control over the magnetization direction. Spin transfer torque (STT) is one effect that affords such control. The generation of spin-polarized supercurrents may be used to obtain a superconducting STT acting on the magnetization of a ferromagnet. This effect may be utilized in high density nanotechnologies that require magnetic tunnel junctions. Thus, the dissipationless nature

of the supercurrent flow offers a promising avenue in terms of low energy nanoscale manipulation of superconducting and magnetic orderings.

As discussed in Chap. 1, for the F/S layered structures, consideration of Andreev reflection is central when studying their transport properties [46, 47, 48] such as their tunneling conductance. Of particular interest [45, 46, 47, 48, 126] is the behavior of the tunneling conductance in the subgap region, where hybrid systems can carry a supercurrent due to Andreev reflection. In conventional Andreev reflection, the reflected hole has opposite spin to the incident particle. Accordingly, the exchange field in the F materials that causes the splitting of spin bands has a significant effect on the tunneling conductance in the subgap region. Most important, the qualitative behavior of the conductance peak in the zero bias limit is strongly influenced by the degree of conduction electron spin polarization in the F materials [46, 47, 48, 127]. Experimentally, this concept has been applied to quantify the spin polarization [49, 50, 128, 129, 130].

An intriguing phenomenon in F/S structures is the induction of the $m = \pm 1$ long-range triplet pairing correlations [29, 30, 31, 34, 131, 132, 133] as discussed extensively in previous chapters. However, for such correlations to be induced, F/S structures must possess a spin-flip mechanism. Examples include a spin-dependent scattering potential at the F/S interface [59, 90] and the introduction of another magnetic layer with a misoriented magnetic moment such as F_1SF_2 superconducting spin valves [33] (see also Sec. 2.1). The pairing state of $m = \pm 1$ induced triplet correlations is at variance with the effects of *conventional* Andreev reflection, responsible for the generation of singlet Cooper pairs. Thus, recent studies [134, 135, 136, 137, 138] on the tunneling conductance propose the existence of *anomalous* Andreev reflection, that is, a reflected hole with the same spin as the incident particle can be Andreev reflected under the same circumstances as the generation of $m = \pm 1$ triplet pairing correlations becomes possible. In this view, triplet proximity effects are correlated with the process of this anomalous Andreev reflection. This will be confirmed and discussed in this chapter.

As discussed in Chaps. 2 and 3, a F_1F_2S trilayer is another important geometry for a superconducting spin valve. By applying an external magnetic field, or switching via STT, one is able to control the relative orientation of the intrinsic magnetic moments and investigate the dependence [53, 82, 84] of physical properties such as T_c on the misorientation angle α between the two magnetic layers. Due to the proximity effects, T_c is

often found to be minimized when the magnetizations are approximately perpendicular to each other [52] reflecting the presence of long-range triplet correlations, induced in F_1F_2S trilayers, as explained in Chaps. 2 and 3. The non-monotonic behavior of T_c as a function of α has also been shown to be quantitatively [53] related to the long-range triplet correlations with excellent agreement between theory and experiment (see Chap. 3).

Motivated by these important findings, we will investigate here, in a fully self-consistent manner, the α dependence of the tunneling conductance and other transport quantities of these F_1F_2S trilayers. Non-self-consistent theoretical studies of tunneling conductance have been performed on F_1F_2S trilayers in previous work [68, 136]. However, as we shall see in Sec. 6.2, only self-consistent methods guarantee that conservation laws are not violated and (see Sec. 6.3) only then can one correctly predict the proximity effects on the angular dependence of transport properties. The spin-polarized tunneling conductance of F/S bilayers only, was studied in Refs. [47, 48, 139, 140]. Also, in traditional spin valves e.g. F_1F_2 layered structures, the spin-polarized current generated in the F_1 layer can transfer angular momentum to the F_2 layer when their magnetic moments are not parallel to each other [14] via the effect of STT [141, 142]. As a result, the spin current is not a conserved quantity and one needs a general law that relates local spin current to local STT [138]. The transport properties of F_1SF_2 structures, in particular the dependence on applied bias of the spin transfer torque and the spin-polarized tunneling conductance have been previously studied [138, 143, 144].

Here, we consider charge transport and both spin current and spin transfer torque in F_1F_2S trilayers. In previous theoretical work, such as that mentioned above, when computing tunneling conductance of N/S and F/S structures, using methods based on the Blonder-Tinkham-Klapwijk (BTK) procedure [45, 47, 48, 126, 138, 144, 145] and quasi-classical approximations [146], the superconducting pair amplitude was assumed to be a step function: a constant in S, dropping abruptly to zero at the N/S or F/S interface and then vanishing in the non-superconducting region. This assumption neglects proximity effects. Only qualitative predictions on the behavior of the tunneling conductance can be reliably made. Still, results exhibit many interesting features especially in F/S systems [47, 48]. However, to fully account for the proximity effects, in the transport properties, one must use a self-consistent pair potential. This is because that

reveals realistic information regarding the leakage and depletion of superconductivity (see Sec. 1.2). Also, as we shall discuss below, self-consistent solutions guarantee that conservation laws are satisfied. In Ref. [54], the tunneling conductance of F/S bilayers was extracted via self-consistent solutions of BdG equations. However, the numerical methods used there required awkward fitting procedures that led to appreciable uncertainties and precluded their application to trilayers. The findings indicated that the self-consistent tunneling conductances for the bilayer are quantitatively different from those computed in a non-self-consistent framework, thus demonstrating the importance of properly accounting for proximity effects in that situation. Here we report on a powerful **self-consistent** approach and use it to compute the tunneling conductance of F_1F_2S trilayers. It is based on the BTK method, incorporated into a transfer matrix procedure similar to that used [147] in Josephson junction calculations and simple F/S junctions within a Hubbard model [148]. As we shall demonstrate, this approach not only has the advantage of being more numerically efficient but also can be used to compute spin transport quantities. Thus, we are able to address many important points regarding both charge and spin transport in F_1F_2S trilayers, including the spin currents and spin transfer torque, the proximity effects on the tunneling conductance, and the correlation between the anomalous Andreev reflection and the triplet correlations.

This chapter is organized as follows: we present our self-consistent approach, and its application to compute the tunneling conductance, the spin transfer torques, the spin current, and the proper way to ensure that conservation laws are satisfied, in Sec. 6.2. In Sec. 6.3 we present the results. In Subsec. 6.3.1, we briefly compare the results of F/S bilayers obtained in our self-consistent approach with non-self-consistent ones. The rest of Subsec. 6.3.2 includes our results for trilayers, that is, the main results of this chapter. The dependence on the tunneling conductance of F_1F_2S trilayers on the angle α is extensively discussed as a function of geometrical and material parameters. Results for the effect of the anomalous Andreev reflection, the spin transfer torque, and the spin current are also presented. We conclude this chapter with a recapitulation in Sec. 6.4.

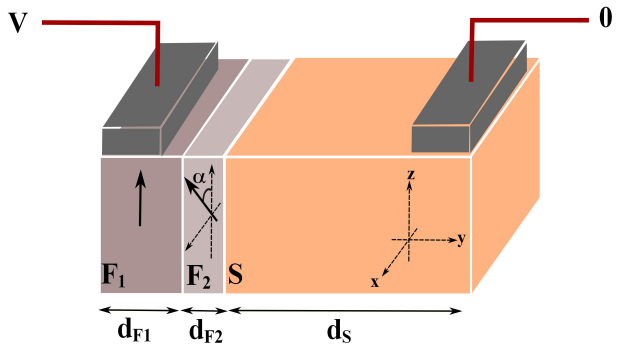

Figure 6.1: Schematic of the F_1F_2S trilayer. The exchange field, $\boldsymbol{h}$, denoted by a black solid arrow, is along the $+z$ direction in the outer magnetic layer (F_1) while within the inner magnetic layer (F_2), $\boldsymbol{h}$ is oriented at an angle α in the x-z plane. The outer magnetic layer and the superconducting layer are connected to electrodes that are biased with a finite voltage V.

6.2 Methods

6.2.1 Description of the system

The geometry of our system is depicted in Fig. 6.1. As in Chap. 2, we denote the outer ferromagnet as F_1 and the middle layer as F_2. We again choose our coordinate system so that the interfaces are parallel to the x-z plane, and infinite in extent, while the system has a finite width $d = d_{F_1} + d_{F_2} + d_S$ in the y direction. The BdG equations appropriate to our system is given in Eq. 2.1. However, to simplify mathematical expressions that follows, the exchange fields in F_1 and F_2 are redefined to be $\mathbf{h} = h_1\hat{\mathbf{z}} \equiv \mathbf{h_1}$ and $\mathbf{h} = h_2\left(\sin\alpha\hat{\mathbf{x}} + \cos\alpha\hat{\mathbf{z}}\right) \equiv \mathbf{h_2}$, respectively. To take into account the more realistic situation where the F materials can in general have different bandwidths than the S layer, we define (as in Ref. [54]) a mismatch parameter Λ (not to be confused with the spatial period defined in Chap. 4) via $E_{FM} \equiv \Lambda E_{FS}$, where E_{FM} and E_{FS} are Fermi energies for magnets and superconductors, respectively. In this chapter, we measure all energies in units of E_{FS}.

We are aiming here to solve the problem in a fully self-consistent manner. The self-consistent pair potential $\Delta(y)$ can be expressed in terms of the quasiparticle and quasihole wavefunctions by making use of the generalized Bogoliubov transformations, $\psi_\sigma = \sum_n \left(u_{n\sigma}\gamma_n + \eta_\sigma v^*_{n\sigma}\gamma^\dagger_n \right)$, where $\sigma = (\uparrow, \downarrow)$ and $\eta_\sigma \equiv 1(-1)$ for spin-down (up). Accordingly,

$$\Delta(y) = \frac{g(y)}{2} {\sum_n}' \left[u_{n\uparrow}(y) v^*_{n\downarrow}(y) + u_{n\downarrow}(y) v^*_{n\uparrow}(y) \right] \tanh\left(\frac{\epsilon_n}{2T} \right), \tag{6.1}$$

We obtain the self-consistent pair potential following the iterative numerical procedures discussed in previous chapters. Here we adopt complex conjugates for the quasihole wavefunctions in the Bogoliubov transformations to remind readers that wavefunction are required to be complex functions when studying transport properties.

6.2.2 Application of the BTK method

The BTK formalism is a procedure to extract the transmitted and reflected amplitudes, and hence the conductance, from solutions to the BdG equations. This is accomplished by writing down the appropriate eigenfunctions in different regions. In this subsection, we review the relevant aspects of the formalism [45] for the non-self-consistent case (a step function pair potential) with the objective of establishing notation and methodology to describe, in the next subsection, the procedure to be used in the self-consistent case.

Consider first a spin-up quasiparticle with energy ϵ, incident into the left side labeled "F_1", in Fig. 6.1. Since the exchange fields in the F_1 and F_2 layers can be noncollinear, it follows from Eq. 2.1 that the spin-up (-down) quasiparticle wavefunction is not just coupled to the spin-down (-up) quasihole wavefunction, as is the case of F/S bilayers. Indeed, the wavefunction in the F_1 layer is a linear combination of the original incident spin-up quasiparticle wavefunctions and various types of reflected wavefunctions, namely reflected spin-up and spin-down quasiparticle and quasihole wavefunctions (via both ordinary and Andreev reflections). We use a single column vector notation to represent these combinations,

$$\Psi_{F1,\uparrow} \equiv \begin{pmatrix} e^{ik^+_{\uparrow 1} y} + b_\uparrow e^{-ik^+_{\uparrow 1} y} \\ b_\downarrow e^{-ik^+_{\downarrow 1} y} \\ a_\uparrow e^{ik^-_{\uparrow 1} y} \\ a_\downarrow e^{ik^-_{\downarrow 1} y} \end{pmatrix} . \tag{6.2}$$

If the incident particle has spin down, the corresponding wavefunction in F_1 is

$$\Psi_{F1,\downarrow} \equiv \begin{pmatrix} b_\uparrow e^{-ik^+_{\uparrow 1}y} \\ e^{ik^+_{\downarrow 1}y} + b_\downarrow e^{-ik^+_{\downarrow 1}y} \\ a_\uparrow e^{ik^-_{\uparrow 1}y} \\ a_\downarrow e^{ik^-_{\downarrow 1}y} \end{pmatrix} \quad . \tag{6.3}$$

In these expressions $k^\pm_{\sigma 1}$ are quasiparticle (+) and quasihole (−) wavevectors in the longitudinal direction y, and satisfy the relation,

$$k^\pm_{\sigma m} = \left[\Lambda(1-\eta_\sigma I_m) \pm \epsilon - k^2_\perp\right]^{1/2}, \tag{6.4}$$

where $m = 1$ (as used above) or $m = 2$, used later, and the dimensionless exchange field is defined as usual, $I_m \equiv h_m/E_{FM}$. As mentioned above, all energies are in units of E_{FS} and, in addition, we measure all momenta in units of k_{FS}. In this simple case, one can easily distinguish the physical meaning of each individual wavefunction. For instance in Eq. 6.2, $a_\downarrow (0,0,0,1)^T e^{ik^-_{\downarrow 1}y}$ is the reflected spin-down quasihole wavefunction. The quasihole wavefunctions are the time reversed solutions of the BdG equations and carry a positive sign in the exponent for a left-going wavefunction. The relevant angles can be easily found in terms of wavevector components. Thus, e.g., the incident angle θ_i (for spin-up) at the F_1F_2 interface is $\theta_i = \tan^{-1}\left(k_\perp/k^+_{\uparrow 1}\right)$, and the Andreev reflected angle $\theta^-_{r\downarrow}$ for reflected spin-down quasihole wavefunction is $\theta^-_{r\downarrow} = \tan^{-1}\left(k_\perp/k^-_{\downarrow 1}\right)$. The conservation of transverse momentum leads to many important features [47, 54] when one evaluates the angularly averaged tunneling conductance, as we will see below. For the intermediate layer F_2, the eigenfunction in general contains both left- and right-moving plane waves, that is,

$$\Psi_{F2} \equiv \begin{pmatrix} c_1 f^+_\uparrow e^{ik^+_{\uparrow 2}y} + c_2 f^+_\uparrow e^{-ik^+_{\uparrow 2}y} + c_3 g^+_\uparrow e^{ik^+_{\downarrow 2}y} + c_4 g^+_\uparrow e^{-ik^+_{\downarrow 2}y} \\ c_1 f^+_\downarrow e^{ik^+_{\uparrow 2}y} + c_2 f^+_\downarrow e^{-ik^+_{\uparrow 2}y} + c_3 g^+_\downarrow e^{ik^+_{\downarrow 2}y} + c_4 g^+_\downarrow e^{-ik^+_{\downarrow 2}y} \\ c_5 f^-_\uparrow e^{ik^-_{\uparrow 2}y} + c_6 f^-_\uparrow e^{-ik^-_{\uparrow 2}y} + c_7 g^-_\uparrow e^{ik^-_{\downarrow 2}y} + c_8 g^-_\uparrow e^{-ik^-_{\downarrow 2}y} \\ c_5 f^-_\downarrow e^{ik^-_{\uparrow 2}y} + c_6 f^-_\downarrow e^{-ik^-_{\uparrow 2}y} + c_7 g^-_\downarrow e^{ik^-_{\downarrow 2}y} + c_8 g^-_\downarrow e^{-ik^-_{\downarrow 2}y} \end{pmatrix}, \tag{6.5}$$

where $k^\pm_{\uparrow 2}$ and $k^\pm_{\downarrow 2}$ are defined in Eq. 6.4. The $\pm$ indices are defined as previously, and the up and down arrows refer to F_1. The eigenspinors f and g that correspond to spin parallel or antiparallel to $\mathbf{h_2}$ respectively, are given, for $0 \le \alpha \le \pi/2$, by the expression,

$$\begin{pmatrix} f_\uparrow^+ \\ f_\downarrow^+ \end{pmatrix} = \frac{1}{\mathcal{N}} \begin{pmatrix} 1 \\ \frac{1-\cos\alpha}{\sin\alpha} \end{pmatrix} = \begin{pmatrix} f_\uparrow^- \\ -f_\downarrow^- \end{pmatrix}; \quad \begin{pmatrix} g_\uparrow^+ \\ g_\downarrow^+ \end{pmatrix} = \frac{1}{\mathcal{N}} \begin{pmatrix} -\frac{\sin\alpha}{1+\cos\alpha} \\ 1 \end{pmatrix} = \begin{pmatrix} -g_\uparrow^- \\ g_\downarrow^- \end{pmatrix} \tag{6.6}$$

with the normalization constant $\mathcal{N} = \sqrt{2/1+\cos\alpha}$. These spinors reduce to those for pure spin-up and spin-down quasiparticles and holes when $\alpha = 0$, corresponding to a uniform magnetization along z. One can also easily see that the particular wavefunction of Eq. 6.5, $c_1 \left(f_\uparrow^+, f_\downarrow^+, 0, 0\right)^T e^{ik_{\uparrow 2}^+ y}$ denotes a quasiparticle with spin parallel to the exchange field in F_2. When $\pi/2 < \alpha \leq \pi$, these eigenspinors read

$$\begin{pmatrix} f_\uparrow^+ \\ f_\downarrow^+ \end{pmatrix} = \frac{1}{\mathcal{N}} \begin{pmatrix} \frac{\sin\alpha}{1-\cos\alpha} \\ 1 \end{pmatrix} = \begin{pmatrix} -f_\uparrow^- \\ f_\downarrow^- \end{pmatrix}; \quad \begin{pmatrix} g_\uparrow^+ \\ g_\downarrow^+ \end{pmatrix} = \frac{1}{\mathcal{N}} \begin{pmatrix} 1 \\ -\frac{1+\cos\alpha}{\sin\alpha} \end{pmatrix} = \begin{pmatrix} g_\uparrow^- \\ -g_\downarrow^- \end{pmatrix} \tag{6.7}$$

with $\mathcal{N} = \sqrt{2/1-\cos\alpha}$.

In this subsection where we are still assuming a non-self-consistent stepwise potential equal to Δ_0 throughout the S region and to zero elsewhere, we have the superconducting coherence factors, $\sqrt{2}u_0 = \left[\left(\epsilon + \sqrt{\epsilon^2 - \Delta_0^2}\right)/\epsilon\right]^{1/2}$ and $\sqrt{2}v_0 = \left[\left(\epsilon - \sqrt{\epsilon^2 - \Delta_0^2}\right)/\epsilon\right]^{1/2}$. In this case the right-going eigenfunctions on the S side can be written as,

$$\Psi_S \equiv \begin{pmatrix} t_1 u_0 e^{ik^+ y} + t_4 v_0 e^{-ik^- y} \\ t_2 u_0 e^{ik^+ y} + t_3 v_0 e^{-ik^- y} \\ t_2 v_0 e^{ik^+ y} + t_3 u_0 e^{-ik^- y} \\ t_1 v_0 e^{ik^+ y} + t_4 u_0 e^{-ik^- y} \end{pmatrix}, \tag{6.8}$$

where, $k^\pm = \left[1 \pm \sqrt{\epsilon^2 - \Delta_0^2} - k_\perp^2\right]^{1/2}$ are quasiparticle (+) and quasihole (-) wavevectors in the S region. By using continuity of the four-component wavefunctions and their first derivatives at both interfaces, one can obtain all sixteen unknown coefficients in the above expressions for the wavefunctions by solving a set of linear equations of the form $\mathcal{M}_{F1} x_{F1,\sigma} = \mathcal{M}_{F2} x_{F2}$ at the F_1F_2 interface and $\tilde{\mathcal{M}}_{F2} x_{F2} = \mathcal{M}_S x_S$ at the F_2S interface simultaneously, where

$$x_{F1,\uparrow}^T = (1, b_\uparrow, 0, b_\downarrow, 0, a_\uparrow, 0, a_\downarrow) \tag{6.9a}$$

$$x_{F1,\downarrow}^T = (0, b_\uparrow, 1, b_\downarrow, 0, a_\uparrow, 0, a_\downarrow) \tag{6.9b}$$

$$x_{F2}^T = (c_1, c_2, c_3, c_4, c_5, c_6, c_7, c_8) \tag{6.9c}$$

$$x_S^T = (t_1, 0, t_2, 0, t_3, 0, t_4, 0)\,, \tag{6.9d}$$

and $\mathcal{M}_{F1}$, $\mathcal{M}_{F2}$, $\tilde{\mathcal{M}}_{F2}$, and $\mathcal{M}_S$ are appropriate 8×8 matrices, which are straightforward to write down (see App. A). Use of these coefficients gives us all the reflected and transmitted amplitudes a_σ and b_σ which are used to compute the conductance, as discussed in the next two subsections.

6.2.3 Transfer matrix self-consistent method

The non-self-consistent step potential assumption is largely unrealistic. Proximity effects lead to a complicated oscillatory behavior of the superconducting order parameter in the F layers and to the generation [13, 33, 34, 131, 132, 133, 134, 149] of triplet pairs as discussed in Sec. 6.1. The concomitant depletion of the pair amplitudes near the F/S interface means that unless the superconductor is thick enough, the pair amplitude does not saturate to its bulk value even deep inside the S regions. Furthermore, as we shall emphasize below, lack of self-consistency may lead to violation of charge conservation: hence, while non-self-consistent approximations might be sometimes adequate for equilibrium calculations, their use must be eschewed for transport. Therefore, one should generally use a self-consistent pair potential that is allowed to spatially vary, as required by Eq. 6.1, and hence results in a minimum in the free energy of the system.

We begin by extending the BTK formalism to the spatially varying self-consistent pair potential obtained as explained below Eq. 6.1. Although the self-consistent solutions of the BdG equations reveal that the pair amplitudes are non-zero in the non-superconducting regions due to the proximity effects, the pair potential vanishes in these regions since $g(y) \equiv 0$ there. Therefore, one can still use Eqs. 6.2 and 6.3, with 6.5, for the wavefunctions in the F_1 and F_2 regions. To deal with the spatially varying pair potential on the S side, we divide it into many very thin layers with microscopic thicknesses of order k_{FS}^{-1}. We treat each layer as a very thin superconductor with a constant pair potential, Δ_i, as obtained from the self-consistent procedure. We are then able to write the eigenfunctions of each superconducting layer corresponding to that value of the pair potential. For example, in the i-th layer, the eigenfunction should contain all

left and right going solutions, and it reads:

$$\Psi_{Si} \equiv \begin{pmatrix} t_{1i}u_i e^{ik_i^+ y} + \bar{t}_{1i}u_i e^{-ik_i^+ y} + t_{4i}v_i e^{-ik_i^- y} + \bar{t}_{4i}v_i e^{ik_i^- y} \\ t_{2i}u_i e^{ik_i^+ y} + \bar{t}_{2i}u_i e^{-ik_i^+ y} + t_{3i}v_i e^{-ik_i^- y} + \bar{t}_{3i}v_i e^{ik_i^- y} \\ t_{2i}v_i e^{ik_i^+ y} + \bar{t}_{2i}v_i e^{-ik_i^+ y} + t_{3i}u_i e^{-ik_i^- y} + \bar{t}_{3i}u_i e^{ik_i^- y} \\ t_{1i}v_i e^{ik_i^+ y} + \bar{t}_{1i}v_i e^{-ik_i^+ y} + t_{4i}u_i e^{-ik_i^- y} + \bar{t}_{4i}v_i e^{ik_i^- y} \end{pmatrix}, \tag{6.10}$$

where, $k_i^{\pm} = \left[1 \pm \sqrt{\epsilon^2 - \Delta_i^2} - k_\perp^2\right]^{1/2}$, and Δ_i represents the strength of the normalized self-consistent pair potential in the i-th superconducting layer. The superconducting coherence factors u_i and v_i depend on Δ_i in the standard way. All the coefficients in Eq. 6.10 are unknown, and remain to be determined. However, in the outermost S layer (rightmost in our convention) the eigenfunctions are of a form identical to Eq. 6.8 but with different locally constant pair potential.

We see then that the price one has to pay for including the proximity effects is the need to compute a very large number of coefficients. To do so, we adopt here a transfer matrix method to solve for these unknowns [147]. If one considers the interface between the i-th and the $(i+1)$-th layer, we have the linear relation $\tilde{\mathcal{M}}_i x_i = \mathcal{M}_{i+1} x_{i+1}$, where, for a generic i,

$$x_i^T = (t_{1i}, \bar{t}_{1i}, t_{2i}, \bar{t}_{2i}, t_{3i}, \bar{t}_{3i}, t_{4i}, \bar{t}_{4i})\,, \tag{6.11}$$

and the matrices, $\tilde{\mathcal{M}}_i$ and $\mathcal{M}_{i+1}$, can be written as discussed in connection with Eq. 6.9. The coefficients in the $(i+1)$-th layer can be obtained in terms of those in the i-th layer as $x_{i+1} = \mathcal{M}_{i+1}^{-1}\tilde{\mathcal{M}}_i x_i$. In the same way, for the interface between the $(i-1)$-th layer and the i-th layer, we can write $x_i = \mathcal{M}_i^{-1}\tilde{\mathcal{M}}_{i-1}x_{i-1}$. From the above relations, one can write down the relation between x_{i+1} and x_{i-1}, i.e. $x_{i+1} = \mathcal{M}_{i+1}^{-1}\tilde{\mathcal{M}}_i\mathcal{M}_i^{-1}\tilde{\mathcal{M}}_{i-1}x_{i-1}$. By iteration of this procedure, one can "transfer" the coefficients layer by layer and eventually relate the coefficients of the rightmost layer, x_n, to those of the leftmost layer in S and then on to the inner ferromagnetic layer F_2:

$$x_n = \mathcal{M}_n^{-1}\tilde{\mathcal{M}}_{n-1}\mathcal{M}_{n-1}^{-1}\cdots\tilde{\mathcal{M}}_1\mathcal{M}_1^{-1}\tilde{\mathcal{M}}_{F2}x_{F2} \tag{6.12}$$

By solving Eq. 6.12 together with $\mathcal{M}_{F1}x_{F1} = \mathcal{M}_{F2}x_{F2}$, we obtain all the coefficients in the F_1 region, where the wavefunction is *formally* still described by the expressions given in Eqs. 6.2 and 6.3. Of course, all coefficients involved, including the energy dependent

a_σ and b_σ values from which (see below) the conductance is extracted, are quite different from those in a non-self-consistent calculation. These differences will be reflected in our results. One can also prove that, when the pair potential in S is a constant (non-self-consistent), then $\mathcal{M}_{i+1} = \tilde{\mathcal{M}}_i$ and therefore Eq. 6.12 becomes $x_n = x_1 = \mathcal{M}_1^{-1}\tilde{\mathcal{M}}_{F2}x_{F2}$. This is formally identical to that we have seen in our discussion of the non-self-consistent formalism.

This efficient technique, besides allowing us to determine all the reflected and transmitted amplitudes in the outermost layers, permits us to perform a consistency check by recomputing the self-consistent solutions to the BdG equations (the eigenfunctions). Once we have determined the amplitudes x_{F1}, x_{F2}, and x_n, we can use them to find the amplitudes in any intermediate layer by "transferring" back the solutions. For example, the coefficients x_{n-1} can be found by using $x_n = \mathcal{M}_n^{-1}\tilde{\mathcal{M}}_{n-1}x_{n-1}$ if we know the coefficient x_n for the rightmost layer. Knowledge of these coefficients in every region yields again the self-consistent wavefunctions of the system. These of course should be the same as the eigenfunctions found in the original procedure. Although the numerical computations involved in this consistency check are rather intensive, it is worthwhile to perform them: we have verified that, by plugging these solutions into Eq. 6.1 and considering all possible solutions with all possible incident angles to the BdG equations, the output pair potential obtained from the transport calculation is the same as the input pair potential obtained by direct diagonalization. This would obviously not have been the case if the initial pair potential had not been fully self-consistent to begin with. The reflected and transmitted amplitudes calculated from the self-consistent solutions are in general very different from the non-self-consistent ones and lead to different quantitative behavior of the tunneling conductance, as we shall discuss in section 6.3.

6.2.4 Charge conservation

We discuss now the important issue of the charge conservation laws. In transport calculations, it is fundamental to assure that they are not violated [150]. From the Heisenberg equation

$$\frac{\partial}{\partial t}\langle\rho(\mathbf{r})\rangle = i\langle[\mathcal{H}_{eff}, \rho(\mathbf{r})]\rangle\,. \tag{6.13}$$

By computing the above commutator, we arrive at the following continuity condition

$$\frac{\partial}{\partial t}\left\langle \rho(\mathbf{r})\right\rangle + \nabla\cdot\mathbf{j} = -4e\mathrm{Im}\left[\Delta(\mathbf{r})\left\langle \psi_{\uparrow}^{\dagger}(\mathbf{r})\psi_{\downarrow}^{\dagger}(\mathbf{r})\right\rangle\right]. \tag{6.14}$$

In the steady state, which is all that we are considering here, the first term on the left is omitted. Equation 6.14 is then simply an expression for the divergence of the current. In our quasi-one-dimensional system, and in terms of our wavefunctions, the conservation law can be rewritten as:

$$\frac{\partial j_y(y)}{\partial y} = 2e\mathrm{Im}\left\{\Delta(y)\sum_n \left[u_{n\uparrow}^{*}v_{n\downarrow} + u_{n\downarrow}^{*}v_{n\uparrow}\right]\tanh\left(\frac{\epsilon_n}{2T}\right)\right\} \tag{6.15}$$

When the system is in equilibrium the self-consistency condition on the pair potential causes the right hand side of Eqs. 6.14 or 6.15 to vanish. This would **not** necessarily be the case if a non-self-consistent [151] solution were used [152]. It was shown that charge conservation is only guaranteed when self-consistency is adhered to in microscopic Josephson junctions [153]. Current-voltage calculations for N/S heterostructures show that self-consistency is crucial to properly account for all of the Andreev scattering channels arising when the current is constant throughout the system [154]. While non-self-consistent solutions are less computationally demanding, their validity when calculating transport quantities in the nonequilibrium regime is always suspect.

In the problem we are considering, there exists a finite voltage bias V between the two leads of the system (see Fig. 6.1). This finite bias leads to a non-equilibrium quasiparticle distribution and results of course in a net current. Still, charge conservation must hold. To see how this works in this non-equilibrium case we first write down the net quasiparticle charge density in the $T \to 0$ limit (the case we consider in this chapter) by considering the excited state $|\mathbf{k_1}\mathbf{k_2}\cdots\rangle$ caused by the finite bias V. Thus, this excited state contains all single particle states $|\mathbf{k_j}\rangle$ $(j = 1, 2, \cdots)$ with energies less than eV. For simplicity, let us first consider the contribution by a single-particle state. We use $|\mathbf{k}\rangle$ to characterize this single particle state with an incident wavevector $\mathbf{k} = \mathbf{k}_{\perp} + k\hat{\mathbf{y}}$

and energy $\epsilon_{\mathbf{k}}$. The charge density associated with it is written as

$$\begin{aligned}
\rho &= -e\sum_{\sigma}\left\langle \mathbf{k}\left|\psi_{\sigma}^{\dagger}\psi_{\sigma}\right|\mathbf{k}\right\rangle \qquad (6.16)\\
&= -e\sum_{n\sigma}\left(|u_{n\sigma}|^{2}\left\langle \mathbf{k}\left|\gamma_{n}^{\dagger}\gamma_{n}\right|\mathbf{k}\right\rangle + |v_{n\sigma}|^{2}\left\langle \mathbf{k}\left|\gamma_{n}\gamma_{n}^{\dagger}\right|\mathbf{k}\right\rangle\right)\\
&= -e\sum_{n\sigma}\left(|u_{n\sigma}|^{2}\left\langle \mathbf{k}\left|\gamma_{n}^{\dagger}\gamma_{n}\right|\mathbf{k}\right\rangle + |v_{n\sigma}|^{2}\left\langle \mathbf{k}\left|1-\gamma_{n}^{\dagger}\gamma_{n}\right|\mathbf{k}\right\rangle\right)\\
&= -e\sum_{n\sigma}|v_{n\sigma}|^{2} - e\sum_{n\sigma}\left(|u_{n\sigma}|^{2}-|v_{n\sigma}|^{2}\right)\delta_{n\mathbf{k}}\\
&= -e\sum_{n\sigma}|v_{n\sigma}|^{2} - e\sum_{\sigma}\left(|u_{\mathbf{k}\sigma}|^{2}-|v_{\mathbf{k}\sigma}|^{2}\right)
\end{aligned}$$

The first term represents the ground state charge density. For a generic excited state, $|\mathbf{k_1}\mathbf{k_2}\cdots\rangle$, that can contain many single-particle states, one need to sum over all single-particle states for the charge density such that

$$\rho = -e\sum_{n\sigma}|v_{n\sigma}|^{2} - e\sum_{\epsilon_{\mathbf{k}}<eV}\sum_{\sigma}\left(|u_{\mathbf{k}\sigma}|^{2}-|v_{\mathbf{k}\sigma}|^{2}\right). \qquad (6.17)$$

The quasiparticle current density from this generic excited state can also be computed,

$$\begin{aligned}
j_{y} &= -\frac{e}{2m}\sum_{\epsilon_{\mathbf{k}}<eV}\sum_{\sigma}\left\langle -i\psi_{\sigma}^{\dagger}\frac{\partial}{\partial y}\psi_{\sigma} + i\left(\frac{\partial}{\partial y}\psi_{\sigma}^{\dagger}\right)\psi_{\sigma}\right\rangle_{\mathbf{k}} \qquad (6.18)\\
&= -\frac{e}{m}\mathrm{Im}\left[\sum_{n\sigma}v_{n\sigma}\frac{\partial v_{n\sigma}^{*}}{\partial y} + \sum_{\epsilon_{\mathbf{k}}<eV}\sum_{\sigma}\left(u_{\mathbf{k}\sigma}^{*}\frac{\partial u_{\mathbf{k}\sigma}}{\partial y} + v_{\mathbf{k}\sigma}^{*}\frac{\partial v_{\mathbf{k}\sigma}}{\partial y}\right)\right]\\
&= -\frac{e}{m}\mathrm{Im}\left[\sum_{\epsilon_{\mathbf{k}}<eV}\sum_{\sigma}\left(u_{\mathbf{k}\sigma}^{*}\frac{\partial u_{\mathbf{k}\sigma}}{\partial y} + v_{\mathbf{k}\sigma}^{*}\frac{\partial v_{\mathbf{k}\sigma}}{\partial y}\right)\right],
\end{aligned}$$

where $\langle ...\rangle_{\mathbf{k}}$ is a shorthand notation of $\langle\mathbf{k}|...|\mathbf{k}\rangle$. The first term in the second line vanishes because it represents the net current for the system in the ground state with a real pair potential. The right hand side of the continuity equation, Eq. 6.15, becomes $-4e\mathrm{Im}\left[\Delta\sum_{\epsilon_{\mathbf{k}}<eV}\left(u_{\mathbf{k}\uparrow}^{*}v_{\mathbf{k}\downarrow}+v_{\mathbf{k}\uparrow}u_{\mathbf{k}\downarrow}^{*}\right)\right]$ and is responsible for the interchange between the quasiparticle current density and the supercurrent density [45]. We have numerically verified that by properly including these terms, all of our numerical results for the current density are constant throughout the whole system.

6.2.5 Extraction of the conductance

We are now in a position to compute the differential tunneling conductances. We begin by discussing the extraction of the conductance from the BTK theory. As we mentioned in the previous subsection, the finite bias V and the resulting non-equilibrium distribution leads to an electric current flowing in the junction. In the BTK theory, this current can be evaluated from the following [45] expression,

$$I(V) = \int G(\epsilon) \left[f\left(\epsilon - eV\right) - f\left(\epsilon\right) \right] d\epsilon, \tag{6.19}$$

where f is the Fermi function. The energy dependent tunneling conductance, $G(\epsilon) = \partial I/\partial V|_{V=\epsilon}$ in the low-T limit, is given as:

$$\begin{aligned} G(\epsilon, \theta_i) &= \sum_\sigma P_\sigma G_\sigma(\epsilon, \theta_i) \\ &= \sum_\sigma P_\sigma \left(1 + \frac{k^-_{\uparrow 1}}{k^+_{\sigma 1}} |a_\uparrow|^2 + \frac{k^-_{\downarrow 1}}{k^+_{\sigma 1}} |a_\downarrow|^2 - \frac{k^+_{\uparrow 1}}{k^+_{\sigma 1}} |b_\uparrow|^2 - \frac{k^+_{\downarrow 1}}{k^+_{\sigma 1}} |b_\downarrow|^2 \right), \end{aligned} \tag{6.20}$$

where we have used, as is customary, natural units of conductance (e^2/h). In the above expression the different k components are as explained in subsection 6.2.2 (see e.g. Eq. 6.4) and the a_σ and b_σ are as defined in Eqs. 6.2 and 6.3. These coefficients, which are of course energy dependent, are calculated using the self-consistent transfer matrix technique of subsection 6.2.3. Therefore, even though Eq. 6.20 is formally the same in the self-consistent and non-self-consistent cases, the results for the reflection amplitudes or probabilities involved, $|a_\uparrow|^2$, $|a_\downarrow|^2$, $|b_\uparrow|^2$, and $|b_\downarrow|^2$ are different in these two schemes. The angle θ_i is the incident angle, discussed in terms of $\mathbf{k}$ components below Eq. 6.4. The weight factor $P_\sigma \equiv \left(1 - h_1 \eta_\sigma\right)/2$ accounts for the number of available states for spin-up and spin-down bands in the outer electrode. The tunneling conductance can also be interpreted as the transmission coefficient for electrical current. The method enables us also to compute the current density directly from the wavefunctions, Eqs. 6.2 and 6.3, in the F_1 layer by using Eq. 6.18 and we have been able to verify that the resulting current density is identical to the terms inside the bracket in the expression of $G(\epsilon)$, Eq. 6.20. In other words, in the low-T limit the continuum-limit version of Eq. 6.18 is equivalent to Eq. 6.19.

The conductance results Eq. 6.20 also depend on the incident angle of electrons,

θ_i. Experimentally, one can measure the forward conductance, $\theta_i = 0$, via point contacts or, in most other experimental conditions, an angular average. Consequently, it is worthwhile to compute the angularly averaged conductance by using the following definitions,

$$\langle G_\sigma(\epsilon)\rangle = \frac{\int_0^{\theta_{c\sigma}} d\theta_i \cos\theta_i G_\sigma(\epsilon,\theta_i)}{\int_0^{\theta_{c\sigma}} d\theta_i \cos\theta_i}, \tag{6.21}$$

and

$$\langle G\rangle = \sum_\sigma P_\sigma \langle G_\sigma\rangle, \tag{6.22}$$

where the critical angle $\theta_{c\sigma}$ is in general different for spin-up and spin-down bands. This critical angle arises from the conservation of transverse momentum and the corresponding Snell's law:

$$\begin{aligned}&\sqrt{\left({k^+_{\sigma 1}}^2 + k_\perp^2\right)}\sin\theta_i = \sqrt{\left({k^+_{\sigma' 1}}^2 + k_\perp^2\right)}\sin\theta^+_{r\sigma'} \\ &= \sqrt{\left({k^-_{\sigma' 1}}^2 + k_\perp^2\right)}\sin\theta^-_{r\sigma'} = \sin\theta_S,\end{aligned} \tag{6.23}$$

where we continue to measure wavevectors in units of k_{FS}. The angles $\theta^\pm_{r\sigma}$ satisfy $\tan^{-1}\left(k_\perp/k^\pm_{\sigma 1}\right)$, and the σ and σ' are each $\uparrow$ or $\downarrow$. The last equality in Eq. 6.23 represents the case of the transmitted wave in S, and θ_S is the transmitted angle. Although the self-consistent pair potential varies in S and so do the quasiparticle (hole) wavevectors, we here need only consider the transmitted angle θ_S in the rightmost layer: this follows in the same way as the usual Snell's law in a layered system, as given in elementary textbooks. From Eq. 6.23, one can determine the critical angles for different channels. Consider, e.g., a spin-up electron incident from F_1 without any Fermi wavevector mismatch, i.e. $\Lambda = 1$. Since we are only concerned with the case that the bias of tunneling junctions is of the order of superconducting gap and therefore much smaller than the Fermi energy, the approximate magnitude of the incident wavevector is $\sqrt{1+I_1}$, the Andreev approximation. We substitute this and similar expressions into Eq. 6.23 and, with the help of Eq. 6.4, we obtain

$$\sqrt{1+I_1}\sin\theta_i = \sqrt{1-I_1}\sin\theta^-_{r\downarrow} = \sin\theta_S. \tag{6.24}$$

One can straightforwardly verify that, when the relation $\theta_i > \sin^{-1}\left(\sqrt{\frac{1-I_1}{1+I_1}}\right)$ is satisfied for the incident angle, the conventional Andreev reflection becomes an evanescent

wave [48]. In this case, the conventional Andreev reflection does not contribute to the angular averaging. On the other hand, if the energy ϵ of the incident electron is less than the saturated value of the superconducting pair amplitude in S, all the contribution to the conductance from the transmitted waves in S also vanishes because $k^{\pm}$ acquires an imaginary part. However, even the condition that ϵ is greater than the saturated superconducting amplitude does not guarantee that the contribution from the transmitted waves to the conductance is non-vanishing. One still needs to consider the transmitted critical angle $\sin^{-1}\left(\sqrt{\frac{1}{1+I_1}}\right)$. We define the critical angle $\theta_{c\sigma}$ to be the largest one among all the reflected and transmitted critical angles. It is obvious that the critical angles $\theta_{c\sigma}$ are different for spin-up and spin-down bands when $I_1 \neq 0$.

6.2.6 Spin transport

We consider now the spin transfer torque and the spin current. As the charge carriers that flow through our system, along the y direction in our convention, are spin polarized, the STT provides an additional probe of the spin degree of freedom. Unlike the charge current, that must be a constant throughout the system, the spin current density is generally not a conserved quantity in the ferromagnet regions as we will demonstrate below. The discussion in Sec. 6.2.4 on how the BTK formalism deals with the charge current can be extended to compute these spin dependent transport quantities. We need here the continuity equation for the local magnetization $\mathbf{m} \equiv -\mu_B \sum_\sigma \left\langle \psi_\sigma^\dagger \boldsymbol{\sigma} \psi_\sigma \right\rangle$, where μ_B is the Bohr magneton. By using the Heisenberg equation $\frac{\partial}{\partial t}\langle \mathbf{m}(\mathbf{r})\rangle = i\langle [\mathcal{H}_{eff}, \mathbf{m}(\mathbf{r})]\rangle$ we obtain the relation:

$$\frac{\partial}{\partial t}\langle m_i\rangle + \frac{\partial}{\partial y} S_i = \tau_i, \quad i = x, y, z \tag{6.25}$$

where $\boldsymbol{\tau}$ is the spin transfer torque, $\boldsymbol{\tau} \equiv 2\mathbf{m} \times \mathbf{h}$, and the spin current density S_i is given by

$$S_i \equiv \frac{i\mu_B}{2m} \sum_\sigma \left\langle \psi_\sigma^\dagger \sigma_i \frac{\partial \psi_\sigma}{\partial y} - \frac{\partial \psi_\sigma^\dagger}{\partial y} \sigma_i \psi_\sigma \right\rangle . \tag{6.26}$$

The spin current density reduces from a tensor form to a vector because of the quasi-one-dimensional nature of our geometry. From Eq. 6.25, we can see that $\mathbf{S}$ is a local physical quantity and $\boldsymbol{\tau}$ is responsible for the change of local magnetizations due to the flow of spin-polarized currents. As we shall see in Sec. 6.3, the conservation law (with

the source torque term) for the spin density is fundamental and one has to check it is not violated when studying these transport quantities.

In the low-T limit and with the presence of a finite bias, the non-equilibrium local magnetizations $m_i \equiv \sum_{\epsilon_{\mathbf{k}}<eV}\sum_{\sigma} -\mu_B\langle\psi^{\dagger}_{\sigma}\sigma_i\psi_{\sigma}\rangle_{\mathbf{k}}$ in Eq. 6.25 reads

$$\begin{aligned} m_x =& -\mu_B\left[\sum_n\left(-v_{n\uparrow}v^*_{n\downarrow}-v_{n\downarrow}v^*_{n\uparrow}\right)\right. \qquad (6.27a)\\ &\left.+\sum_{\epsilon_{\mathbf{k}}<eV}\left(u^*_{\mathbf{k}\uparrow}u_{\mathbf{k}\downarrow}+v_{\mathbf{k}\uparrow}v^*_{\mathbf{k}\downarrow}+u^*_{\mathbf{k}\downarrow}u_{\mathbf{k}\uparrow}+v_{\mathbf{k}\downarrow}v^*_{\mathbf{k}\uparrow}\right)\right]\\ m_y =& -\mu_B\left[i\sum_n\left(v_{n\uparrow}v^*_{n\downarrow}-v_{n\downarrow}v^*_{n\uparrow}\right)\right. \qquad (6.27b)\\ &\left.-i\sum_{\epsilon_{\mathbf{k}}<eV}\left(u^*_{\mathbf{k}\uparrow}u_{\mathbf{k}\downarrow}+v_{\mathbf{k}\uparrow}v^*_{\mathbf{k}\downarrow}-u^*_{\mathbf{k}\downarrow}u_{\mathbf{k}\uparrow}-v_{\mathbf{k}\downarrow}v^*_{\mathbf{k}\uparrow}\right)\right]\\ m_z =& -\mu_B\left[\sum_n\left(|v_{n\uparrow}|^2-|v_{n\downarrow}|^2\right)\right. \qquad (6.27c)\\ &\left.+\sum_{\epsilon_{\mathbf{k}}<eV}\left(|u_{\mathbf{k}\uparrow}|^2-|v_{\mathbf{k}\uparrow}|^2-|u_{\mathbf{k}\downarrow}|^2+|v_{\mathbf{k}\downarrow}|^2\right)\right], \end{aligned}$$

where the first summations in the expressions for m_i denote the ground state local magnetizations. The second summations appear as a consequence of the finite bias between electrodes. The expressions for the corresponding spin currents,

$$S_i \equiv \frac{i\mu_B}{2m}\sum_{\epsilon_{\mathbf{k}}<eV}\sum_{\sigma}\left\langle\psi^{\dagger}_{\sigma}\sigma_i\frac{\partial\psi_{\sigma}}{\partial y}-\frac{\partial\psi^{\dagger}_{\sigma}}{\partial y}\sigma_i\psi_{\sigma}\right\rangle_{\mathbf{k}}, \qquad (6.28)$$

becomes

$$S_x = \frac{-\mu_B}{m}\mathrm{Im}\left[\sum_n\left(-v_{n\uparrow}\frac{\partial v^*_{n\downarrow}}{\partial y} - v_{n\downarrow}\frac{\partial v^*_{n\uparrow}}{\partial y}\right)\right. \tag{6.29a}$$
$$\left. + \sum_{\epsilon_{\mathbf{k}}<eV}\left(u^*_{\mathbf{k}\uparrow}\frac{\partial u_{\mathbf{k}\downarrow}}{\partial y} + v_{\mathbf{k}\uparrow}\frac{\partial v^*_{\mathbf{k}\downarrow}}{\partial y} + u^*_{\mathbf{k}\downarrow}\frac{\partial u_{\mathbf{k}\uparrow}}{\partial y} + v_{\mathbf{k}\downarrow}\frac{\partial v^*_{\mathbf{k}\uparrow}}{\partial y}\right)\right]$$
$$S_y = \frac{\mu_B}{m}\mathrm{Re}\left[\sum_n\left(-v_{n\uparrow}\frac{\partial v^*_{n\downarrow}}{\partial y} + v_{n\downarrow}\frac{\partial v^*_{n\uparrow}}{\partial y}\right)\right. \tag{6.29b}$$
$$\left. + \sum_{\epsilon_{\mathbf{k}}<eV}\left(u^*_{\mathbf{k}\uparrow}\frac{\partial u_{\mathbf{k}\downarrow}}{\partial y} + v_{\mathbf{k}\uparrow}\frac{\partial v^*_{\mathbf{k}\downarrow}}{\partial y} - u^*_{\mathbf{k}\downarrow}\frac{\partial u_{\mathbf{k}\uparrow}}{\partial y} - v_{\mathbf{k}\downarrow}\frac{\partial v^*_{\mathbf{k}\uparrow}}{\partial y}\right)\right]$$
$$S_z = \frac{-\mu_B}{m}\mathrm{Im}\left[\sum_n\left(v_{n\uparrow}\frac{\partial v^*_{n\uparrow}}{\partial y} - v_{n\downarrow}\frac{\partial v^*_{n\downarrow}}{\partial y}\right)\right. \tag{6.29c}$$
$$\left. + \sum_{\epsilon_{\mathbf{k}}<eV}\left(u^*_{\mathbf{k}\uparrow}\frac{\partial u_{\mathbf{k}\uparrow}}{\partial y} - v_{\mathbf{k}\uparrow}\frac{\partial v^*_{\mathbf{k}\uparrow}}{\partial y} - u^*_{\mathbf{k}\downarrow}\frac{\partial u_{\mathbf{k}\downarrow}}{\partial y} + v_{\mathbf{k}\downarrow}\frac{\partial v^*_{\mathbf{k}\downarrow}}{\partial y}\right)\right].$$

The first summations in Eq. 6.29 represent the static spin current densities when there is no bias. The static spin current does not need to vanish, since a static spin transfer torque may exist near the boundary of two magnets with misaligned exchange fields. The finite bias leads to a non-equilibrium quasiparticle distribution for the system and results in non-static spin current densities that are represented by the second summation in Eq. 6.29. Obviously, the spin transfer torque has to vanish in the superconductor where the exchange field is zero. As mentioned in Sec. 2.3, it is conventional to normalize $\mathbf{m}$ to [33] $-\mu_B(N_\uparrow + N_\downarrow)$, where the number densities $N_\uparrow = k_{FS}^3(1+I_m)^{3/2}/(6\pi^2)$ and $N_\downarrow = k_{FS}^3(1-I_m)^{3/2}/(6\pi^2)$. Following this convention, we normalize $\boldsymbol{\tau}$ to $-\mu_B(N_\uparrow + N_\downarrow)E_{FS}$ and $\mathbf{S}$ to $-\mu_B(N_\uparrow + N_\downarrow)E_{FS}/k_{FS}$.

6.3 Results

The forward scattering conductances G are computed by considering a particle incident with an angle $\theta_i \cong 0$ (normal incidence). Angular averaging has been discussed in the text above Eq. 6.21. The bias energy $E \equiv eV$ is in units of the zero temperature gap, Δ_0, in bulk S material and e^2/h is used as the natural unit of conductance. When the

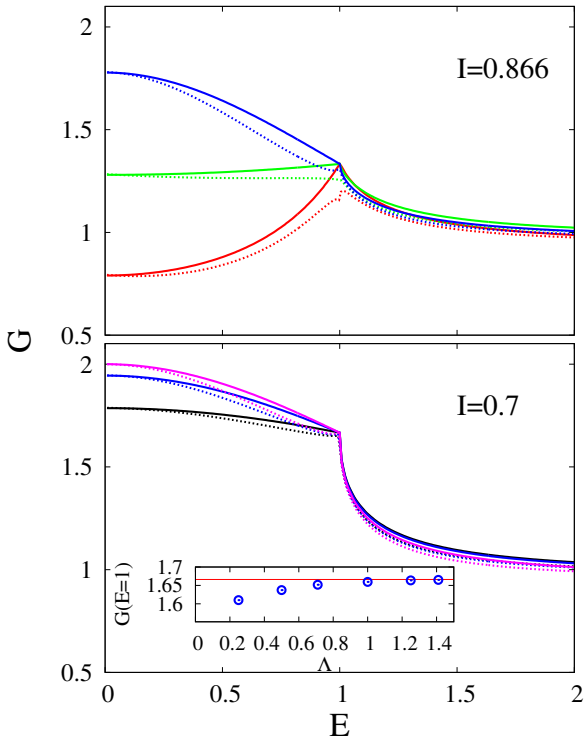

Figure 6.2: Bias dependence of the results for the forward conductance, G, in thick F/S bilayers (see text). The values of I are indicated. In both main panels the solid and dashed curves show G, in units of e^2/h for non-self-consistent and self-consistent results, respectively. The bias E is in units of the S bulk gap Δ_0. In the top panel the (red) lower curves are for a mismatch parameter $\Lambda = 0.25$, (green) the middle curves for $\Lambda = 0.5$, and the (blue) higher curves for $\Lambda = 1$. In the bottom panel, the (purple) top curves are for $\Lambda = 1.41$, the (blue) curves are as in the top panel, and the (black) lower ones for $\Lambda = 0.71$. The inset (see text) shows $G(E = 1)$ vs Λ in the self-consistent calculation (dots) and the non-self-consistent result (line).

F_1 and F_2 regions are made of same F material, i.e., $I_1 = I_2$ and $k^{\pm}_{\uparrow 1,(\downarrow 1)} = k^{\pm}_{\uparrow 2,(\downarrow)2}$, we will use I (the same convention as Chap. 2) and $k^{\pm}_{\uparrow,(\downarrow)}$ to denote their exchange fields and wavevectors. This is the case we will mostly study. All results are for the low-T limit. As in Chap. 2, all of the lengths are measured in unit of k_{FS}^{-1} and denoted by capital letters.

6.3.1 Bilayers

We begin with a brief discussion of self-consistent results for the tunneling conductance in F/S bilayers, contrasting them with non-self-consistent results. We assume that the S layer is very thick so that the pair amplitude saturates to its bulk value deep inside the S region. In this subsection, the dimensionless superconducting coherence length Ξ_0 is taken to be 50 and the thicknesses D_F and D_S of the F and S layers are both $15\Xi_0$. By computing the pair amplitudes via the direct diagonalization method [34], we have verified that they indeed saturate to their bulk value with this large ratio of D_S to Ξ_0.

As discussed in Sec. 6.1, the replacement of nonmagnetic metals with ferromagnets in a bilayer leads to strong suppression of the Andreev reflection in the subgap region. The decrease of the zero bias conductance (ZBC) strongly depends on the magnitude of the exchange field in F. This dependence is used to measure the degree of spin-polarization of magnetic materials experimentally [49, 50]. However, in early theoretical work [47, 48], it was shown that to accurately determine the degree of spin-polarization, one has to consider the Fermi wavevector mismatch (FWM), Λ, as well as the interfacial barriers. The ZBC peak is very sensitive to both spin-polarization and FWM and the dependence cannot be characterized by a single parameter.

We display in Fig. 6.2 forward conductance vs bias results for both the self-consistent and non-self-consistent calculations, at two different values of the exchange fields and several FWM values. One sees at once that the self-consistent results approach the non-self-consistent ones in the zero bias limit, while deviating the most for energies near the superconducting gap. The ZBC decreases with increasing I and with decreasing Λ. Also, larger I indeed leads to a conspicuous reduction in the subgap conductance and so does the introduction of FWM. One can conclude that the behavior of the ZBC can not be characterized by only one parameter, either I or Λ. Instead, one should expand the fitting parameter space to determine the degree of spin polarization.

In the non-self-consistent framework, the conductance at the superconducting gap ($E = 1$ in our units) is independent of Λ at a given I. However, earlier work [54] predicted that this conclusion is invalid in self-consistent approach, and that the conductance at the superconducting gap varies monotonically with increasing Λ. Here we verify this via our self-consistent transfer matrix method. The inset in the bottom panel of Fig. 6.2 clearly shows this dependence on Λ. Figure 6.2 also shows that the self-consistent results (dashed curves) on subgap conductances are in general lower than those obtained in the non-self-consistent framework (solid curves) for a strong exchange field. On the other hand, in the high bias limit, the self-consistent results become similar to the non-self-consistent ones. This is simply because the particle does not experience much of a difference between a step-like pair potential and a smooth pair potential when it is incident with high enough energy. Finally, clear cusps appear at the superconducting gap value in some cases, e.g., the forward scattering conductance curve at $I = 0.866$ and $\Lambda = 1$. This is consistent with what is found in previous work [54] for thick bilayers.

6.3.2 Trilayers

We now discuss our results for F_1F_2S trilayers of finite widths. First, we discuss the dependence of the tunneling conductances on the angle α between $\mathbf{h}_1$ and $\mathbf{h}_2$ (see Fig. 6.1). An important reason for considering trilayers with finite widths is the strong dependence of the superconducting transition temperatures T_c on the angle α due to proximity effects [52] and induced long-range triplet correlations [51]. Field induced switching effects [66] also make these structures attractive candidates for memory elements. The non-monotonic behavior of $T_c(\alpha)$ with its minimum being near $\alpha = 90°$, was extensively discussed in Chap. 2 and 3. This angular dependence has been shown to be related to the induced triplet pairing correlations [53]. The superconducting transition temperatures are also predicted to be positively correlated with the singlet pair amplitudes deep inside the S regions [52]. Therefore, it is of particular importance to consider systems of finite size to take into view the whole picture of proximity effects on the angular dependence of the tunneling conductance. For the results shown in this subsection, we assume the absence of FWM ($\Lambda = 1$).

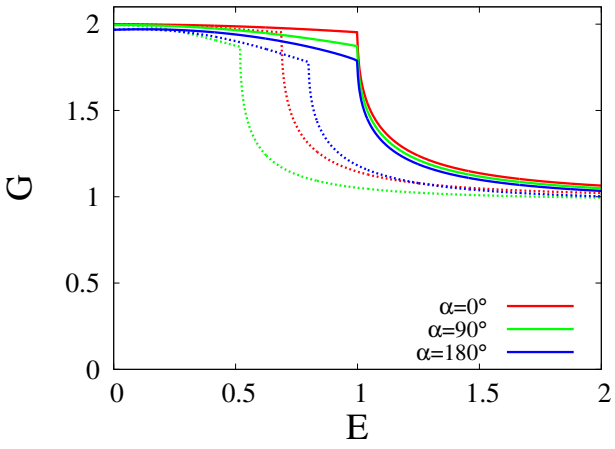

Figure 6.3: Comparison between the self-consistent and non-self-consistent forward scattering conductances of F_1F_2S trilayers. The solid and the dashed lines are for non-self-consistent and self-consistent results respectively. The (red) curves, highest at the critical bias (CB) are for $\alpha = 0°$. The (blue) curves, lowest at CB, are for $\alpha = 180°$. We have $D_{F1} = 10$, $D_{F2} = 12$, and $D_S = 180$ (see text).

Forward Scattering

As a typical example of our results, we show in Fig. 6.3 results for the α dependence of the forward scattering conductances. The exchange field we use here for both F layers is $I = 0.3$, and the thicknesses of the F_1 and F_2 layers correspond to $D_{F1} = 10$ and $D_{F2} = 12$ respectively, while the S layer has width $D_S = 180 = 1.5\Xi_0$. Results obtained via the non-self-consistent approach are plotted for comparison. In the non-self-consistent framework where the single parameter Δ_0 describes the stepwise pair potential, one sees in Fig. 6.3 that for all values of the angle α the conductance curves drop when the bias is at Δ_0, corresponding to $E = 1$ in our units. In contrast, for the self-consistent results, one can clearly see in Fig. 6.3, that the drop in the conductance curves occurs at different bias values for different angles. We also see that this critical bias (which we will denote by CB) depends on α non-monotonically, with $\alpha = 180°$ corresponding to the largest and $\alpha = 90°$ to the smallest bias values. Since the CB depends on the strength of the superconducting gap deep inside the S regions, the non-monotonicity of the CB in Fig. 6.3 is correlated with the non-monotonicity of T_c. The CB never reaches unity, in these trilayers, due to their finite size. Accordingly, this feature

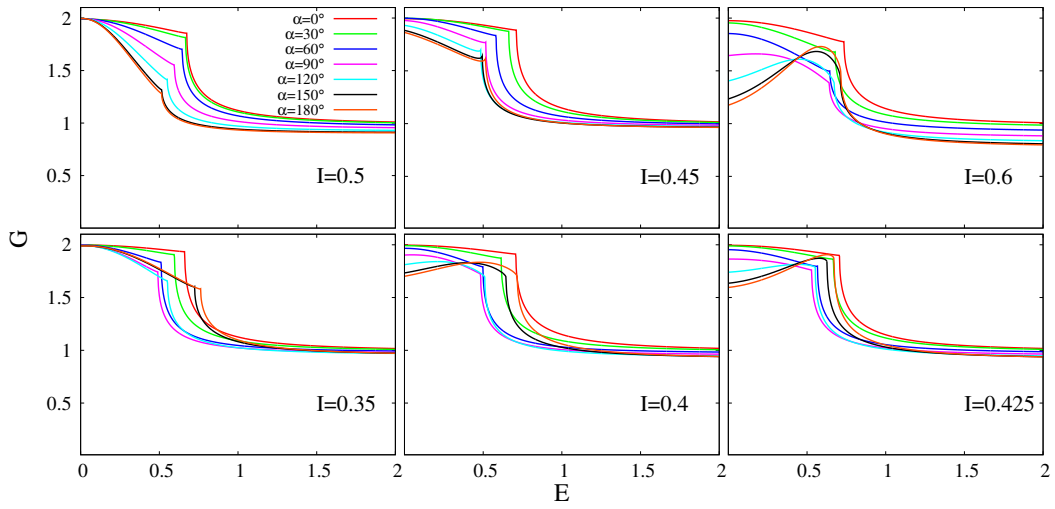

Figure 6.4: Forward scattering conductance of F_1F_2S trilayers for several angles α as indicated in the legend. The top panels are for $D_{F1} = 10$, $D_{F2} = 12$, and $D_S = 180$ and the bottom panels for $D_{F1} = 10$, $D_{F2} = 18$, and $D_S = 180$. The exchange field strength I is indicated. For the left panels, the conductances at CB decrease with increasing α. For the other panels, the ZBC (see text) decreases as α increases.

of the correct self-consistent results implies that one cannot adequately determine the angular dependence of the forward conductance in the non-self-consistent framework. This feature also provides experimentalists with another way to measure the strength of the superconducting gap for different angles in these trilayers by determining the CB in a set of conductance curves. The remaining results shown in this section are all computed self-consistently.

In Fig. 6.4, we present more results for the dependence of the forward scattering conductances on α. In the top panels the thicknesses of each layer and the coherence length are the same as Fig. 6.3. In the bottom panels we increase the thickness of the inner magnetic layer to $D_{F2} = 18$ while D_{F1}, D_S, and Ξ_0 remain unchanged. For each row of Fig. 6.4, results for three different exchange fields are plotted. In the top left panel ($I = 0.5$) we see that the angular dependence of the CB (or the magnitude of the saturated pair amplitudes) is monotonic with α. Although this monotonicity is not common, we have verified that it is consistent with the theoretical results for $T_c(\alpha)$ for the same particular case. The more usual non-monotonic dependence is found in

all other panels, as discussed in the previous paragraph. In every case, we have also checked that the magnitude of the CB reflects the magnitude of the self-consistent pair amplitudes deep inside the superconductor.

For the ZBC, we see that the degree of its angular dependence is very sensitive to I. In the top left panel, with $I = 0.5$, the ZBC is nearly independent on α. On the other hand, the ZBC in the top right panel, $I = 0.6$, drops by almost a factor of two as α varies from the relative parallel (P) orientation, $\alpha = 0^\circ$, to the antiparallel (AP) orientation, $\alpha = 180^\circ$. This is a consequence of interference between the spin-up and spin-down wavefunctions under the influence of the rotated exchange field in the middle layer. In the top left panel, we see that the conductance at CB decreases with increasing angle. In other words, the zero bias conductance peak (ZBCP) becomes more prominent as α is increased. However, for the top middle panel, $I = 0.45$, the development of the ZBCP is less noticeable when the angle α is increased. In the top right panel, $I = 0.6$, the ZBCP evolves into a zero bias conductance dip (ZBCD) as α varies from $\alpha = 0^\circ$ to $\alpha = 180^\circ$, with a clear finite bias conductance peak (FBCP) appearing just below the CB. This behavior is reminiscent [48] of that which occurs when a barrier, or mismatch, are present. In the bottom panels of this figure, corresponding to a larger value of D_{F2} one can observe similar features. For example, a slight change from $I = 0.35$ to $I = 0.4$ causes by itself a very large change in the behavior of the ZBC. Moreover, the evolution of the ZBCP to a ZBCD accompanies the occurrence of a FBCP when $\alpha > 90^\circ$. The location of the FBCP also moves closer to the CB value when α increases. That these features of the ZBC depend on both the strength of exchange field (reflected in $k_\uparrow^\pm$ and $k_\downarrow^\pm$) and the thickness of the F_2 layer indicates that the ZBC shows the characteristics of a resonance scattering phenomenon as in an elementary quantum mechanical barrier. The main difference is that the scattering problem here involves the intricate interference between quasiparticle and quasihole spinors.

When the bias is high enough, the tunneling conductance approaches its normal state value. Thus, one can extract the magnetoresistance from the conductance at $E = 2$. We only discuss here the magnetoresistance's qualitative behavior. One can define a measure of the magnetoresistance as,

$$M_G(E, \alpha) \equiv \frac{G(E, \alpha = 0^\circ) - G(E, \alpha)}{G(E, \alpha = 0^\circ)}. \tag{6.30}$$

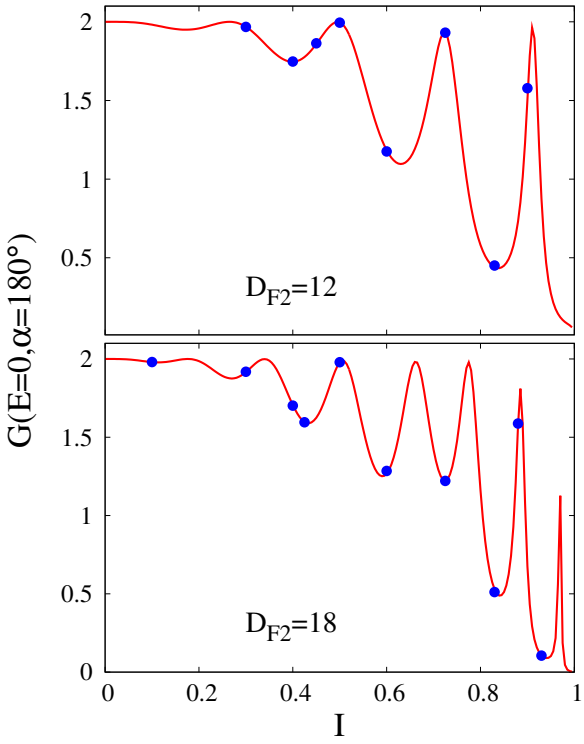

Figure 6.5: Resonance effects in the forward scattering conductance at zero bias for trilayers at $\alpha = 180°$. In the top panel, the trilayers have same thicknesses as in the top panels of Fig. 6.4, and in the bottom panel, they are as in the bottom panels of Fig. 6.4. The (blue) dots are the results from our computations and the (red) curves from Eq. 6.31.

For all results shown in the panels of Fig. 6.4, the conductance at $E = 2$ decreases with increasing α, i.e., it is a monotonic function of α, the standard behavior for conventional, non-superconducting, spin valves. Furthermore, one can also see that $M_G(E = 2, \alpha = 180°)$ increases with exchange field. Therefore, the behavior of the magnetoresistance at large bias is as one would expect in the present self-consistent BTK framework. However, the behavior of $M_G(E = 0, \alpha = 180°)$ that is associated with the behavior of the ZBC is generally a non-monotonic function of I.

We next investigate the high sensitivity of the ZBC to I by examining its resonances for two different F widths arranged in an AP magnetic configuration ($\alpha = 180°$). To do

so, we performed an analytic calculation of the ZBC in the non-self-consistent framework in situations where (as discussed in connection with Fig. 6.3) the results nearly coincide with those of self-consistent calculations. We find that the ZBC at $\alpha = 180°$, $G(E = 0, \alpha = 180°) \equiv G_{ZB}$, for a given I and D_{F2} is:

$$G_{ZB} = \frac{32 k_{\uparrow}^3 k_{\downarrow}^3}{A + 2\left(I^4 - 2I^2 - 2I^2 k_{\uparrow} k_{\downarrow}\right) \cos\left[2\left(k_{\uparrow} - k_{\downarrow}\right) D_{F2}\right]}. \tag{6.31}$$

The expression for A in Eq. 6.31 is:

$$a_1 \sin^2\left[\left(k_{\uparrow} + k_{\downarrow}\right) D_{F2}\right] + a_2\left[\cos\left(2k_{\uparrow} D_{F2}\right) - \cos\left(2k_{\downarrow} D_{F2}\right)\right] + a_3, \tag{6.32}$$

where $a_1 = 4I^2(1 - k_{\uparrow}k_{\downarrow})^2$, $a_2 = 4I^3$, and $a_3 = I^4 + (-2 + I^2 - 2k_{\uparrow}k_{\downarrow})^2$. Here we have omitted the $\pm$ indices for the quasiparticle and quasihole wavevectors, since we are in the zero bias limit. In Fig. 6.5, we plot Eq. 6.31 as a function of I for $D_{F2} = 12$ (top panel) and 18 (bottom panel). In this zero bias limit, the (blue) circles (self-consistent numerical results) are on top of the (red) curves (analytic results). As the thickness of the intermediate layer increases, the number of resonance maxima and minima increases. Therefore, the resonance behavior of the ZBC is more sensitive to I for larger D_{F2}, as we have seen in Fig. 6.4. For a given D_{F2}, the ZBC drops considerably as α varies from $\alpha = 0°$ to $\alpha = 180°$ when I is near the minimum of the resonance curve (rightmost panels of Fig. 6.4). On the other hand, when I is near the resonance maximum (leftmost panels of Fig. 6.4), the ZBC is a very weak function of α provided that I is not too strong. By examining the denominator of Eq. 6.31, we find that the terms involved in A are less important than the last term. This is because the wavelength $(k_{\uparrow} - k_{\downarrow})^{-1}$ associated with that term is the dominant characteristic wavelength in the theory of proximity effects in F/S structures [15, 58]. In both panels of Fig. 6.5, we see that the ZBC for $\alpha = 180°$ vanishes in the half-metallic limit. To show this analytically, one can use the conservation of probability currents and write down the relation, valid when the bias is smaller than the superconducting gap:

$$\frac{k_{\uparrow 1}^-}{k_{\sigma 1}^+}|a_{\uparrow}|^2 + \frac{k_{\downarrow 1}^-}{k_{\sigma 1}^+}|a_{\downarrow}|^2 + \frac{k_{\uparrow 1}^+}{k_{\sigma 1}^+}|b_{\uparrow}|^2 + \frac{k_{\downarrow 1}^+}{k_{\sigma 1}^+}|b_{\downarrow}|^2 = 1. \tag{6.33}$$

By combining Eq. 6.33 with Eq. 6.20, it becomes clear that the subgap conductances arise largely from Andreev reflection. In the half-metallic limit, conventional Andreev

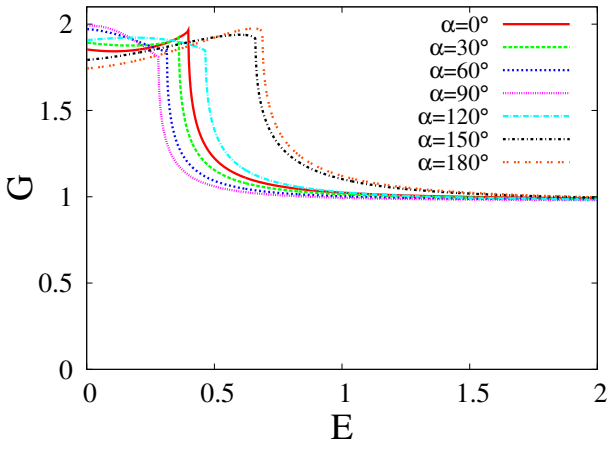

Figure 6.6: Forward scattering conductance of a F_1F_2S trilayer with differing magnetic materials corresponding to exchange fields of $I_1 = 0.6$ and $I_2 = 0.1$. Various magnetic orientations, α, are considered as shown. Geometry and other parameters are as in the top panels of Fig. 6.4.

reflection is forbidden due to the absence of an opposite-spin band: this leads to zero ZBC at $\alpha = 180°$. Same-spin Andreev reflection (see discussion in the paragraph above Eq. 6.2) is not allowed in collinear magnetic configurations. Equation 6.33 also reflects another important feature of the ZBC: the contributions to G at zero bias from the spin-up and down channels are identical except for the weight factor P_σ: one can prove analytically that the sum of first two terms (related to Andreev reflection) in Eq. 6.33 is spin-independent. As a result, the sum of last two terms, related to ordinary reflection, is also spin-independent, and so is the ZBC.

We briefly consider here one example where the two F materials in the trilayers have different field strengths. In this example all the thicknesses and the coherence length are as in the top panels of Fig. 6.4. In Fig. 6.6, we plot the forward scattering conductance for several α at $I_1 = 0.6$ and $I_2 = 0.1$. One can quickly identify that the ZBC here is a non-monotonic function of α with it maximum at the orthogonal relative magnetization angle, $\alpha = 90°$. In contrast, results at equal exchange field strengths usually demonstrate monotonic behavior, as previously shown. However, many features are still the same, such as the formation of a FBCP when $\alpha > 90°$. For $\alpha = 0°$ and $\alpha = 30°$, the conductance curves are not monotonically decreasing, as was the

case at $I_1 = I_2$. There, when $I_1 = I_2$ and $\alpha < 90°$, we always see monotonically decreasing behavior because the scattering effect due to misoriented magnetizations is not as great as at $\alpha > 90°$. Also, when $I_1 \neq I_2$, we have to include in our considerations another scattering effect that comes from the mismatch between $k^{\pm}_{\uparrow 1,(\downarrow 1)}$ and $k^{\pm}_{\uparrow 2,(\downarrow 2)}$. Specifically, when $\alpha = 0°$, the only important scattering effect is that due to mismatch from $I_1 \neq I_2$ and it leads to suppression of the ZBC at $\alpha = 0°$. However, we see that the scattering due to the misoriented magnetic configuration ($\alpha \neq 0°$) compensates the effect of mismatch from $I_1 \neq I_2$ and ZBC is maximized when $\alpha = 90°$. Qualitatively, one can examine Eqs. (6.6) and (6.7) and verify that the spinor at $\alpha = 90°$ is composed of both pure spin-up and spin-down spinors with equal weight, apart from phase factors. As a result, the scattering effect due to mismatch from $k^{\pm}_{\uparrow 1,(\downarrow 1)}$ and $k^{\pm}_{\uparrow 2,(\downarrow 2)}$ is reduced. We also verified that, when the strength of I_2 is increased towards I_1, the locations for the maximum of the ZBC(α) curves gradually move from $\alpha = 90°$ at $I_2 = 0.1$ to $\alpha = 0°$ at $I_2 = 0.6$.

Angularly averaged conductance

We now present results for the angularly averaged conductance, $\langle G \rangle$ as defined in Eq. 6.21. The details of the angular averaging are explained under Eq. 6.23. The angularly averaged conductance is relevant to a much wider range of experimental results than the forward conductance, which is relevant strictly only for some point contact experiments. This is particularly true if one recalls that the critical angle $\theta_{c\sigma}$ and the weight factor for angular averaging in Eq. 6.21 used in this work can be modified based on a real experimental set-up or on the geometry of the junction.

In Fig. 6.7, we present results for $\langle G \rangle$ at $D_{F2} = 12$ (left panels) and $D_{F2} = 18$ (right panels). All curves are obtained with $D_{F1} = 10$ and $D_S = 180 = 1.5\Xi_0$ at the values of I indicated in each panel. Results are plotted over the entire range of α values. The CB values obtained for $\langle G \rangle$ are again non-monotonic functions of α and the non-monotonicity matches that of the saturated pair amplitudes, for the reasons previously given. The CB values for $\langle G \rangle$ in these cases are the same as those for the forward scattering conductance. One can also see that the resonance phenomenon is washed out in the angularly averaged conductance. For example, the resonance curve in the top panel of Fig. 6.5 tells us that $I \approx 0.3$ and $I \approx 0.6$ correspond respectively to a

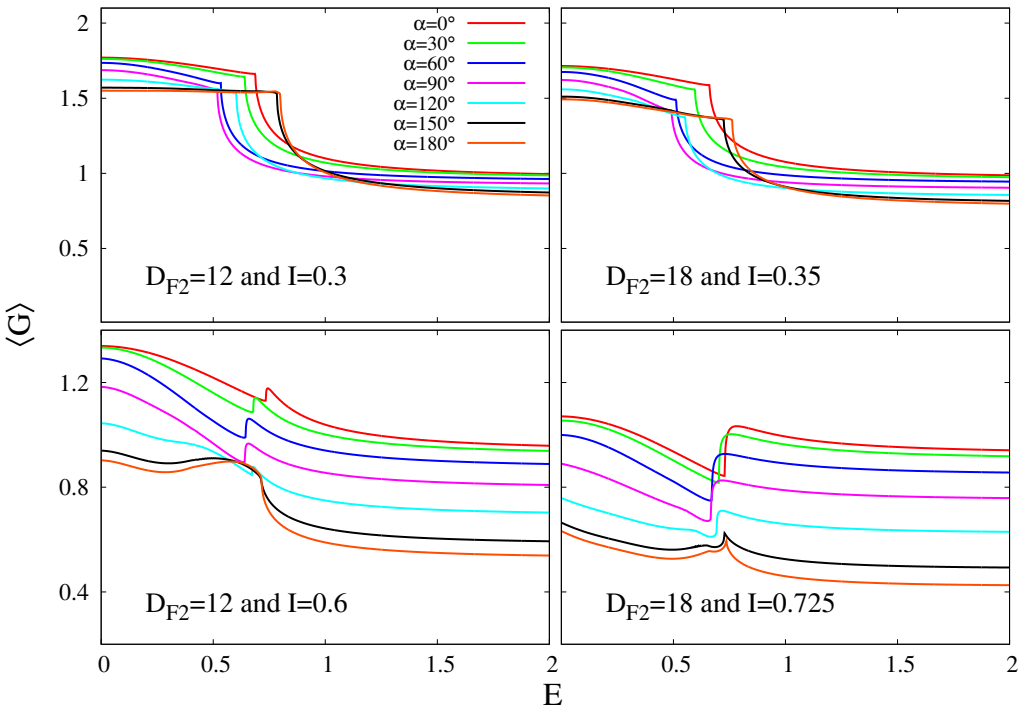

Figure 6.7: Bias dependence of the angularly averaged conductance of F_1F_2S trilayers for several angles α (see legend). In the left panels, $D_{F1} = 10$,and $D_S = 180 = 1.5\Xi_0$, as in the top panels of Fig. 6.4. In the right panels, $D_{F1} = 10$ as in the bottom panels of Fig. 6.4. In all cases, the ZBC decreases with increasing α.

resonance maximum and minimum of the ZBC in the forward scattering G. However, in the top left panel of Fig. 6.7, the ZBC is no longer a weak function of α and it gradually decreases when α is increased. Near the resonance minimum, $I = 0.6$, bottom left panel of Fig. 6.7, we can see a trace of the appearance of the FBCP when α is above 90°. This FBCP in $\langle G\rangle$ is not as prominent as that in the forward scattering G, due to the averaging.

The magnetoresistance measure $M_G(E = 2, \alpha)$ is larger for $\langle G\rangle$ than for the forward scattering conductance. For example, $M_G(E = 2, \alpha = 180°)$ in the forward scattering conductance for $I = 0.6$ and $D_{F2} = 12$ is half of that in $\langle G\rangle$. As for the zero bias magnetoresistance $M_G(E = 0, \alpha = 180°)$ in $\langle G\rangle$, it is of about the same order as $M_G(E = 2, \alpha = 180°)$ and it does not depend on where it is located in the resonance

curve, Fig. 6.5 (recall that $M_G(E=0,\alpha=180^\circ)$ for the forward scattering conductance almost vanishes at the resonance maximum).

In the right panels of Fig. 6.7, we plot results for a larger D_{F2} with values of $I=0.35$ (near a resonance maximum) and $I=0.725$ (near a resonance minimum). They share very similar features with the thinner D_{F2} case in the left panels. However, for $I=0.725$, we see that the ZBC values at different α shrink to almost or less than unity and they are just barely higher than the conductance at $E=2$ because the contributions from Andreev reflection are strongly suppressed in such a high exchange field. Another important feature in the angularly averaged results for higher exchange fields (bottom panels in Fig. 6.7) is the existence of cusps at the CB. To understand the formation of these cusps, we analyze $\langle G\rangle$ by dividing the contribution from all angles into two ranges: the range above and the range below the conventional Andreev critical angles θ_c^A (see discussion below Eq. 6.24). Consider e.g., the case of spin-up incident quasiparticles. When $\theta_c^A \equiv \sin^{-1}\left(\sqrt{\frac{1-I}{1+I}}\right) < \theta_i < \sin^{-1}\left(\sqrt{\frac{1}{1+I}}\right)$, the conventional Andreev reflected waves become evanescent while the transmitted waves are still traveling waves above the CB. When $\theta_i > \sin^{-1}\left(\sqrt{\frac{1}{1+I}}\right)$, both the conventional Andreev reflected waves and the transmitted waves become evanescent. Here, $\theta_{c\uparrow} = \sin^{-1}\left(\sqrt{\frac{1}{1+I}}\right)$ is the upper limit in Eq. 6.21.

The case of spin-down incident quasiparticles is trivial, because the dimensionless incident momentum is $\sqrt{1-I}$ which is less than both the conventional Andreev reflected wavevector, $\sqrt{1+I}$, and the transmitted wavevector, (unity in our conventions). Therefore, all the reflected and transmitted waves above the CB are traveling waves. As a result, we should consider all possible incident angles and the upper limit of Eq. 6.21 is $\pi/2$. Let us therefore focus on the nontrivial spin-up component of $\langle G\rangle$. In Fig. 6.8 we separately plot the contributions to $\langle G_\uparrow\rangle$ from angles in the range above θ_c^A (top panels) and below (bottom panels) for the field values and geometry in the left panels of Fig. 6.7, in particular $D_{F2}=12$. These contributions we will denote as $\langle G_\uparrow(E)\rangle_{above}$ and $\langle G_\uparrow(E)\rangle_{below}$ respectively. The $\langle G_\uparrow(E)\rangle_{below}$ contributions, in the bottom panels of Fig. 6.8 are, for both $I=0.3$ and $I=0.6$, similar to the result for their total forward scattering counterpart (see Fig. 6.3 and the top right panel of Fig. 6.4). Of course, the angular averaging leads to a smearing of the pronounced features originally in the forward scattering G. Qualitatively, the similarity comes from the propagating nature of

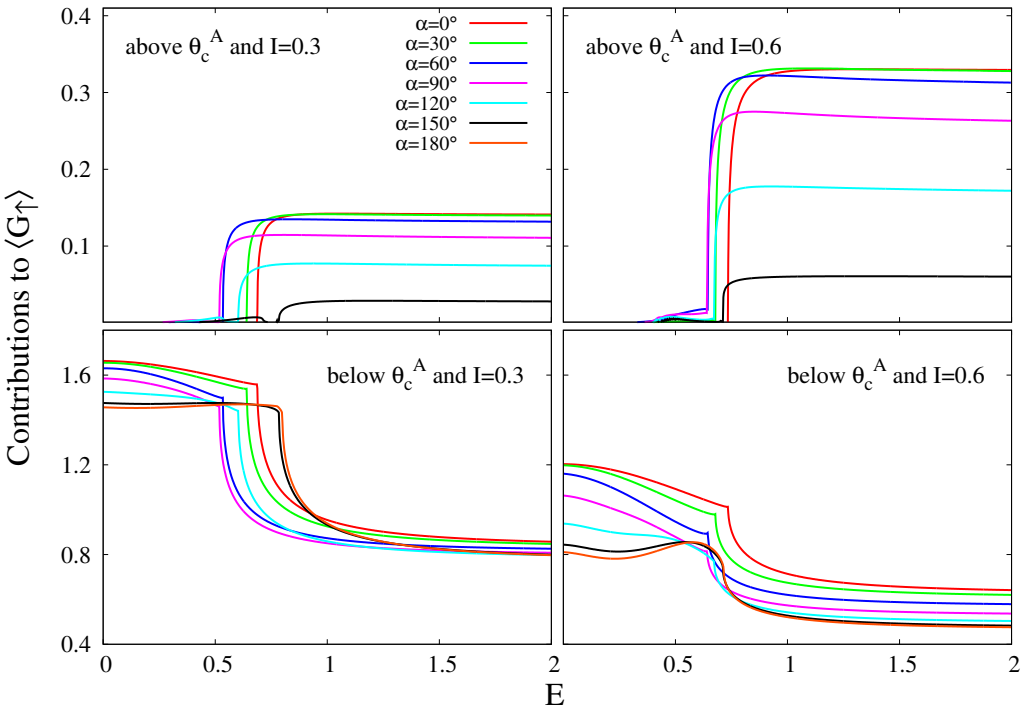

Figure 6.8: Contributions (see text) to the spin-up angularly averaged conductance, $\langle G_\uparrow \rangle$, from angular ranges above (top panels) and below (bottom panels) the Andreev critical angle θ_c^A. Several values of α are considered, as indicated. The top panel results at $\alpha = 180°$ are vanishingly small. The geometric and exchange field values are as in the left panels of Fig. 6.7. For the top panels, the plotted values at $E = 2$ decrease with increasing α. For the bottom panels, their values at both $E = 0$ and $E = 2$ decrease with increasing α.

all possible waves except the transmitted waves below the CB when $\theta_i < \theta_c^A$. Therefore, the forward scattering G is just a special example with the incident angle perpendicular to the interface.

In the subgap region, the contribution to $\langle G_\uparrow(E) \rangle_{above}$ is vanishingly small although small humps appear when the exchange fields in the two F layers are noncollinear, i.e., $\alpha \neq 0, \pi$. These small humps are generated by the process of anomalous, equal-spin Andreev reflection. This process is possible in trilayers because, in a noncollinear magnetic configuration, a spin-up quasiparticle can Andreev reflect as a spin-up hole. This can be seen from the matrix form of the BdG equations, Eq. 2.1. The occurrence

of anomalous Andreev reflection leads to some important physics which we shall discuss in the next sub-subsection. One can see from Fig. 6.8, that when the exchange fields are strictly parallel or antiparallel to each other, anomalous Andreev reflection does not arise.

Above θ_c^A, the conventional Andreev-reflected wave is evanescent and it does not contribute to $\langle G_\uparrow \rangle$. When the bias is above the saturated pair amplitude, contributions to $\langle G_\uparrow \rangle$ from the upper range are provided by both the transmitted waves and by anomalous Andreev reflected waves. Recall that ordinary transmitted waves are propagating when E is greater than the saturated pair amplitudes. We also see that $\langle G_\uparrow \rangle_{above}$ decreases with increasing α. At $\alpha = 180°$, $\langle G_\uparrow \rangle$ is vanishingly small due to the effect of a large mismatch from the antiparallel exchange field. Note also that the contribution from above θ_c^A is less in the $I = 0.3$ case than at $I = 0.6$. This is mainly due to a smaller fraction of states at $I = 0.3$ with incident angles larger than θ_c^A. On the other hand, the contribution from below θ_c^A is larger in the $I = 0.3$ case. The increase of $\langle G_\uparrow \rangle_{above}$ and the decrease of $\langle G_\uparrow \rangle_{below}$ from $I = 0.3$ to $I = 0.6$ gives rise to the cusp at the CB, when adding these two contributions together.

Anomalous Andreev reflection

As we have seen, equal-spin (anomalous) Andreev reflection (ESAR) can be generated when the magnetic configuration is noncollinear. We have previously shown that conventional Andreev reflection is forbidden when $\theta_i > \theta_c^A = \sin^{-1}\left(\sqrt{\frac{1-I_1}{1+I_1}}\right)$. Thus, θ_c^A vanishes in the half-metallic limit. In that case, conventional Andreev reflection is not allowed for any incident angle θ_i and the subgap $\langle G_\uparrow \rangle$ arises only from ESAR. For this reason, in this sub-subsection we present results for a trilayer structure that consists of one half-metal ($I_1 = 1$) and a much weaker ($I_2 = 0.1$) ferromagnet. The weaker ferromagnet serves the purpose of generating ESAR. A somewhat similar example that has been extensively discussed in the literature is that of half metal-superconductor bilayers with spin-flip interface [134, 135, 155, 156]. There the spin-flip interface plays the same role as the weaker ferromagnet here. Another interesting phenomenon also related to ESAR is the induction of triplet pairing correlations in F/S structures [33, 34, 52, 136]. To induce this type of triplet pairing, F/S systems must be in a noncollinear magnetic configuration such as F_1F_2S or F_1SF_2 trilayers with $\alpha \neq 0, \pi$. Hence, the mechanism

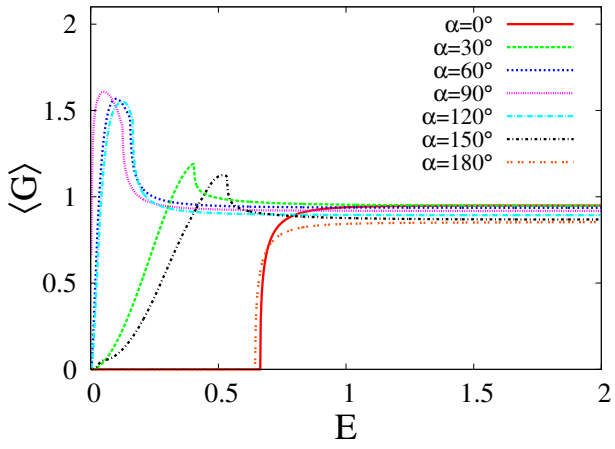

Figure 6.9: The angularly averaged conductance of F_1F_2S trilayers with exchange field $I_1 = 1$ and $I_2 = 0.1$ for several values of α. See text for discussion.

behind induced triplet pairing correlations is also responsible for ESAR and these two phenomena are closely related.

In Fig. 6.9, we plot the $\langle G \rangle$ of this particular system for several α. The geometrical parameters are again $D_{F1} = 10$, $D_{F2} = 12$, and $D_S = 180$. We have $\langle G \rangle = \langle G_\uparrow \rangle$ because the weight factor $P_\downarrow = 0$ in this half metallic case. For $\alpha = 0°$ and $\alpha = 180°$ the CB value is about 0.65 and, below the CB (in the subgap region), $\langle G \rangle$ vanishes because the conventional Andreev reflection is completely suppressed and ESAR is not allowed in the collinear cases. For $\alpha = 30°$ and $\alpha = 150°$, the CB is near 0.4 and 0.5 respectively and all of the subgap $\langle G \rangle$ is due to ESAR. The CB values for $\alpha = 60°$, $90°$, and $120°$ are 0.15, 0.12, and 0.15. For these three angles, a FBCP clearly forms, arising from the ESAR in the subgap region.

To examine the conductance in the subgap region, which is in this case due only to ESAR, we choose the $\alpha = 150°$ angle and plot, in Fig. 6.10, the contributions to G (for this case G and $\langle G \rangle$ are very similar) from the reflected spin-up particle and the reflected spin-up hole wavefunctions. The spin-down particle and spin-down hole wavefunctions are evanescent and do not contribute to the conductance. Thus, Eq. 6.20 reads $G = 1 + (k^-_{\uparrow 1}/k^+_{\uparrow 1})|a_\uparrow|^2 - |b_\uparrow|^2$. The quantities plotted are the second ((green) curve) and third ((red) curve, highest at the origin) terms in this expression. The value of G is also plotted. One sees that the reflected ESAR amplitudes decay very quickly

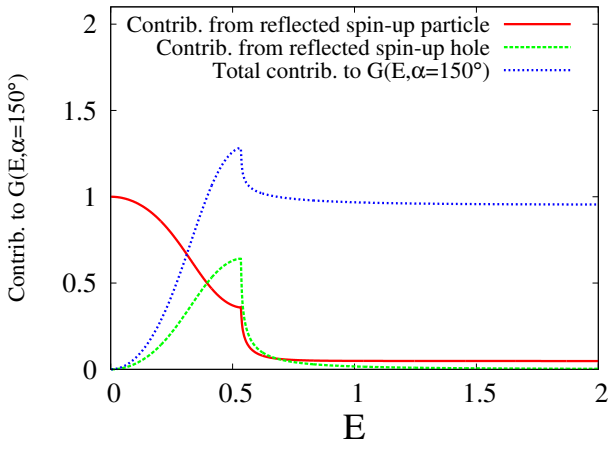

Figure 6.10: Contributions to $G(E, \alpha = 150°)$, computed for the parameter values used in Fig. 6.9, from the spin-up quasiparticle and spin-up quasihole ESAR (see text for discussion). The total G is also shown.

above the CB. However, these reflected amplitudes are quite appreciable in the subgap region. In other words, the supercurrent in the subgap region contains signatures of the triplet correlations. This confirms the simple picture [45] that above the CB the current flowing throughout the junction is governed by the transport of quasiparticles. However, below the CB it is dominated by ESAR.

Spin current densities and spin transfer torques

Finally, we now report on spin-dependent transport quantities, including the spin current, the spin transfer torques, and their connections to the local magnetization at finite bias. An objective here is to demonstrate that the conservation law Eq. 6.25 which in the steady state is simply:

$$\frac{\partial}{\partial y} S_i = \tau_i, \quad i = x, y, z, \tag{6.34}$$

is satisfied in our self-consistent calculations for F_1F_2S trilayers. We consider these spin dependent quantities in a trilayer with $I = 0.1$ and a noncollinear orthogonal magnetic configuration, $\alpha = 90°$. Thus, the internal field in the outer electrode F_1 is along the z axis, while that in F_2 is along x. The thicknesses are $D_{F1} = 250$, $D_{F2} = 30$, and $D_S = 250 = 5\Xi_0$.

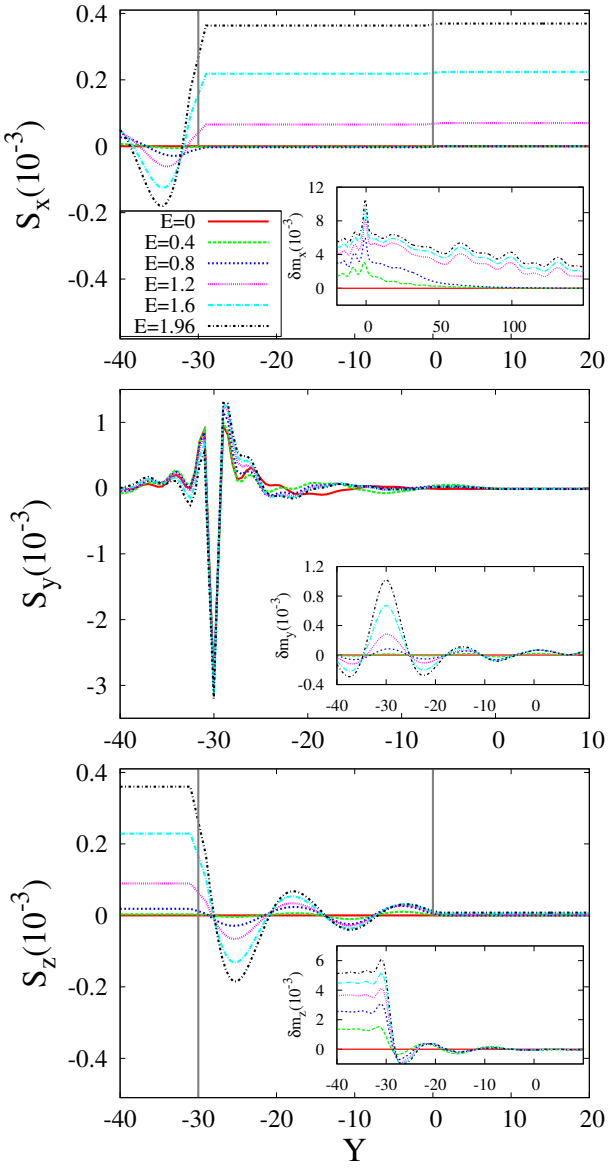

Figure 6.11: The components of the spin current density, S_x, S_y, and S_z, calculated from Eq. 6.29 are plotted vs $Y \equiv k_F y$ for several values of the bias $E \equiv eV$ (main panels). We have $\alpha = 90°$, $I = 0.1$, $D_{F1} = 250$, $D_{F2} = 30$, $D_S = 250 = 5\Xi_0$. The F_2S interface is at $Y = 0$ and the F_1F_2 interface at $Y = -30$. Vertical lines at these interfaces in the top and bottom panels help locate the different regions. Only the central portion of the Y range is included (see text). The ranges included depend on the component. The insets show the change in each component of the local magnetization, $\delta\mathbf{m}(E) \equiv \mathbf{m}(E) - \mathbf{m}(0)$, also as a function of Y. The values of E are as in the main plot, the ranges included may be different.

A set of results is shown in Fig. 6.11. There, in the three main plots, we display the three components of the spin current density, computed from Eqs. 6.29 and normalized as explained below that equation. They are plotted as functions of the dimensionless position $Y \equiv k_F y$ for several values of the bias V, $E \equiv eV$. The F_2S interface and the F_1F_2 interface are located at $Y = 0$ and $Y = -30$, respectively. For clarity, only the range of Y corresponding to the "central" region near the interfaces is included in these plots: the shape of the curves deeper into S or F_1 can be easily inferred by extrapolation. From these main panels, one sees that the current is spin-polarized in the x-direction (the direction of the exchange field in F_2) to the right of F_1F_2 interface, including the S region. Furthermore, S_x is found to be a constant except in the F_1 region, where it exhibits oscillatory behavior. This indicates the existence of a non-vanishing, oscillating spin transfer torque in the F_1 layer, as we will verify below. We also see that S_x vanishes when the bias is less than the superconducting gap in bulk S ($E < 1$ in our notation). In fact, the behavior of S_x with V is similar to that of the ordinary charge current in an N/S tunneling junction with a very strong barrier where there is no current until $V > \Delta_0$. This phenomenon is very different from what occurs in ordinary spin valves (F_1F_2), where the spin current is not blocked below any finite characteristic bias.

The S_y component, along the normal to the layers, is shown in the middle main panel of Fig. 6.11. It depends extremely weakly on the bias E. It is very small except near the interface between the two ferromagnets but there it is about an order of magnitude larger than the other two components. Hence only a somewhat smaller Y range is shown. Unlike the S_x and S_z components, S_y does not vanish even when there is no bias applied to the trilayer (the (red) curve in this panel). From these observations, one can infer that S_y is largely derived from its static part with only a very small contribution from the effect of finite bias. The emergence of a static spin current is due to the leakage of the local magnetization m_z into the F_2 layer and of m_x into the F_1 layer. This explains why the static spin current S_y is mostly localized near the F_1F_2 interface. The S_z component (lower panel) is constant in the F_1 region, as one would expect. It oscillates in the F_2 region, and vanishes in the S layer. As opposed to the S_x component, S_z is non-vanishing, although very small, when $E < 1$. It increases rapidly with bias when $E > 1$. The oscillatory behavior of S_z, again, is related to the local spin transfer torque as we will verify below.

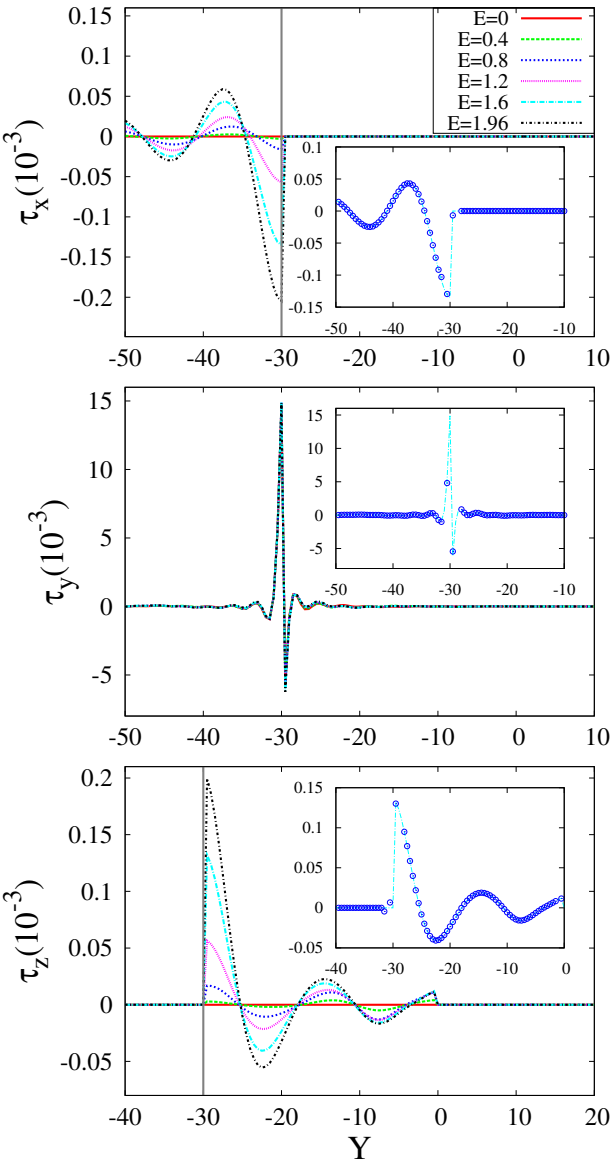

Figure 6.12: The components of the spin transfer torque $\boldsymbol{\tau} \equiv 2\mathbf{m} \times \mathbf{h}$ plotted vs Y for several bias values. All parameters and geometry are as in Fig. 6.11. Vertical lines, denoting interfaces, are in the top and bottom panels. The insets show (for bias $E = 1.6$) the torque ((blue) dashed line) and the derivative of the component of spin current density ((blue) circles). The lines and circles agree, proving that Eq. 6.34 holds.

We can summarize the behavior of the spin current vector, in this $\alpha = 90^\circ$ configuration, as follows: when $E > 1$, the spin current, which is initially (at the left side) spin-polarized in the $+z$ direction, is twisted to the x direction under the action of the spin torques discussed below, as it passes through the second magnet, which therefore acts as a spin filter. The current remains then with its spin polarization in the $+x$ direction as it flows through the superconductor. Thus, in this range of E the trilayer switches the polarization of the spin current. On the other hand, when $E < 1$, the small z-direction spin-polarized current tunneling into the superconductor is gradually converted into supercurrent and becomes spin-unpolarized.

In the insets of the three panels of Fig. 6.11, we illustrate the behavior with bias of the corresponding component of the local magnetization as it is carried into S. Specifically, we plot the components of the vector difference between the local magnetization with and without bias, $\delta\mathbf{m}(E) \equiv \mathbf{m}(E) - \mathbf{m}(E = 0)$, as a function of Y. The range of Y is chosen to display the salient aspects of the behavior of this quantity, and it is not the same as in the main plots, nor is it the same for each component. The bias values are the same as in the main plots, however. The magnetizations are computed from Eqs. 6.27 and normalized in the usual way, as discussed below Eqs. 6.29. In these units, and at $I = 0.1$ the value of the dominant component of $\mathbf{m}$ in the magnetic layers is about 0.15. This scale should be kept in mind.

The behavior of the x component is nontrivial in the F_2 and S regions, and the corresponding Y range is included in the top panel inset. When the applied bias is below the bulk S gap value, $\delta m_x(E)$ penetrates into the S layer with a decay length $\sim \Xi_0 = 50$. This decay length is much longer than that found for the static magnetization, $\mathbf{m}(0)$. [52] When the bias is above the gap, $\delta m_x(E)$ penetrates even more deeply into the S layer, with a clearly very different behavior than for $E < 1$. This long-range propagation is of course consistent with the behavior of S_x, as S_x, the spin current polarized in the x direction, appears only when $E > 1$. The magnitude of δm_y is much smaller than that of δm_x or δm_z. It peaks near the F_1F_2 interface and that range of Y is emphasized in the middle inset. Its overall scale monotonically increases with increasing bias. It damps away from the interface in an oscillatory manner. As to δm_z, which can conveniently be plotted in the same Y range, it decays with a very short decay length and oscillates in F_2. The overall damped oscillatory behavior of δm_y and δm_z in the F_2 region reflects

the precession, as a function of position, of the spin density around the local exchange field that points toward the $+x$ direction. This phenomenon is well known in spin valves [157]. The oscillation periods for δm_y, δm_z, S_x, and S_z are very similar and of the order of $1/(Ik_{FS})$.

Next, we investigate the spin transfer torque, $\boldsymbol{\tau} \equiv 2\mathbf{m} \times \mathbf{h}$. This quantity, computed from the normalized values of I and $\mathbf{m}$, is plotted as a function of position in Fig. 6.12 for the same system as in Fig. 6.11. Results are shown for each of its three components in the main panels of the figure. One sees that at zero bias, $E = 0$, both τ_x and τ_z vanish identically. In the F_1 layer, τ_x increases in magnitude with increasing E. It vanishes in F_2 and in S. The behavior of τ_z is, as one would expect, the converse: it vanishes in F_1 and S, and its magnitude increases in F_2. The oscillatory behavior of τ_x and τ_z is consistent, as we shall see below, with the results for S_x and S_y. The component normal to the layers, τ_y, is non-vanishing only near the F_1F_2 interface, although its peak there attains a rather high value, nearly two orders of magnitude larger than the peak value of the other components. It is independent of bias, consistent with the behavior of S_y.

In the insets, we verify, for each component, that Eq. 6.34 is satisfied, that is, that our self-consistent methods strictly preserve the conservation laws in this nontrivial case. (We have already mentioned that we have verified that the charge or particle current are independent of y). We specifically consider the bias value $E = 1.6$ as an illustration. Consider first the top panel inset. There we plot both the x component of the spin transfer torque, τ_x (blue dashes), taken from the corresponding main plot, and the derivative of the spin current, $\partial S_x/\partial Y$ (blue circles), obtained by numerically differentiating the corresponding result in the top panel of Fig. 6.11. Clearly, the curves are in perfect agreement. (One can easily check that with the normalizations and units chosen there should be no numerical factor between the two quantities). In the second panel, the same procedure is performed for the y component, although in this case, because of the very weak dependence of both S_y and τ_y on bias, the value of the latter is hardly relevant. Nevertheless, despite the evident difficulty in computing the numerical derivative of the very sharply peaked S_y, the agreement is excellent. For τ_z, its vanishing in the F_1 region is in agreement with the constant spin current in that layer. The conservation law, Eq. 6.34, is verified in the inset for this component, again at bias $E = 1.6$. Just as for the x component, the dots and the line are on top of each

other. Thus, the conservation law for each component is shown to be perfectly obeyed.

The results of this sub-subsection can be summarized as follows: the finite bias leads to spin currents. As opposed to the ordinary charge currents, these spin currents are generally not conserved locally because of the presence of the spin transfer torques which act as source terms and are responsible for the change of spin density. But a self-consistent calculation *must* still contain exactly the correct amount of non-conservation, that is, Eq. 6.34 must be satisfied. It is therefore of fundamental importance to verify that it is, as we have.

6.4 Conclusions

In summary, we have investigated important transport properties of F_1F_2S trilayers, including tunneling conductances and spin transport. To properly take into account the proximity effects that lead to a spatially varying pair potential, we have incorporated a transfer matrix method into the BTK formalism. This allows us to use self-consistent solutions of the BdG equations. This technique also enables us to compute spin transport quantities including spin transfer torque and spin currents. We have shown that in F/S bilayers the self-consistent calculations lead to conductances at the superconducting gap that increase with the Fermi wavevector mismatch whereas non-self-consistent ones predict they are insensitive to this parameter. In F_1F_2S trilayers, we have found that the critical bias CB (where tunneling conductance curves drop) for different relative magnetization angles, α, depends on the strength of the superconducting order parameter near the interface. The angular dependence of the critical bias reflects that of the transition temperatures T_c, which are usually non-monotonic functions of α. For forward scattering in these F_1F_2S trilayers, we found that the dependence of the zero bias conductance peak (ZBCP) on α is related to both the strength of the exchange fields and the thickness of the F_2 layers. This remarkable behavior can be explained via quantum interference effects. At the resonance minimum, the ZBCP drops significantly and monotonically from $\alpha = 0^\circ$ to $\alpha = 180^\circ$. On the other hand, the α dependence of the ZBCP is very weak when it is at its resonance maximum. For asymmetric cases where $I_1 \neq I_2$, we found that the ZBCP is a non-monotonic function of α with its

value at $\alpha = \pi/2$ being the maximum. We have also investigated the angularly averaged tunneling conductances, $\langle G \rangle$, and found that features of resonance effects are then somewhat washed out due to the averaging. However, by studying $\langle G \rangle$ in the subgap regions, we found that anomalous (equal-spin) Andreev reflection (ESAR) arises when α corresponds to noncollinear orientations. The emergence of ESAR is correlated with the well-known induced triplet pairing correlations in proximity coupled F/S structures. When the outer magnet is a half metal, the $\langle G \rangle$ signatures arise chiefly from the process of ESAR. We have also studied the bias dependence of the spin currents and spin transfer torques and their general behavior in F_1F_2S trilayers with $\alpha = 90^\circ$ (the exchange fields in F_1 and F_2 point toward the z and x directions, respectively). The spin current components are in general non-conserved quantities. The S_z component, parallel to the local exchange field in the F_1 layer, does not change in the F_1 region but shows damped oscillatory behavior in the F_2 layer and eventually vanishes in the S region. However, S_x is a constant throughout the F_2 and S regions and oscillates in F_1 layers. We found that S_y (the component normal to the layers) depends very weakly on the bias, and thus its spatial dependence arises largely from a static effect. The bias dependence of S_x in the S region is very similar to that of the tunneling charge current in normal/superconductor systems with high barriers: S_x vanishes in the subgap regions and arises right above the gap. The behavior of $\mathbf{m}$ is consistent with that of $\mathbf{S}$. We found that m_x, parallel to the local exchange fields in F_2, spreads out over the S regions when the bias is larger than the superconducting gap. We have also investigated the bias dependence of the spin transfer torques, and we have carefully verified that the appropriate continuity equation for the spin current is strictly obeyed in our self-consistent approach. Our method can be extended to include the effects of interfacial scattering and wavevector mismatch. It can also be used for further study of the intricate phenomena associated with spin transport in these systems.

Chapter 7

Conclusions

In this chapter, we will conclude this thesis with a summary. In Chap. 1, we reviewed the fundamental physics of superconducting proximity effects in ferromagnet/superconductor (F/S) layered heterostructures. The proximity effects often lead to interesting non-monotonic dependence of critical temperatures, T_c, on experimental controllable variables, such as the thicknesses of F layers and the relative angle, α, between the magnetizations in F layers of F_1F_2S structures. The induction of triplet correlations is another cornerstone of proximity effects due to their long-range nature that is important for studying Josephson junctions. The emergence of the long-range triplet correlations often rely on the presence of magnetic inhomogeneity in F/S systems. For these reasons, it is of fundamental importance to study proximity effects in F/S structures with inhomogeneous magnetization, including F_1F_2S trilayers and conical magnet/S bilayers.

In F_1F_2S trilayers, we studied (see Chap. 2) proximity effects by self-consistently solving the BdG equations. We predict that T_c is a non-monotonic function of α with the minimum that often occurs near $\alpha = \pi/2$. This property makes them different than that found in F_1SF_2 trilayers, where T_c monotonically increases with α. For certain values of the exchange field and the thicknesses of the F and the S layers, the system may exhibit reentrant superconductivity with α. In addition, we demonstrate the existence of the long-range triplet superconductivity. The results also indicate a connection between the equal-spin triplet pairing and the singlet pairing state that characterizes T_c. Our theoretical results for T_c are both qualitatively and quantitatively in good agreement with experiments (see Chap. 3). We found that the non-monotonicity of $T_c(\alpha)$ found in

experiments is correlated with triplet superconductivity and also involves the process of singlet-to-triplet conversion.

In conical magnet/S bilayers, we studied (see Chap. 4) both singlet and triplet proximity effects by solving the BdG equations self-consistently. We compute T_c as a function of the magnet thickness, d_F. We find that $T_c(d_F)$ contains several oscillations and the periodicity of these oscillations is governed by both the periodicity of the conical magnetization and the strength of exchange fields. In addition to the usual reentrant superconductivity with d_F that can occur in this system, a novel transition phenomenon, reentrance with temperatures (T), is also found in certain cases. In the T reentrance, the relevant thermodynamic functions reveal that the superconducting state is less ordered than the normal state in a certain range of T. We verified the existence of these long-range triplet correlations. The proximity lengths of these correlations, as functions of d_F, oscillate with a periodicity similar to or proportional to that of the conical magnetization. We compared our theoretical fit to $T_c(d_F)$ with experiments (see Chap. 5) on Ho/S bilayers and found they are in good agreement.

We also studied in Chap. 6 transport properties of F_1F_2S structures, such as tunneling conductance and spin transfer torques. By using transfer matrix techniques, we are able to combine the original BTK formalism with self-consistent solutions of the BdG equations to take into account the proximity effects. Our results indicate that only when a self-consistent approach is adopted can one correctly quantify the tunneling conductance. We found that the forward scattering tunneling conductance often exhibits interesting resonance phenomena. For the angularly averaged results, the equal-spin Andreev reflection may occur in the subgap regions and is also related to the triplet correlations. We have investigated both spin currents and spin transfer torque and found that the conservation law is always satisfied in our framework. The bias dependence of spin currents indicates that, by changing the relative angle between magnetizations, one can manipulate the spin polarization of the tunneling current.

In summary, as a consequence of superconducting proximity effects in F/S heterostructures with inhomogeneous magnetization, our results reveal the importance of their underlying physics and many of them have been confirmed experimentally. In addition, these systems can have important applications to spintronics due to their superconducting switching effects.

References

[1] M. Tinkham, *Introduction to Superconductivity* (Dover Books, Mineola, NY, 1996).

[2] G. Grosso and G. P. Parravicini, *Solid State Physics* (Elsevier, Amsterdam, Netherlands, 2000).

[3] W. Meissner and R. Ochsenfeld, Naturwissenschaften **21**, 787 (1933).

[4] J. Bardeen, L. N. Cooper, and J. R. Schrieffer, Phys. Rev. **106**, 162 (1957).

[5] L. N. Cooper, Phys. Rev. **104**, 1189 (1956).

[6] N. N. Bogoliubov, Nuovo Cimento **7**, 794 (1958).

[7] J. G. Valatin, Nuovo Cimento **7**, 843 (1958).

[8] R. Holm and W. Meissner, Z. Phys. **74**, 715 (1932).

[9] B. D. Josephson, Physics Letters **1**, 251 (1962).

[10] G. Deutscher and P. G. de Gennes, 1969, "Proximity Effects" in *Superconductivity*, edited by R. D. Parks (Dekker, New York), pp. 1005-1034.

[11] A. C. Mota, P. Visani, and A. Pollini, J. Low Temp. Phys. **76**, 465 (1989).

[12] A. F. Andreev, Sov. Phys. JETP **19**, 1228 (1964).

[13] A. I. Buzdin, Rev. Mod. Phys. **77**, 935 (2005).

[14] I. Zutić, J. Fabian, and S. Das Sarma, Rev. Mod. Phys. **76**, 323 (2004).

[15] E. A. Demler, G. B. Arnold, and M. R. Beasley, Phys. Rev. B **55**, 15174 (1997).

[16] K. Halterman and O. T. Valls, Phys. Rev. B **65**, 014509 (2001).

[17] P. Fulde and A. Rerrel, Phys. Rev. **135**, A550 (1964).

[18] A. Larkin and Y. Ovchinnikov, Sov. Phys. JETP **20**, 762 (1965).

[19] Z. Radović, M. Ledvij, L. Dobrosavljević-Grujić, A. I. Buzdin, and J. R. Clem, Phys. Rev. B **44**, 759 (1991).

[20] M. G. Khusainov and Y. N. Proshin, Phys. Rev. B **56**, R14283 (1997).

[21] Y. V. Fominov, N. M. Chtchelkatchev, and A. A. Golubov, Phys. Rev. B **66**, 014507 (2002).

[22] J. S. Jiang, D. Davidović, D. H. Reich, and C. L. Chien, Phys. Rev. Lett. **74**, 314 (1995).

[23] I. A. Garifullin, D. A. Tikhonov, N. N. Garif'yanov, L. Lazar, Yu. V. Goryunov, S. Ya. Khlebnikov, L. R. Tagirov, K. Westerholt, and H. Zabel, Phys. Rev. B **66**, 020505(R) (2002).

[24] V. Zdravkov, A. Sidorenko, G. Obermeier, S. Gsell, M. Schreck, C. Müller, S. Horn, R. Tidecks, and L. R. Tagirov, Phys. Rev. Lett. **97**, 057004 (2006).

[25] V. Zdravkov, J. Kehrle, G. Obermeier, S. Gsell, M. Schreck, C. Mller, H.-A. Krug von Nidda, J. Lindner, J. Moosburger-Will, E. Nold, R. Morari, V. V. Ryazanov, A. S. Sidorenko, S. Horn, R. Tidecks, and L. R. Tagirov, Phys. Rev. B **82**, 054517 (2010).

[26] I. Baladié and A. Buzdin, Phys. Rev. B **67**, 014523 (2003).

[27] K. Halterman and O. T. Valls, Phys. Rev. B **70**, 104516 (2004).

[28] K. Halterman and O. T. Valls, Phys. Rev. B **72**, 060514(R) (2005).

[29] F. S. Bergeret, A. F. Volkov, and K. B. Efetov, Phys. Rev. Lett. **86**, 3140 (2001).

[30] F. S. Bergeret, A. F. Volkov, and K. B. Efetov, Phys. Rev. B **68**, 064513 (2003).

[31] F. S. Bergeret, A. F. Volkov, and K. B. Efetov, Rev. Mod. Phys. **77**, 1321 (2005).

[32] T. Löfwander, T. Champel, J. Durst, and M. Eschrig, Phys. Rev. Lett. **95**, 187003 (2005).

[33] K. Halterman, P. H. Barsic, and O. T. Valls, Phys. Rev. Lett. **99**, 127002 (2007).

[34] K. Halterman, O. T. Valls, P. H. Barsic, Phys. Rev. B **77**, 174511, (2008).

[35] V. L. Berezinskii, JETP Lett. **20**, 287, (1974).

[36] M. Giroud, H. Courtois, K. Hasselbach, D. Mailly, and B. Pannetier, Phys. Rev. B **58**, R11872 (1998).

[37] T. S. Khaire, M. A. Khasawneh, W. P. Pratt, Jr., and N. O. Birge, Phys. Rev. Lett. **104** 137002 (2010).

[38] J. W. A. Robinson, J. D. S. Witt, and M. G. Blamire, Science **329**, 59 (2010).

[39] L. R. Tagirov., Phys. Rev. Lett. **83**, 2058 (1999).

[40] A. I. Buzdin, A. V. Vedyayev, and N. V. Ryzhanova, Europhys. Lett. **48**, 686 (1999).

[41] J. Y. Gu, C.-Y. You, J. S. Jiang, J. Pearson, Ya. B. Bazaliy, and S. D. Bader, Phys. Rev. Lett. **89**, 267001 (2002).

[42] I. C. Moraru, W. P. Pratt, Jr., and N. O. Birge, Phys. Rev. Lett. **96**, 037004 (2006).

[43] C. Visani, V. Peña, J. Garcia-Barriocanal, D. Arias, Z. Sefrioui, C. Leon, J. Santamaría, N. M. Nemes, M. Garcia-Hernandez, J. L. Martinez, S. G. E. te Velthuis, and A. Hoffmann , Phys. Rev. B **75**, 054501 (2007).

[44] J. Zhu, I. N. Krivorotov, K. Halterman, and O. T. Valls, Phys. Rev. Lett. **105**, 207002 (2010).

[45] G. E. Blonder, M. Tinkham, and T. M. Klapwijk, Phys. Rev. B **25**, 4515 (1982).

[46] M. J. M. de Jong and C. W. J. Beenakker, Phys. Rev. Lett. **74**, 1657 (1995).

[47] I. Zutić and O. T. Valls, Phys. Rev. B **58**, 8738 (1999).

[48] I. Zutić and O. T. Valls, Phys. Rev. B **60**, 6320 (1999).

[49] R. J. Soulen Jr., J. M. Byers, M. S. Osofsky, B. Nadgorny, T. Ambrose, S. F. Cheng, P. R. Broussard, C. T. Tanaka, J. Nowak, J. S. Moodera, A. Barry, and J. M. D. Coey, Science **282**, 85 (1998).

[50] S. K. Upadhyay, A. Palanisami, R. N. Louie, and R. A. Buhrman, Phys. Rev. Lett. **81**, 3247 (1998).

[51] Ya. V. Fominov, A. A. Golubov, T. Yu. Karminskaya, M. Yu. Kupriyanov, R. G. Deminov, L. R. Tagirov, JETP Letters **91**, 308 (2010).

[52] C.-T. Wu, K. Halterman, and O. T. Valls, Phys. Rev. B **86**, 014523 (2012).

[53] A. A. Jara, C. Safranski, I. N. Krivorotov, C.-T. Wu. A. N. Malmi-Kakkada, O. T. Valls, and K. Halterman, Phys. Rev. B **89**, 184502 (2014).

[54] P. H. Barsic and O. T. Valls, Phys. Rev. B **79**, 014502 (2009).

[55] C.-T. Wu, K. Halterman, and O. T. Valls, Phys. Rev. B **86**, 184517 (2012).

[56] F. Chiodi, J. D. S. Witt, R. G. J. Smits, L. Qu, Gabor B. Halasz, C.-T. Wu, O. T. Valls, K. Halterman, J. W. A. Robinson, and M. G. Blamire, Europhys. Lett. **101**, 37002 (2013).

[57] P. G. de Gennes, *Superconductivity of Metals and Alloys* (Addison-Wesley, Reading, MA, 1989).

[58] K. Halterman and O. T. Valls, Phys. Rev. B **66**, 224516 (2002).

[59] M. Eschrig and T. Löfwander, Nature Physics **4**, 138 (2008).

[60] M. Eschrig, J. Kopu, J. C. Cuevas, and Gerd Schön, Phys. Rev. Lett. **90**, 137003 (2003);

[61] M. Eschrig, T. Löfwander, T. Champel, J. C. Cuevas, J. Kopu, and G. Schön, J. Low temp. Phys, **147** 457 (2007).

[62] M. Grein, M. Eschrig, G. Metalidis, and Gerd Schön, Phys. Rev. Lett. **102**, 227005 (2009).

[63] J. Y. Gu, J. Kusnadi and C.-Y. You, Phys. Rev. B **81**, 214435 (2010).

[64] D. Sprungmann, K. Westerholt, H. Zabel, M. Weides, and H. Kohlstedt, Phys. Rev. B **82**, 060505 (2010).

[65] C.-T. Wu, O.T. Valls, and K. Halterman, Phys. Rev. Lett. **108**, 117005 (2012).

[66] S. Oh, D. Youm, and M. R. Beasley, Appl. Phys. Lett. **71**, 2376 (1997).

[67] T. Y. Karminskaya, A. A. Golubov, and M. Y. Kupriyanov, Phys. Rev. B **84**, 064531 (2011).

[68] Q. Cheng, and B. Jin, Physica C: Superconductivity **473**, 29 (2012).

[69] M. Knežević, L. Trifunovic, and Z. Radović, Phys. Rev. B **85**, 094517 (2012).

[70] A. Potenza and C. H. Marrows, Phys. Rev. B **71**, 180503(R) (2005).

[71] P. V. Leksin, N. N. Garif'yanov, I. A. Garifullin, J. Schumann, H. Vinzelberg, V. Kataev, R. Klingeler, O. G. Schmidt, and B. Büchner, Appl. Phys. Lett. **97**, 102505 (2010).

[72] P. V. Leksin, N. N. Garif'yanov, I. A. Garifullin, J. Schumann, V. Kataev, O. G. Schmidt, and B. Büchner, Phys. Rev. Lett. **106**, 067005 (2011).

[73] K. Westerholt, D. Sprungmann, H. Zabel, R. Brucas, B. Hjörvarsson, D. A. Tikhonov, and I. A. Garifullin, Phys. Rev. Lett. **95**, 097003 (2005).

[74] G. Nowak, H. Zabel, K. Westerholt, I. Garifullin, M. Marcellini, A. Liebig, and B. Hjörvarsson, Phys. Rev. B **78**, 134520 (2008).

[75] A. Frydman and R. C. Dynes, Phys. Rev. B **59**, 8432, (1999).

[76] V. N. Krivoruchko and E. A. Koshina, Phys. Rev. B **66**, 014521 (2002).

[77] K. Halterman and O. T. Valls, Phys. Rev. B **69**, 014517 (2004).

[78] F. S. Bergeret, A. F. Volkov, and K. B. Efetov, Phys. Rev. B **69**, 174504 (2004).

[79] P. H. Barsic, O. T. Valls, and K. Halterman, Phys. Rev. B **75**, 104502 (2007).

[80] I. Kosztin, Š. Kos, M. Stone, A. J. Leggett, Phys. Rev. B **58**, 9365 (1998).

[81] I. C. Moraru, W. P. Pratt, Jr., and N. O. Birge, Phys. Rev. B. **74**, 220507(R) (2006).

[82] P. V. Leksin, N. N. Garif'yanov, I. A. Garifullin, Ya. V. Fominov, J. Schumann, Y. Krupskaya, V. Kataev,O. G. Schmidt, and B. Büchner, Phys. Rev. Lett. **109**, 057005 (2012).

[83] Y. Liu, C. Visani, N. M. Nemes, M. R. Fitzsimmons, L. Y. Zhu, J. Tornos, M. Garcia-Hernandez, M. Zhernenkov, A. Hoffmann, C. Leon, J. Santamaría, and S. G. E. te Velthuis, Phys. Rev. Lett. **108**, 207205 (2012).

[84] V. I. Zdravkov, J. Kehrle, G. Obermeier, D. Lenk, H.-A. Krug von Nidda, C. Müller, M. Yu. Kupriyanov, A. S. Sidorenko, S. Horn, R. Tidecks, and L. R. Tagirov, Phys. Rev. B **87**, 144507 (2013).

[85] L. Y. Zhu, Yaohua Liu, F. S. Bergeret, J. E. Pearson, S. G. E. te Velthuis, S. D. Bader, and J. S. Jiang, Phys. Rev. Lett. **110**, 177001 (2013).

[86] B. Li, N. Roschewsky, B. A. Assaf, M. Eich, M. Epstein-Martin, D. Heiman, M. Münzenberg, and J. S. Moodera, Phys. Rev. Lett. **110**, 097001 (2013).

[87] G. Nowak, K. Westerholt and H. Zabel, Supercond. Sci. Technol. **26** 025004 (2013).

[88] T. Gredig, I. N. Krivorotov, C. Merton, A. M. Goldman, and E. D. Dahlberg, J. Appl. Phys. **87**, 6418 (2000).

[89] S. S. P. Parkin, R. Bhadra, and K. P. Roche, Phys. Rev. Lett. **66**, 2152 (1991).

[90] K. Halterman and O. T. Valls, Phys. Rev. B **80**, 104502 (2009).

[91] A. F. Volkov, A. Anishchanka, and K. B. Efetov, Phys. Rev. B, **73**, 104412 (2006).

[92] I. Sosnin, H. Cho, V. T. Petrashov, and A. F. Volkov, Phys. Rev. Lett. **96**, 157002 (2006).

[93] J. W. Cable, E. O. Wollan, W. C. Koehler, and M. K. Wilkinson, Phys. Rev. **140**, A1896 (1965).

[94] E.A. Karhu, S. Kahwaji, M. D. Robertson, H. Fritzsche, B. J. Kirby, C. F. Majkrzak, and T. L. Monchesky, Phys. Rev. B **84**, 060404 (2011).

[95] H. Shi, Z.-B. Huang, J. S. Tse, and H.-Q. Lin, J. Appl. Phys. **110**, 043917 (2011).

[96] M. Alidoust, J. Linder, G. Rashedi, T. Yokoyama, and A. Sudbø, Phys. Rev. B **81**, 014512 (2010).

[97] M. Alidoust and J. Linder, Phys. Rev. B **82**, 224504 (2010).

[98] G. B. Halász, M. G. Blamire, and J. W. Robinson Phys. Rev. B **84**, 024517 (2011).

[99] G. B. Halász, J. W. A. Robinson, J. F. Annett, M. G. Blamire, Phys. Rev. B **79**, 224505 (2009).

[100] W. A. Fertig, D. C. Johnston, L. E. DeLong, R. W. McCallum, M. B. Maple, and B. T. Matthias, Phys. Rev. Lett. **38**, 987 (1977).

[101] D. E. Moncton, D. B. McWhan, J. Eckert, G. Shirane, and W. Thomlinson, Phys. Rev. Lett. **39**, 1164 (1978).

[102] H. R. Ott, W. A. Fertig, D. C. Johnston, M. B. Maple, and B. T. Matthias, J. Low Temp. Phys. **33**, 159 (1978).

[103] G. W. Crabtree, F. Behroozi, S. A. Campbell, and D. G. Hinks, Phys. Rev. Lett. **49**, 1342 (1982).

[104] J. W. Lynn, J. A. Gotaas, R. N. Shelton, H. E. Horng, and C. J. Glinka, Phys. Rev. B **31**, 5756 (1985).

[105] R. Prozorov, M. D. Vannette, S. A. Law, S. L. Budko, and P. C. Canfield, Phys. Rev. B **77**, 100503(R)

[106] In $ErRh_4B_4$ it is only 0.3 K (Ref. [105]) in $HoMo_6S_8$ even less.

[107] P. Anderson and H. Suhl, Phys. Rev. **116**, 898 (1959).

[108] L. Brossard, M. Ribault, L. Valade, and P. Cassoux, Phys. Rev. B **42**, 3935 (1990).

[109] T. H. Lin, X. Y. Shao, M. K. Wu, P. H. Hor, X. C. Jin, C. W. Chu, N. Evans, and R. Bayuzick, Phys. Rev. B **29**, 1493(R) (1984).

[110] The phase convention used here is that of e.g. Ref. [65]. Other conventions may lead to slightly different signs in the equations (see Chap. 2).

[111] F.S. Bergeret, A. Levy Yeyati, and A. Martín-Rodero, Phys. Rev. B **72**, 064524 (2005).

[112] M. Yu. Kharitonov, A.F. Volkov, and K. B. Efetov, Phys. Rev. B **73**, 054511 (2006).

[113] J. Linder, T. Yokoyama, and A. Sudbø, Phys. Rev. B **79**, 054523 (2009).

[114] See e.g. G. Aeppli *et al*, Phys. Rev. B **28**, 5160 (1983).

[115] V. V. Ryazanov, V. A. Oboznov, A. Yu. Rusanov, A. V. Veretennikov, A. A. Golubov, and J. Aarts, Phys. Rev. Lett. **86**, 2427 (2001).

[116] J. W. A. Robinson, Z. H. Barber, and M. G. Blamire, Appl. Phys. Lett. **95**, 192509 (2009).

[117] T. Kontos, M. Aprili, J. Lesueur, F. Gent, B. Stephanidis, and R. Boursier, Phys. Rev. Lett. **89**, 137007 (2002).

[118] Th. Mühge, K. Theis-Bröhl, K. Westerholt, H. Zabel, N. N. Garif'yanov, Yu. V. Goryunov, I. A. Garifullin, and G. G. Khaliullin, Phys. Rev. B **57**, 5071 (1998).

[119] Y. Obi, M. Ikebe, T. Kubo, and H. Fujimori, Physica C **317**, 149 (1999).

[120] H. K. Wong and J. B. Ketterson, J. Low Temp. Phys. **63**, 139 (1986).

[121] F. S. Bergeret, A. F. Volkov, and K. B. Efetov, Phys. Rev. Lett. **86**, 4096 (2001).

[122] A. Kadigrobov, R. I. Shekhter, and M. Jonson, Europhys. Lett. **54**, 394 (2001).

[123] M. Houzet and A. I. Buzdin, Phys. Rev. B **76**, 060504 (2007).

[124] J. D. S. Witt, T. P. A. Hase, R. Fan, C. J. Kinane, T. R. Charlton, S. Langridge, and M. G. Blamire, J. Phys. Condens. Matter, **23**, 416006 (2011).

[125] L. F. Mattheiss, Phys. Rev. B **1**, 373 (1970).

[126] S. Kashiwaya, Y. Tanaka, M. Koyanagi, and K. Kajimura, Phys. Rev. B **53**, 2667 (1996).

[127] I. I. Mazin, Phys. Rev. Lett. **83**, 1427 (1999).

[128] P. Raychaudhuri, A. P. Mackenzie, J. W. Reiner, and M. R. Beasley, Phys. Rev. B **67**, 020411 (2003).

[129] P. Chalsani, S. K. Upadhyay, O. Ozatay, and R. A. Buhrman, Phys. Rev. B **75**, 094417 (2007).

[130] S. Hacohen-Gourgy, B. Almog, and G. Deutscher, Appl. Phys. Lett. 92, 152502 (2008).

[131] F. S. Bergeret, A. F. Volkov, and K. B. Efetov, Appl. Phys. A **89**, 599 (2007)

[132] J. Wang, M. Singh, M. Tian, N. Kumar, B. Liu, C. Shi, J. K. Jain, N. Samarth, T. E. Mallouk, and M. H. W. Chan, Nature Physics **6**, 389 (2010).

[133] F. Hübler, M. J. Wolf, T. Scherer, D. Wang, D. Beckmann, and H. v. Löhneysen, Phys. Rev. Lett. **109**, 087004 (2012).

[134] C. Visani, Z. Sefrioui, J. Tornos, C. Leon, J. Briatico, M. Bibes, A. Barthélémy, J. Santamaría, and Javier E. Villegas, Nature Physics **8**, 539 (2012).

[135] Z. P. Niu, Europhys. Lett. **100** 17012 (2012).

[136] Y.-Q. Ji, Z.-P. Niu, C.-D. Feng, and D.-Y. Xing, Chinese Phys. Lett. **25**, 691 (2008).

[137] C. D. Feng, Z. M. Zheng, R. Shen, B. Wang, and D. Y. Xing, Phys. Rev. B **81**, 224510 (2010).

[138] J. Linder, T. Yokoyama, and A. Sudbø, Phys. Rev. B **79**, 224504 (2009).

[139] S. Kashiwaya, Y. Tanaka, N. Yoshida, and M. R. Beasley, Phys. Rev. B **60**, 3572 (1999).

[140] T. Yamashita, S. Takahashi, H. Imamura, and S. Maekawa, Phys. Rev. B **65**, 172509 (2002).

[141] L. Berger, Phys. Rev. B **54**, 9353 (1996).

[142] E. B. Myers, D. C. Ralph, J. A. Katine, R. N. Louie, and R. A. Buhrman, Science **285**, 867 (1999).

[143] F. Romeo and R. Citro, Phys. Rev. B **84**, 024531 (2011).

[144] M. Bozŏvić and Z. Radović, Phys. Rev. B **66**, 134524 (2002).

[145] J. Linder and A. Sudbø, Phys. Rev. B **75**, 134509 (2007).

[146] R. Grein, T. Löfwander, G. Metalidis, and M. Eschrig, Phys. Rev. B **81**, 094508 (2008).

[147] A. Spuntarelli, P. Pieri, and G. C. Strinati, Physics Reports **488**, 111 (2010).

[148] J.-X. Zhu, C.S. Ting, Phys. Rev. B **61**, 1456 (2000).

[149] R. S. Keizer, S. T. B. Goennenwein, T. M. Klapwijk, G. Miao, G. Xiao, and A. Gupta, Nature **439**, 825 (2006).

[150] G. Baym and L.P. Kadanoff, Phys. Rev. **124**, 287 (1961).

[151] With a current present, one cannot adopt the expedient of choosing real wavefunctions.

[152] P. F. Bagwell, Phys. Rev. B **49**, 6841 (1993).

[153] F. Sols and J. Ferrer, Phys. Rev. B **49**, 15913 (1994).

[154] J. Sanchez-Canizares and F. Sols, Phys. Rev. B **55**, 531 (1997).

[155] M. Eschrig, J. Kopu, J. C. Cuevas, and G. Schrön, Phys. Rev. Lett. **90**, 137003 (2003).

[156] J. Linder, M. Cuocco, and A. Sudbø, Phys. Rev. B **81**, 174526 (2010).

[157] D. C. Ralph and M. D. Stiles, J. Magn, Magn. Mater. **320**, 1190 (2008).

Appendix A

Transfer matrices

The expressions for the matrices we employed in computing the conductance are given below. We assume that the F_1F_2 interface is at $y = a$, where $a < 0$, and F_2S interface is at $y = 0$. It follows that $\mathcal{M}_{F1}$ is:

$$\begin{pmatrix}
e^{ik^+_{\uparrow 1}a} & e^{-ik^+_{\uparrow 1}a} & 0 & 0 & 0 & 0 & 0 & 0 \\
0 & 0 & e^{ik^+_{\downarrow 1}a} & e^{-ik^+_{\downarrow 1}a} & 0 & 0 & 0 & 0 \\
0 & 0 & 0 & 0 & e^{-ik^-_{\uparrow 1}a} & e^{ik^-_{\uparrow 1}a} & 0 & 0 \\
0 & 0 & 0 & 0 & 0 & 0 & e^{-ik^-_{\downarrow 1}a} & e^{ik^-_{\downarrow 1}a} \\
ik^+_{\uparrow 1}e^{ik^+_{\uparrow 1}a} & -ik^+_{\uparrow 1}e^{-ik^+_{\uparrow 1}a} & 0 & 0 & 0 & 0 & 0 & 0 \\
0 & 0 & ik^+_{\downarrow 1}e^{ik^+_{\downarrow 1}a} & -ik^+_{\downarrow 1}e^{-ik^+_{\downarrow 1}a} & 0 & 0 & 0 & 0 \\
0 & 0 & 0 & 0 & -ik^-_{\uparrow 1}e^{-ik^-_{\uparrow 1}a} & ik^-_{\uparrow 1}e^{ik^-_{\uparrow 1}a} & 0 & 0 \\
0 & 0 & 0 & 0 & 0 & 0 & -ik^-_{\downarrow 1}e^{-ik^-_{\downarrow 1}a} & ik^-_{\downarrow 1}e^{ik^-_{\downarrow 1}a}
\end{pmatrix}. \tag{A.1}$$

For the $\mathcal{M}_{F2}$, we have

$$\begin{pmatrix}
\widetilde{f^+_\uparrow} & \widetilde{f^+_\uparrow}^* & \widetilde{g^+_\uparrow} & \widetilde{g^+_\uparrow}^* & 0 & 0 & 0 & 0 \\
\widetilde{f^+_\downarrow} & \widetilde{f^+_\downarrow}^* & \widetilde{g^+_\downarrow} & \widetilde{g^+_\downarrow}^* & 0 & 0 & 0 & 0 \\
0 & 0 & 0 & 0 & \widetilde{f^-_\uparrow} & \widetilde{f^-_\uparrow}^* & \widetilde{g^-_\uparrow} & \widetilde{g^-_\uparrow}^* \\
0 & 0 & 0 & 0 & \widetilde{f^-_\downarrow} & \widetilde{f^-_\downarrow}^* & \widetilde{g^-_\downarrow} & \widetilde{g^-_\downarrow}^* \\
ik^+_{\uparrow 2}\widetilde{f^+_\uparrow} & -ik^+_{\uparrow 2}\widetilde{f^+_\uparrow}^* & ik^+_{\downarrow 2}\widetilde{g^+_\uparrow} & -ik^+_{\downarrow 2}\widetilde{g^+_\uparrow}^* & 0 & 0 & 0 & 0 \\
ik^+_{\uparrow 2}\widetilde{f^+_\downarrow} & -ik^+_{\uparrow 2}\widetilde{f^+_\downarrow}^* & ik^+_{\downarrow 2}\widetilde{g^+_\downarrow} & -ik^+_{\downarrow 2}\widetilde{g^+_\downarrow}^* & 0 & 0 & 0 & 0 \\
0 & 0 & 0 & 0 & ik^-_{\uparrow 2}\widetilde{f^-_\uparrow} & -ik^-_{\uparrow 2}\widetilde{f^-_\uparrow}^* & ik^-_{\downarrow 2}\widetilde{g^-_\uparrow} & -ik^-_{\downarrow 2}\widetilde{g^-_\uparrow}^* \\
0 & 0 & 0 & 0 & ik^-_{\uparrow 2}\widetilde{f^-_\downarrow} & -ik^-_{\uparrow 2}\widetilde{f^-_\downarrow}^* & ik^-_{\downarrow 2}\widetilde{g^-_\downarrow} & -ik^-_{\downarrow 2}\widetilde{g^-_\downarrow}^*
\end{pmatrix}, \tag{A.2}$$

where $\widetilde{f_\sigma^+} = f_\sigma^+ e^{ik_{\uparrow 2}^+ a}$, $\widetilde{f_\sigma^-} = f_\sigma^- e^{ik_{\uparrow 2}^- a}$, $\widetilde{g_\sigma^+} = g_\sigma^+ e^{ik_{\downarrow 2}^+ a}$, and $\widetilde{g_\sigma^-} = g_\sigma^- e^{ik_{\downarrow 2}^- a}$. The expression for $\tilde{\mathcal{M}}_{F2}$ is

$$\begin{pmatrix} f_\uparrow^+ & f_\uparrow^+ & g_\uparrow^+ & g_\uparrow^+ & 0 & 0 & 0 & 0 \\ f_\downarrow^+ & f_\downarrow^+ & g_\downarrow^+ & g_\downarrow^+ & 0 & 0 & 0 & 0 \\ 0 & 0 & 0 & 0 & f_\uparrow^- & f_\uparrow^- & g_\uparrow^- & g_\uparrow^- \\ 0 & 0 & 0 & 0 & f_\downarrow^- & f_\downarrow^- & g_\downarrow^- & g_\downarrow^- \\ ik_{\uparrow 2}^+ f_\uparrow^+ & -ik_{\uparrow 2}^+ f_\uparrow^+ & ik_{\downarrow 2}^+ g_\uparrow^+ & -ik_{\downarrow 2}^+ g_\uparrow^+ & 0 & 0 & 0 & 0 \\ ik_{\uparrow 2}^+ f_\downarrow^+ & -ik_{\uparrow 2}^+ f_\downarrow^+ & ik_{\downarrow 2}^+ g_\downarrow^+ & -ik_{\downarrow 2}^+ g_\downarrow^+ & 0 & 0 & 0 & 0 \\ 0 & 0 & 0 & 0 & ik_{\uparrow 2}^- f_\uparrow^- & -ik_{\uparrow 2}^- f_\uparrow^- & ik_{\downarrow 2}^- g_\uparrow^- & -ik_{\downarrow 2}^- g_\uparrow^- \\ 0 & 0 & 0 & 0 & ik_{\uparrow 2}^- f_\downarrow^- & -ik_{\uparrow 2}^- f_\downarrow^- & ik_{\downarrow 2}^- g_\downarrow^- & -ik_{\downarrow 2}^- g_\downarrow^- \end{pmatrix}, \tag{A.3}$$

and for $\mathcal{M}_S$,

$$\begin{pmatrix} u_0 & u_0 & 0 & 0 & 0 & 0 & v_0 & v_0 \\ 0 & 0 & u_0 & u_0 & v_0 & v_0 & 0 & 0 \\ 0 & 0 & v_0 & v_0 & u_0 & u_0 & 0 & 0 \\ v_0 & v_0 & 0 & 0 & 0 & 0 & u_0 & u_0 \\ ik^+ u_0 & -ik^+ u_0 & 0 & 0 & 0 & 0 & -ik^- v_0 & ik^- v_0 \\ 0 & 0 & ik^+ u_0 & -ik^+ u_0 & -ik^- v_0 & ik^- v_0 & 0 & 0 \\ 0 & 0 & ik^+ v_0 & -ik^+ v_0 & -ik^- u_0 & ik^- u_0 & 0 & 0 \\ ik^+ v_0 & -ik^+ v_0 & 0 & 0 & 0 & 0 & -ik^- u_0 & ik^- u_0 \end{pmatrix}. \tag{A.4}$$

The last matrix $\mathcal{M}_S$ can be generalized to the transfer matrix of intermediate layers, with an appropriate strength of the superconducting pair potential, in the S region.